Electronic and topological properties of low-dimensional α-Sn and HgTe structures

Dissertation

zur Erlangung des akademischen Grades

doctor rerum naturalium (Dr. rer. nat.)

vorgelegt dem Rat der Physikalisch-Astronomischen Fakultät
der Friedrich-Schiller-Universität Jena

von Dipl.-Phys. Sebastian Küfner

geboren am 13. Mai 1987 in Gera

Gutachter:

1. Prof. Dr. Friedhelm Bechstedt (Friedrich-Schiller Universität Jena)
2. Prof. Dr. Miguel Marques (Martin-Luther-Universität Halle-Wittenberg)
3. Prof. Dr. Thomas G. Pedersen (Aalborg University)

Tag der Disputation: 23.06.2015

There is a theory which states that if ever anyone discovers exactly what the Universe is for and why it is here, it will instantly disappear and be replaced by something even more bizarre and inexplicable. There is another theory which states that this has already happened.

(Douglas Adams)

Contents

1 Introduction and Motivation

The group-IV material α-Sn and the II-VI compound semiconductor HgTe exhibit remarkable physical properties. The two materials possess different space groups O_h^7 (diamond structure) and T_d^2 (zinc blende structure). However, in contrast to other tetrahedrally coordinated semiconductors, they are characterized by a vanishing fundamental band gap, where the four-fold degenerated Γ_{8v} states pin the Fermi level [1]. In addition, as a consequence of the relativistic mass-Darwin effect, the s-like Γ_{6c} levels are energetically lower than the p-like Γ_{8v} levels and, hence, form an inverted band structure with a "negative gap" with respect to other group-IV semiconductors like germanium or compound semiconductors such as CdTe [1, 2]. Due to the large spin-orbit coupling (SOC) in both materials, a theoretical description of their quasiparticle electronic properties is difficult. An astonishing property of both materials is, that they have been found to be three-dimensional (3D) topological insulators (TIs), if a slight strain opens a small gap between the Γ_{8v} states [3]. The topological character is mainly a consequence of the SOC-induced band inversion. TIs are characterized by an insulating bulk material but exhibit metallic surface or edge states, that form Dirac cones inside the fundamental gap of the bulk material [4–6]. These states possess linear $\mathbf{k}$-dispersion. Spin polarization leads to intrinsic spin currents in the absence of an external magnetic field. This property characterizes a new state of matter, which is called the quantum-spin Hall (QSH) phase [4, 5, 7, 8] and might offer applications in spintronics [9–11].

The physical properties of a crystalline material are significantly influenced, when the dimensionality is reduced by the formation of nanocrystals (NCs), surfaces, interfaces, etc. [12, 13] due to spacial confinement and surface or interface effects. For example, the optical absorption and emission properties may be controlled by the size of the nanostructures [14–16]. Indeed, infrared emission from colloidal HgTe nanocrystals (NCs) [17] and photoresponse of HgTe quantum dot films between 3 and 5 μm [18] have been recently demonstrated. Due to the similar electronic properties, the same effects can be expected in the case of α-Sn NCs. However, the preparation of tetrahedrally coordinated α-Sn NCs is challenging, because α-Sn is only stable for temperatures below 13.2 °C. For higher temperatures, a phase transition into metallic β-Sn occurs [1]. Nevertheless, crystalline matrices such as Si and Ge with diamond structure prevent the collapse to the denser β form and particles of α-Sn

can be stabilized [19–22], at least with diameters below 8 nm [20]. Apart from a tight-binding study of the optical absorption [14], *ab-initio* calculations of the optical properties of α-Sn NCs are completely missing. The size-dependent optical absorption and emission properties, the influence of the nanostructuring on energy level symmetry and the energetic level ordering have not been studied so far.

Recently, a 3D topological phase in strained α-Sn (001) films has been reported [23, 24]. This is in accordance with the expectation to find topological surface states at surfaces of strained α-Sn due to its topological non-trivial character. These films are pseudomorphically grown on InSb(001) substrates, so that they are biaxially strained due to the small lattice mismatch between both materials. Thick and ultrathin layers with varying thicknesses 0.1 to 1 μm [23] and 2.0 to 5.5 nm [24], respectively, have been investigated. Angle-resolved photoemission spectroscopy (ARPES) including spin detection has been used to probe topological surface states (TSSs) for ultrathin and thick α-Sn films. The measurements have been verified by electronic structure calculations in the framework of the density functional theory (DFT) including SOC [23, 24]. However, the energetic position of the Dirac point is below the Fermi level, which contradicts the classic picture of gapless edge states bridging the fundamental bulk band gap [4, 5, 7, 8]. In addition, it seems to depend on film thickness and substrate doping, and, therefore, this topic is under debate.

In 2006, Bernevig et al. [5] predicted HgTe quantum wells (QWs) to be two-dimensional (2D) TIs. The QWs consist of a thin HgTe layer with thickness d_1 sandwiched between barrier layers of CdTe. The lattice mismatch between the both materials leads to a symmetry-lowering by biaxial strain, that causes splitting of the HgTe Γ_{8v} states and, consequently, a gap opening in HgTe. As pointed out, strained HgTe is a strong topological insulator [3]. A HgTe/CdTe QW structure exhibits consequently interfaces between a strong TI and the wide-gap conventional semiconductor CdTe. A single interface between two half spaces filled with HgTe and CdTe, respectively, is expected to possess helical states located the interface, which are referred to as edge states. In a QW structure with finite thicknesses of the respective layers, however, the barrier material CdTe leads to a confinement of electrons or holes in the HgTe layers in-between. Its consequence for extremely thin layers is a level inversion in the HgTe layer, such that the band ordering of the QW structure becomes that of a trivial insulator. For large thicknesses, the HgTe films should behave similarly to the bulk material with an inverted band structure. The situation becomes similar to that of an interface between two half-spaces such that the QWs possess a QSH phase character [10, 25]. This picture of a thickness-dependent 2D TI has been confirmed experimentally [7, 26]. The critical thickness d_c of the HgTe

layer, where the topological phase transition between the trivial insulating phase and the QSH phase occurs, was found to be 6.3 nm[7, 26]. *Ab-initio* studies on this topic are widely missing. Influences of the barrier material, interface electronics and geometry remain unknown. The similarity of the bulk electronic band structures suggests, that the same properties as for HgTe QWs can be expected for α-Sn/CdTe QW structures. However, there are no respective theoretical or experimental studies available, which rises several questions. In particular, the question whether or not α-Sn QWs embedded in a wide-gap semiconductor show a similar quantum phase transition versus thickness as the HgTe material. The higher space-group symmetry, the different interface properties, and the slightly changed spin-orbit interaction may modify the topological behavior. The spin-orbit interaction, in particular that in the p-derived valence states, is different due to the contribution of both atoms in the unit cell (α-Sn) and mainly the anion (HgTe) to the states at the top of the valence bands, and the different local electrostatic properties due to the different bonding character in the QW layers and their interfaces with the CdTe barrier material.

In this thesis, electronic and topological properties of α-Sn and HgTe bulk and low-dimensional systems such as NCs, surfaces and superlattice structures are studied by means of first-principles calculations in the framework of DFT. In Chapter 2, the theoretical background, the numerical implementation and the studied crystal structures are introduced. To overcome the computational limitations regarding the system size within the DFT, a tight-binding scheme including nearest-neighbor SOC is developed. In Chapter 3, results are presented. In a first step, in Sec. 3.1, the electronic properties of the bulk zero-gap semiconductors α-Sn and HgTe, and the conventional semiconductors CdTe and InSb are discussed. Several exchange-correlation functionals are compared and evaluated concerning accuracy and computational effort in order to find the most suitable method for the description of the low-dimensional systems. It is concluded, that the Tran-Blaha method [27] yields remarkably reasonable band-structure results, while the computational cost is comparably low. Unfortunately, the application of the Tran-Blaha method is restricted to homogeneous systems, which do not include vacuum. Therefore, it is applied in the case of quantum-well structures whereas Kohn-Sham or generalized Kohn-Sham electronic structures are studied for the other nanostructures. Small nanocrystals and surface slabs are treated within hybrid functionals [28]. For larger systems, the local density approximation [29] and the tight-binding method is applied to study system sizes, which are beyond the possibilities of DFT. In Sec. 3.2, the discussion of the bulk properties is extended to the topology of the bulk band structures of α-Sn, HgTe, CdTe, and InSb. Calculating the topological invariants, which dis-

tinguish topologically trivial and topologically non-trivial systems, it is shown, that α-Sn and HgTe are 3D topological insulators, while CdTe and InSb are topologically trivial semiconductors. These findings motivate the investigation of low-dimensional structures consisting of these materials in the sections thereafter. The discussion of the low-dimensional structures starts with the structural, electronic and optical properties of α-Sn NCs including SOC. The size dependence of the fundamental gap, its inversion for larger diameters, and the related optical absorption and emission spectra are discussed in particular.

In the subsequent Section 3.4, surfaces of biaxially strained α-Sn are investigated. The existence of topological surface states for thin and thick α-Sn films is discussed in detail. Their linear dispersion, helical character, localization, and spin polarization are studied. Special attention is given to the dependence of the absolute energetic position of the Dirac cone and its relation to bulk-derived states on the film thickness.

The last part of the results chapter, Sec. 3.5, deals with the electronic structure of α-Sn/CdTe and HgTe/CdTe quantum wells. The similarities and differences of the two embedded zero-gap semiconductors on the formation of quantum-well, edge and interface states are investigated in detail. The discussion is split in three subsections. The discussion starts with the investigation of the interface electrostatics of these QW structures for (001) and (110) orientation of the interface normal in Sec. 3.5.1. The band discontinuities at the interfaces depending on the well material, α-Sn or HgTe, and the well material and barrier material thicknesses are studied. The resulting types of the heterostructures are identified and possible effects on the electronic structure of the respective interfaces are discussed. In the second part 3.5.2, the electronic structure depending on the QW thickness of QWs grown in [001] orientation is described. It is shown, that for both well materials a phase transition occurs from a topological trivial insulating phase into a QSH phase. The characteristic thicknesses of α-Sn and HgTe, respectively, where this transition occurs, are calculated and the QSH phase is characterized in detail concerning the occurrence of spin-polarized edge states with linear band dispersion. In a following step, in Sec. 3.5.3, α-Sn and HgTe QWs with [110] orientation are studied. It is shown, that HgTe QWs behave similarly to the [001] case and a phase transition into the QSH phase occurs, while in α-Sn QWs this transition is inhibited by a break of inversion symmetry caused by electrostatics.

Finally, in Sec. 4 a summary and conclusions are given.

Most of the results discussed and depicted in this thesis have been published in Refs. [30–34].

2 Theoretical Background

2.1 The many-body problem

All matter is made up of atoms consisting of protons and neutrons in the atomic core and electrons in the atomic shell. The description of real-structure condensed matter systems therefore requires the solution of a many-problem of interacting electrons and nuclei within the framework of quantum mechanics, because the classical mechanics do not apply at an atomic length scale. The dimensionality of this problem far beyond from what can be solved analytically. Even a numerical treatment of so many particles asks for reasonable approximations. In the present chapter, the many-body problem is described in three steps. In a first step, the general theory is presented. In a second step, necessary simplifications are introduced leading to the formalism of the density functional theory. Some improvements for electronic excitations are also discussed. Finally, in a third step, concepts of the numerical implementation including details concerning the actual calculations are put forward.

2.1.1 The many-body Hamiltonian and its simplification

We use the many-body Hamilton operator to describe the interaction between electrons and nuclei

$$\begin{aligned} H(\{\mathbf{x}_i\},\{\mathbf{R}_j\}) &= T_n(\{\mathbf{q}_i\}) + T_e(\{\mathbf{p}_i\}) + V_{nn}(\{\mathbf{R}_j\}) + V_{ee}(\{\mathbf{X}_i\}) + V_{ne}(\{\mathbf{R}_j,\mathbf{X}_i\}) \\ &= -\sum_j \tfrac{\hbar^2}{2M_j}\Delta_{\mathbf{r}_j} - \sum_i \tfrac{\hbar^2}{2m_i}\Delta_{\mathbf{x}_i} + \tfrac{1}{2}\sum_{j\neq l} Z_j Z_l v(\mathbf{r}_j,\mathbf{r}_l) \\ &\quad + \tfrac{1}{2}\sum_{i\neq k} v(\mathbf{x}_i,\mathbf{x}_k) - \tfrac{1}{2}\sum_{i,j} Z_j v(\mathbf{x}_i,\mathbf{r}_j). \end{aligned} \tag{2.1}$$

Here, $v(\mathbf{x},\mathbf{x}') = \frac{e^2}{4\pi\epsilon_0}\frac{1}{|\mathbf{x}-\mathbf{x}'|}$ denotes the bare Coulomb potential. The coordinates $\mathbf{X}_i = \{\mathbf{p}_i,\mathbf{x}_i,\mathbf{s}_i\}$ consist of the momenta $\{\mathbf{p}_i\}$, the spatial coordinates $\{\mathbf{x}_i\}$, and the spins $\{\mathbf{s}_i\}$ of the electrons (labeled by the index e). Analogously, the nuclei (labeled by the index n) coordinates $\mathbf{R_j}$ are given by their momenta $\{\mathbf{q}_j\}$, position vectors $\{\mathbf{r_j}\}$ and spins $\{\mu_j\}$. The operators T_e and T_n denote the kinetic-energy operators of electrons and cores, respectively. Z_j denotes the nuclear charge, m_e and M_j are the electron mass and the nuclear mass. Finally, e is the elemental charge. The

Hamiltonian (2.1) does not regard for transversal electron-electron interaction and relativistic corrections, such as spin-orbit coupling (SOC), and spin-spin interaction. Such effects will be included later on (see Sec. 2.2.4).

However, regarding macroscopic systems, the order of magnitude of interacting particles is defined by the Avogadro constant 6.022×10^{23} particles per mol. It is obvious, that a many-body problem defined by the stationary Schrödinger's equation for the many-body wave function $|\psi(\{\mathbf{X}_i\},\{\mathbf{R}_j\})\rangle$:

$$H(\{\mathbf{X}_i\},\{\mathbf{R}_j\})|\psi(\{\mathbf{X}_i\},\{\mathbf{R}_j\})\rangle = E|\psi(\{\mathbf{X}_i\},\{\mathbf{R}_j\})\rangle \tag{2.2}$$

arising from the Hamiltonian (2.1) cannot be solved explicitly and, consequently, simplifications have to be made. The first step to simplify of the problem is the separation of the electronic and nuclear motion within the Born-Oppenheimer approximation [35]. The mass of a proton is by a factor 1836 larger than the electron mass. Therefore, the characteristic velocities of the electrons are much faster than that of the nuclei. It can be assumed, that the electrons follow a displacement of the nuclei almost instantaneously. In this case, the behavior of the electronic system can be described by a Schrödinger equation for the electrons in an external potential formed by the nuclei at certain fixed positions $\mathbf{r}_j$.

If the action of the fixed nuclei is replaced by a generalized external scalar electromagnetic potential $v_{ext}(\{\mathbf{x}_i,\mathbf{s}_i\})$ the Hamiltonian describing the electronic system takes the form

$$H(\{\mathbf{X}_i\}) = T_e(\{\mathbf{p}_i\}) + V_{ee}(\{\mathbf{x}_i\}) + V_{ext}(\{\mathbf{x}_i,\mathbf{s}_i\}). \tag{2.3}$$

The operator of the action of an external potential $V_{ext}(\{\mathbf{x}_i,\mathbf{s}_i\})$ on the electrons regards for the potential energy of the electronic system within the electrostatic field $U_{ext}(\mathbf{x})$ arising from the nuclear charges as well as an additional coupling of the electronic spins with an external magnetic field $\mathbf{B}^{\text{ext}}(\mathbf{x})$. Note, that in equ. (2.3) the arrangement of the nuclei enters only parametrically.

2.1.2 Second Quantization

The Hamiltonian (2.3) describes a system consisting only of electrons. Electrons are fermions and indistinguishable particles. The N-electron wave function $|\psi\rangle_N$ must therefore be antisymmetric under the commutation of two electrons according to the Pauli principle [36]. Following the framework of the second quantization [36, 37], the creation and annihilation operators $\phi^\dagger_{\alpha_i}(\mathbf{x}_i)$ and $\phi_{\alpha_i}(\mathbf{x}_i)$, respectively, of an electron at the position $\mathbf{x}_i$ and the spin state α_i are introduced. These operators

are defined on the Fock space, that is given by the direct product of the Hilbert spaces of fixed electron numbers $M = 1...N$. The creation operator $\phi^\dagger_{\alpha_i}(\mathbf{x}_i)$ creates an electron at the place $\mathbf{x}_i$ with the spin state $\alpha_i \in \{\uparrow;\downarrow\}$, whereas the annihilation operator $\phi_{\alpha_i}(\mathbf{x}_i)$ annihilates the same electron. The N-electron wave function, which is a solution of the Schrödinger equation (2.2), is constructed from the vacuum state $|0\rangle$ by successively applying the creation operators

$$|\psi\rangle_N = |\mathbf{x}_1, \alpha_1; ...; \mathbf{x}_n, \alpha_n\rangle = \phi^\dagger_{\alpha_1}(\mathbf{x}_1)...\phi^\dagger_{\alpha_N}(\mathbf{x}_N)|0\rangle. \tag{2.4}$$

The antisymmetry of the N-electron wave function under the commutation of two electrons is ensured by the anti-commutator relations

$$[\phi^\dagger_\alpha(\mathbf{x}_i), \phi^\dagger_\beta(\mathbf{x}_j)]_+ = [\phi_\alpha(\mathbf{x}_i), \phi_\beta(\mathbf{x}_j)]_+ = 0 \tag{2.5}$$

and

$$[\phi_\alpha(\mathbf{x}_i), \phi^\dagger_\beta(\mathbf{x}_j)]_+ = \delta(\mathbf{x}_i - \mathbf{x}_j)\delta_{\alpha\beta}. \tag{2.6}$$

The many particle states (2.4) form an antisymmetric basis system on the Fock space, which can be used to expand any operator on that Fock space. For a specific choice of the coordinate system, the wave functions are represented by Pauli spinors, $\phi^i(\mathbf{x}) = (\phi^i_\uparrow(\mathbf{x}), \phi^i_\downarrow(\mathbf{x}))$. The spin index α denotes the spin up ($\uparrow$) and spin down ($\downarrow$) component. Thereby, the spin vector $\mathbf{s}_i$ of the i-th electron is given by $\mathbf{s}_i = \sum_{\alpha,\beta} \phi^i_\alpha \sigma_{\alpha\beta} \phi^i_\beta$, where σ denotes the vector of the pauli matrices. Multiplied with the Bohr Magneton μ_B, $\mathbf{s}_i$ gives the vetor of the spin magnetization.

Within second quantization, the operators contributing to the Hamiltonian (2.3) are given as

$$T_e = -\frac{\hbar^2}{2m_e} \sum_\alpha \int \mathrm{d}^3\mathbf{x} \phi^\dagger_\alpha(\mathbf{x}) \Delta \phi_\alpha(\mathbf{x}) \tag{2.7}$$

$$V_{ee} = \frac{1}{2} \sum_{\alpha,\beta} \int\int \mathrm{d}^3\mathbf{x}_1 \mathrm{d}^3\mathbf{x}_2 \phi^\dagger_\alpha(\mathbf{x}_1) \phi^\dagger_\beta(\mathbf{x}_2) v(\mathbf{x}_1, \mathbf{x}_2) \phi_\beta(\mathbf{x}_2) \phi_\alpha(\mathbf{x}_1) \tag{2.8}$$

$$V_{ext} = \sum_{\alpha,\beta} \int \mathrm{d}^3\mathbf{x} \phi^\dagger_\alpha(\mathbf{x}) w_{\alpha\beta}(\mathbf{x}) \phi_\beta(\mathbf{x}) = \int \mathrm{d}^3\mathbf{x} \hat{n}_{\alpha\beta}(\mathbf{x}) w_{\alpha\beta}(\mathbf{x}) \tag{2.9}$$

Here, $\hat{n}_{\alpha\beta}(\mathbf{x}) = \phi^\dagger_\alpha(\mathbf{x})\phi_\beta(\mathbf{x})$ is the operator of the spin density. The sum over its diagonal elements yields the operator of the electron density $\hat{n}(\mathbf{x}) = \sum_{\alpha\beta} \delta_{\alpha\beta} \hat{n}_{\alpha\beta}(\mathbf{x})$. The external potential $w_{\alpha\beta}(\mathbf{x}) = U_{ext}(\mathbf{x})\delta_{\alpha\beta} + (\mu_B \sigma \mathbf{B}^{\mathrm{ext}}(\mathbf{x}))$ regards for the external

electrostatic field of the nuclei $U_{ext}(\mathbf{x})$ and an external magnetic filed $\mathbf{B}^{\text{ext}}(\mathbf{x})$.

2.2 Density Functional Theory

Despite the separation of the nuclear and electronic motion, the many-body problem remains too large to be solved explicitly due to the $3N$ spatial times 2 spin degrees of freedom per electron of the N-electron system. Hohenberg and Kohn [38] proved that it is possible to derive the physical properties of the many-electron system as a function of the ground-state electron density. The Hohenberg-Kohn theorems (HKT) are originally formulated for electrons inside an external electrostatic potential, as e.g. induced by the positively charged nuclei, assuming a non-degenerate ground-state $|g\rangle$. This section follows the extended formulation of the theorems to spin-dependent external potentials $w_{\alpha\beta}(\mathbf{x})$ by von Barth and Hedin [39]. The degrees of freedom are thereby reduced to only three spatial coordinates and a 2×2 spin density matrix $n_{\alpha\beta}(\mathbf{x}) = \langle g|\hat{n}_{\alpha\beta}(\mathbf{x})|g\rangle$ instead of the $6N$ degrees of freedom of the N-electron system.

2.2.1 Hohenberg-Kohn Theory

Because of the non-degeneracy of the ground-state, the external potential $U_{ext}(\mathbf{x})$ and the external magnetic field $\mathbf{B}^{\text{ext}}(\mathbf{x})$ uniquely determine the spin-density matrix $n_{\alpha\beta}(\mathbf{x})$ and the many-body wave function $|g\rangle$ in the ground-state. The first HKT proves, that the opposite direction is also true.

1. **Hohenberg-Kohn Theorem 1**
   For a non-degenerate ground-state $|g\rangle$, the ground-state energy E_g of an inhomogeneous electron gas is a functional of the ground-state spin-density matrix, $E_g = E_g[n_{\alpha\beta}(\mathbf{x})]$ and it holds

$$\begin{aligned} E_g[n_{\alpha\beta}(\mathbf{x})] &= \underbrace{\langle g[n_{\alpha\beta}(\mathbf{x})]|T_e + V_{ee}|g[n_{\alpha\beta}(\mathbf{x})]\rangle}_{F[n_{\alpha\beta}(\mathbf{x})]} \\ &\quad + \sum_{\alpha\beta} \int \mathrm{d}^3\mathbf{x} w_{\alpha\beta}(\mathbf{x}) n_{\alpha\beta}(\mathbf{x}). \end{aligned} \tag{2.10}$$

   The functional $F[n_{\alpha\beta}(\mathbf{x})]$ is independent of the external fields $U_{ext}(\mathbf{x})$ and $\mathbf{B}^{\text{ext}}(\mathbf{x})$. The variational character of the total-energy functional (2.10) is specified within the second HKT.

2. **Hohenberg-Kohn Theorem 2**
   For non-degenerate ground-state $|g\rangle$, the functional of the total energy $E[n_{\alpha\beta}(\mathbf{x})]$

is minimal with respect to a variation of the spin-density matrix at the ground-state density.

In summary: for each external potential (including a magnetic field term), a uniquely defined spin-density matrix exists and the total energy, which is a functional of this spin-density matrix, becomes minimal for the ground-state spin-density matrix. The huge advantage emerging from these two theorems is, that it is in principle possible to derive the ground-state properties of the many-body system from a minimization of the total energy under a variation with respect to the spin-density matrix, and, consequently, a massive reduction of the problem's dimensionality.

2.2.2 Kohn-Sham Theory

Although the HKT allow for a reduction of the total-energy minimization to a dependence on the 2×2 spin-density matrix $n_{\alpha\beta}(\mathbf{x})$, the functional $F[n_{\alpha\beta}(\mathbf{x})]$ remains unknown. In 1965, Kohn and Sham [40] suggested to replace the system of interacting electrons with collinear spins in an external potential $V_{ext}(\mathbf{x})$ by a system of non-interacting electrons in an effective potential $V^{eff}(\mathbf{x})$ with the same ground-state electron density $n^{eff}(\mathbf{x})$ as the interacting system: $n^{eff}(\mathbf{x}) = n(\mathbf{x}) = n_{\alpha\alpha}(\mathbf{x}) + n_{\beta\beta}(\mathbf{x})$. This formalism was extended by von Barth and Hedin to spin-dependent external potentials $w_{\alpha\beta}(\mathbf{x})$ and the corresponding effective potential $w^{eff}_{\alpha\beta}(\mathbf{x})$. The ground-state electron densities $n(\mathbf{x})$ and $n^{eff}(\mathbf{x})$ are replaced by the ground-state spin-density matrix $n_{\alpha\beta}(\mathbf{x}) = n^{eff}_{\alpha\beta}(\mathbf{x})$.

The energy of the non-interacting system $E_{KS}[n_{\alpha\beta}]$ is a functional of the spin-density matrix

$$E_{KS}[n_{\alpha\beta}] = T_S[n_{\alpha\beta}] + \sum_{\alpha,\beta} \int \mathrm{d}^3\mathbf{x} n_{\alpha\beta}(\mathbf{x}) w^{eff}_{\alpha\beta}(\mathbf{x}). \tag{2.11}$$

Here, $T_S[n_{\alpha\beta}]$ denotes the kinetic energy of the non-interacting electrons. To obtain an expression for the yet unknown effective potential $w^{eff}_{\alpha\beta}(\mathbf{x})$ of the non-interacting system, the energy functional (2.10) of the full interacting system is rewritten:

$$E[n_{\alpha\beta}] = T_S[n_{\alpha\beta}] + E_H[n_{\alpha\beta}] + E_{XC}[n_{\alpha\beta}] + \sum_{\alpha,\beta} \int \mathrm{d}^3\mathbf{x} n_{\alpha\beta}(\mathbf{x}) w_{\alpha\beta}(\mathbf{x}). \tag{2.12}$$

Here, the Hartree energy

$$\begin{aligned} E_H[n_{\alpha\beta}] &= \tfrac{1}{2}\sum_{\alpha,\beta}\int \mathrm{d}^3\mathbf{x}\int \mathrm{d}^3\mathbf{x}' n_{\alpha\alpha}(\mathbf{x})v(\mathbf{x},\mathbf{x}')n_{\beta\beta}(\mathbf{x}') \\ &\doteq \tfrac{1}{2}\sum_{\alpha}\int \mathrm{d}^3\mathbf{x} n_{\alpha\alpha}(\mathbf{x})v_H[n_{\alpha\alpha}](\mathbf{x}) \end{aligned} \tag{2.13}$$

and the exchange-correlation (XC) energy

$$E_{XC}[n_{\alpha\beta}] = T[n_{\alpha\beta}] - T_S[n_{\alpha\beta}] + V_{ee}[n_{\alpha\beta}] - E_H[n_{\alpha\beta}] \tag{2.14}$$

have been introduced. In equ. (2.13), the Hartree-potential

$$v_H[n_{\alpha\alpha}](\mathbf{x}) = \sum_{\gamma}\int \mathrm{d}^3\mathbf{x}' n_{\gamma\gamma}(\mathbf{x}')v(\mathbf{x},\mathbf{x}') \tag{2.15}$$

is defined. The exchange-correlation energy corrects the of the kinetic energy of the full interacting system and that of the non-interacting particles as well as the unphysical self-interaction of electrons contained in the Hartree energy (2.13).

As introduced above, the Kohn-Sham system of independent particles is required to possess the same ground-state spin-density matrix $n_{\alpha\beta}(\mathbf{x})$ as the fully interacting system. According to the Hohenberg-Kohn theorems, both functionals become minimal at the ground-state spin-density matrix under a variation with respect to $n_{\alpha\beta}(\mathbf{x})$ and the additional condition of particle number conservation. This allows to determine the effective Kohn-Sham potential except for an unimportant additive constant, which is neglected:

$$w^{eff}_{\alpha\beta}(\mathbf{x}) = w_{\alpha\beta}(\mathbf{x}) + v_H[n_{\alpha\beta}](\mathbf{x}) + v^{XC}_{\alpha\beta}[n_{\alpha\beta}](\mathbf{x}) \tag{2.16}$$

with the XC potential

$$v^{XC}_{\alpha\beta}[n_{\alpha\beta}](\mathbf{x}) = \frac{\delta}{\delta n_{\alpha\beta}(\mathbf{x})}E_{XC}[n_{\alpha\beta}]. \tag{2.17}$$

The eigenvalue problem arising from the Hamiltonian, that is associated with the effective Kohn-Sham potential in (2.16), leads to a set of single-particle Schrödinger equations, the Kohn-Sham equations

$$\sum_{\beta}\{-\delta_{\alpha\beta}\frac{\hbar^2}{2m_e}\Delta + \omega_{\alpha\beta}(\mathbf{x}) + \delta_{\alpha\beta}v_H[n_{\alpha\alpha}](\mathbf{x}) + v^{XC}_{\alpha\beta}[n_{\alpha\beta}](\mathbf{x})\}\phi^i_\beta(\mathbf{x}) = \varepsilon^i\phi^i_\alpha(\mathbf{x}). \tag{2.18}$$

The eigenfunctions are represented by Pauli spinors, $\phi^i(\mathbf{x}) = (\phi^i_\uparrow(\mathbf{x}), \phi^i_\downarrow(\mathbf{x}))$, the corresponding single-particle Kohn-Sham eigenenergies are denoted as ε^i. The total energy follows from (2.12):

$$E[n_{\alpha\beta}] = \sum_{i=1}^{N} \varepsilon^i - E_H[n_{\alpha\beta}] + E_{XC}[n_{\alpha\beta}] - \sum_{\alpha,\beta} \int \mathrm{d}^3\mathbf{x} n_{\alpha\beta}(\mathbf{x}) v_{\alpha\beta}^{XC}[n_{\alpha\beta}](\mathbf{x}), \quad (2.19)$$

where first term is the band structure energy.

2.2.3 Modeling of exchange and correlation

The Kohn-Sham theory allows the calculation of the exact ground-state energy and the corresponding spin-density matrix from the solution of a system of one-particle Schrödinger equations. However, an exact determination of the exchange-correlation functional in equ. (2.17) is not possible and, therefore, approximations are required. In this section, the approximations, which are used in the present work, are discussed.

2.2.3.1 Hartree-Fock approximation

Fock [41] proposed to construct the N-electron wave function $|\psi\rangle_N$ introduced in (2.4) as a Slater determinant [42] of single particle orbitals $\phi_\alpha^i(\mathbf{x})$, which fulfills the Pauli principle by definition. In the resulting total-energy functional, which is given by the expectation value of the Hamiltonian (2.3) within the many body wave function, the exchange and correlation energy (2.14) is replaced by the non-local exchange interaction in Hartree-Fock (HF) approximation

$$E_X[\psi] = -\frac{1}{2} \sum_{\alpha,\beta} \int \mathrm{d}^3\mathbf{x} \int \mathrm{d}^3\mathbf{x}' v(\mathbf{x},\mathbf{x}') |n_{\alpha\beta}(\mathbf{x},\mathbf{x}')|^2 \quad (2.20)$$

that corrects the Hartree energy (2.13) by the unphysical self-interaction of the electrons. The correlation energy is neglected.

2.2.3.2 Local spin density approximation (LSDA) and generalized gradient approximation (GGA)

The local spin density approximation (LSDA) [29], which is a generalization of the local density approximation (LDA) [40] for spin polarized systems, is one of the most simple approximations of the XC potential. It is assumed, that the spin densities are slowly varying, which means, that they do not considerably vary within a length scale defined by the average distance of the electrons in the system. For fixed position $\mathbf{x}$, a local spin-magnetization axis can be defined, such that the 2×2 spin-density matrix $n_{\alpha\beta}(\mathbf{x})$ becomes digonal. Therefore, the local spin-magnetization inside the PAW

sphere (see Sec. 2.3.3) can be described by two spin-densities $n_\sigma(\mathbf{x})$, the spin-up, and the spin-down density. They are the local eigenvalues of $n_{\alpha\beta}(\mathbf{x})$. The description of non-collinear systems is accomplished by a rotation of the local coordinate system [43]. The contribution of an electron at the position $\mathbf{x}$ to the total XC energy can consequently be approximated with the XC energy per electron of a homogeneous electron gas with the spin density of the inhomogeneous system at the position $\mathbf{x}$ of the electron

$$E_{XC}[n_\sigma] = \int \mathrm{d}^3\mathbf{x} n(\mathbf{x}) \epsilon_{XC}^{hom}[n_\sigma] \mid_{n_\sigma = n_\sigma(\mathbf{x})} . \tag{2.21}$$

This implies, that the non-collinear description, which has been introduced in section 2.2.1, is now replaced by a locally collinear treatment of the electron spins. This is justified by the assumption of slowly varying densities. The XC energy of a homogenous electron gas can be expressed by a sum over the exchange $\epsilon_X^{hom}[n_\sigma]$ and the correlation $\epsilon_C^{hom}[n_\sigma]$ part:

$$\epsilon_{XC}^{hom}[n_\sigma] = \epsilon_X^{hom}[n_\sigma] + \epsilon_C^{hom}[n_\sigma]. \tag{2.22}$$

While analytical expressions for the exchange energy $\epsilon_X^{hom}[n_\sigma]$ were derived, for example by Perdew and Zunger [44], the exact determination of the correlation energy $\epsilon_C^{hom}[n_\sigma]$ is not possible. The most suitable values for the correlation energy are obtained within the parametrization by Perdew and Zunger [44], which is obtained [45] by a fit to Monte-Carlo results of Ceperly and Alder [46] for low electron densities and a fit to the high-density limit of Gell-Mann and Brueckner [47]. The dependence on the spin polarization is added following the idea of von Barth and Hedin [39].

Despite the formal restriction to systems with slowly varying densities, the LSDA turns out to yield remarkably reasonable results even for systems, where the density is strongly varying such as nanocrystals. This is caused by the cancellation of different errors within the correlation energy [48]. Generally, the L(S)DA leads to a significant overbinding, i.e. to an underestimation of bond lengths [49]. Since the DFT is a ground-state theory, excitation effects are not considered. This results in Kohn-Sham gaps, which drastically underestimate the measured quasiparticle gaps.

Interpreting the L(S)DA XC energy functional (2.21) as zeroth order of a series expansion of the real XC energy at the position $\mathbf{x}$, a possible improvement is to additionally include spin-density gradients. This so-called Generalized Gradient Approximation (GGA), that regards for gradient corrections to the exchange and correlation energy (PW86 [50] and PW91 [51]), was introduced by Perdew and

Wang. The most frequently applied GGA XC functional is the parametrization according to the Perdew-Burke-Ernzerhof (PBE) method [52]. In contrast to the LDA, the GGA tends to overestimate bond lengths and still significant energy gap underestimations [53].

2.2.3.3 Hybrid functionals

Since the Hartree-Fock theory yields the exact non-local and orbital-dependent exchange interaction, but neglects the correlation energy, it is obvious, that an inclusion of the HF exchange to a certain extend in the LSDA or GGA XC functional leads to a more reliable description of the electronic system, since non-local effects are taken into account [48]. Several parametrizations for the XC energy combining the correlation from LDA or GGA functionals and the Hartree-Fock-like exchange energy have been proposed [54–56]. The exchange interaction is divided into a long-range E_X^l and a short-range part E_X^s [57]. The long-range part of the Hartree-Fock exchange $E_X^{HF,l}$ is replaced by a semilocal exchange energy $E_X^{PBE,l}$ (see Sec. 2.2.3.2) obtained from GGA functionals simulating an effective screening of the Coulomb interaction. The correlation energy is taken from PBE or L(S)DA functionals. This parametrization is known as the HSE06 XC functional [28, 58].

2.2.3.4 Becke-Johnson-type approximations

The main problem with the use of hybrid functionals is the large computational effort due to the non-locality of the short-range Fock exchange, which significantly limits the describable system size. A possibility to overcome these problems is the development of (semi)local XC functionals, which model important aspects of excitation properties, for example the Becke-Johnson functionals. Becke-Johnson type XC functionals provide a possibility to obtain reliable band gaps, while the computational cost is comparable to common LSDA/GGA calculations.

The Becke-Johnson type XC potentials are based on the idea to reproduce the shape of the exact exchange of optimized effective potentials (OEP) for atoms [59, 60]. The OEPs are local exchange potentials. The corresponding orbitals minimize the total energy of the Slater determinant and can be determined exactly for spherical atoms. However, the determination of the OEP requires the solution of a difficult integral equation involving two-electron integrals resulting in a huge computational effort and numerical instability [61, 62].

In 2006, Becke and Johnson [61] proposed an approximate, local, effective exchange potential that closely reproduces the shape the exact exchange of the OEP by Talman-Shadwick [60] purely depending on densities without the necessity to

solve two-electron integrals. The correlation energy is taken from L(S)DA computations. However, this approach still significantly underestimates energy gaps .

Tran and Blaha [27] suggested a modification of the Becke-Johnson exchange potential depending on the electron density and its derivatives. As described in the case of the LSDA (see Sec. 2.2.3.2), the spin is treated locally collinear. The modified Becke-Johnson (MBJ) exchange potential is given as

$$v_{X,\sigma}^{\mathrm{MBJ}}(\mathbf{x}) = c v_{X,\sigma}^{\mathrm{BR}}(\mathbf{x}) + (3c-2)\frac{1}{\pi}\sqrt{\frac{5}{12}}\sqrt{\frac{2t_\sigma(\mathbf{x})}{n_\sigma(\mathbf{x})}} \tag{2.23}$$

with the spin density $n_\sigma = \sum_{i=1}^{N_\sigma} |\phi_\sigma^i|^2$, and the kinetic-energy density $t_\sigma = \frac{1}{2}\sum_{i=1}^{N_\sigma} \nabla\phi_\sigma^{i*}\nabla\phi_\sigma^i$. N_σ is the number of electrons in the spin channel σ. $v_{X,\sigma}^{\mathrm{BR}}(\mathbf{x})$ denotes the Becke-Russel potential [63]:

$$v_{X,\sigma}^{\mathrm{BR}}(\mathbf{x}) = -\frac{1}{b_\sigma(\mathbf{x})}\left(1 - e^{-x_\sigma(\mathbf{x})} - \frac{1}{2}x_\sigma(\mathbf{x})e^{-x_\sigma(\mathbf{x})}\right). \tag{2.24}$$

$x_\sigma(\mathbf{x})$ is a function depending on the electron density, and its first and second spatial derivatives, while $b_\sigma(\mathbf{x}) = (x_\sigma^3 e^{-x_\sigma}/(8\pi n_\sigma))^{\frac{1}{3}}$ depends on x_σ [27]. However, due to the inclusion of the free parameter $c = a + b\left(\frac{1}{V_{\mathrm{cell}}}\int_{\mathrm{cell}}\frac{|\nabla n_\sigma(\mathbf{x}')|}{n_\sigma(\mathbf{x}')}\mathrm{d}^3\mathbf{x}'\right)^{\frac{1}{2}}$, where a and b on their part are free parameters as well, the MBJ exchange functional is no longer *ab-initio*. Similar to the LSDA, a non-collinear description is replaced by a locally collinear treatment of spins.

The semilocal MBJ exchange functional in equation (2.23) is very similar to the L(S)DA for a constant electron density. In combination with the correlation energy taken from L(S)DA calculation, the band gaps of solids can be computed in good agreement with experiments, while the computational effort is comparable to L(S)DA calculations [27, 64]. Due to the inverse dependence on the spatial density derivatives, the MBJLDA becomes unstable, when it is applied to systems with large electron density gradients such as surfaces, i.e., boundaries between material and vacuum. Therefore, this approach can be only applied to nearly homogeneous systems, especially with respect to the kinetic-energy density.

2.2.4 Relativistic corrections

So far, relativistic effects have been neglected. However, the importance of relativistic corrections within the description of the electron moving in the electrostatic potential of the nuclei and the other electrons increases with increasing nuclear weight. The relativistic Hamiltonian of an electron moving in a spherical potential $V(r)$ with the velocity $\mathbf{v} = \frac{\mathbf{p}}{m}$, the momentum $\mathbf{p}$, the spin $\mathbf{s}$, and the angular mo-

mentum $\mathbf{l}$, can be expanded in a power series of $|\mathbf{v}|/c$, with c the speed of light [65], which yields three main relativistic corrections. The scalar relativistic effects of the so-called Darwin term and the dynamic mass correction, which are given by

$$H_s = -\frac{\mathbf{p^4}}{8m_e^3c^2} + \frac{\hbar^2}{8m_e^2c^2}\Delta V(r), \tag{2.25}$$

are commonly considered within the pseudopotential generation [66] (see Sec. 2.3.3). Another important contribution is the spin-orbit interaction

$$H_{SO} = \frac{1}{2m_e^2c^2}\frac{1}{r}\frac{\mathrm{d}V(r)}{\mathrm{d}r}\mathbf{l}\cdot\mathbf{s}. \tag{2.26}$$

It is included as an additional contribution in the Kohn-Sham Hamiltonian in equ. (2.3) within the PAW sphere (see Sec. 2.3.3). The potential $V(r)$ is approximated by the spherical contributions of the local potential inside the PAW sphere, which is reasonable, since the multi-pole expansion of the potential in the vicinity of the nuclei is dominated by spherical symmetric terms.

2.3 Numerical concepts

So far, possibilities for the solution of the many-particle problem were introduced. In the present section, concepts of the numerical implementation are discussed. The results presented in this thesis were obtained using the DFT-software VASP (Vienna *ab-initio* simulation package [67, 68]). The solutions of the Kohn-Sham equations are expanded in a plane wave basis set outside the PAW spheres (see Sec. 2.3.3) and atomic positions are relaxed using a conjugate-gradient or a quasi-newton algorithm, respectively. For reasons of numeric stability, after each structural iteration step, the old electron density is not simply replaced by the new one, but the old and the new densities are mixed via the *Broyden-Pulay procedure* [69, 70].

2.3.1 Determination of the ground-state geometry

The obtain the electronic and optical properties of a crystal from the solution of a many-electron problem in the fixed external potential requires the knowledge of the ground-state atomic geometry. However, the ground-state configuration of the atomic cores depends on the electrostatic interaction between the cores and the interaction between the cores and the electron density. Because the geometry defines the external potential, which, in turn, determines the electron density, this problem is not trivial. The idea for an approximate solution is to minimize the forces acting

on the ions for fixed electron density. According to the Hellmann-Feynman theorem [71, 72], these forces are equal to the gradient of the total energy given by the sum of the potential energy from the core-core interaction and that of the electronic system. After the minimization of these forces by means of a displacement of the atomic positions, the electronic ground-state for the external potential resulting of the new crystal geometry is computed, assuming that the electrons instantaneously follow the displacement of the cores, in accordance with the Born-Oppenheimer approximation. This relaxation procedure is repeated until either the total energy of the system or the atomic forces are converged to a sufficient abort criterion. For the actual calculations, a conjugate-gradient algorithm was applied to minimize the Hellmann-Feynman forces acting on the atoms in the bulk unit cell and the nanocrystals below 5 and 20 meV/Å, respectively, in order to obtain the ground-state bulk lattice constants and the ground-state geometry of the nanocrystals. For NCs with more than 147 tin atoms, a abort criterion of 50 meV/Å had to be applied due to the computational effort. In the case of surface and interface calculations, no structural relaxation was performed. For the electronic relaxation, a total energy difference of 10^{-4} eV between two steps was used as convergence criterion for all calculations.

To determine the lattice constant a_0 of a face-centered cubic (fcc) crystal, the total energy of the unit cell depending on the unit cell volume is calculated by a variation of the lattice constant. Finally, this volume dependence is fitted to the Murnaghan equation of state [73] to obtain the energy minimum and the corresponding lattice parameter. For each lattice parameter, the atomic positions are relaxed such that the forces acting on the atoms are below 5 meV/Å.

2.3.2 Plane-wave expansion

Due to the translational symmetry of crystalline systems, it is appropriate, to expand the Kohn-Sham spinor wave functions $\phi_\alpha^{\nu\mathbf{k}}(\mathbf{x})$ (see Sec. 2.2.2) into an orthonormal plane-wave basis set [74]:

$$\phi_\alpha^{\nu\mathbf{k}}(\mathbf{x}) = \frac{1}{V}\sum_{\mathbf{G}} c_\alpha^{\nu\mathbf{k}}(\mathbf{G}) e^{i(\mathbf{k}+\mathbf{G})\mathbf{x}}. \tag{2.27}$$

Here, $\mathbf{k}$ are vectors inside the Brillouin zone (BZ) and $\mathbf{G}$ are reciprocal lattice vectors and ν denotes the band index. The size of the basis set and the associated numerical effort is determined by the introduction of the energy cutoff $E_{cut} = -\frac{\hbar^2}{2m_e}|\mathbf{G}_{cut}|^2$, restricting the plane waves to $(\mathbf{k}+\mathbf{G}) < \mathbf{G}_{cut}$. A huge advantage of this plane-wave expansion is, that the resulting Kohn-Sham orbitals automati-

cally fulfill the Bloch-theorem $\phi_\alpha^{\nu\mathbf{k}}(\mathbf{x}+\mathbf{R}) = e^{i\mathbf{k}\mathbf{R}}\phi_\alpha^{\nu\mathbf{k}}(\mathbf{x})$. In addition, plane waves are eigenfunctions of the momentum operator, and, hence, the kinetic energy term in equ. (2.18) becomes diagonal. In the present work, we use a plane-wave cutoff of $E_{cut} = 500$ eV for the bulk calculations. The calculation of low-dimensional systems is computationally much more expensive and requires a reduction of the plane wave basis set. These cutoffs are specific for each pseudopotential and amount to $E_{cut} = 103$ eV (Sn), $E_{cut} = 233$ eV (Hg), $E_{cut} = 274$ eV (Cd), $E_{cut} = 175$ eV (Te), $E_{cut} = 96$ eV (In), $E_{cut} = 172$ eV (Sb), and $E_{cut} = 250$ eV (H). For structures, which contain more than one species of atoms, the highest value of the respective plane-wave cutoffs is applied.

The plane-wave coefficients can be obtained inserting (2.27) in equ. (2.18), multiplying with $e^{-i(\mathbf{k}+\mathbf{G})\mathbf{r}}$ and integrating over the real space. Thereby, an algebraic eigenvalue problem for the plane-wave coefficients is obtained. Its numerical solution requires the discretization of the Brillouin zone. The number of $\mathbf{k}$ points, which is necessary to assure the convergence of eigenvalues and eigenfunctions, can be significantly reduced taking advantage of the symmetry operations of the BZ, which allows to constrain the $\mathbf{k}$ sampling only to the symmetry-irreducible part of the BZ. In the present work, Γ-centered Monkhorst-Pack $\mathbf{k}$-point meshs [75] are used, because the electronic properties at the Γ-point are crucial especially in the case of low-dimensional systems. In the case of bulk calculations 12×12×12 Γ centered Monkhorst-Pack mesh was used, which in combination with the used total-energy cutoff assures an accuracy of 1 meV of the total energy of the unit cell. For the sampling of surface- and interface unit cells (see Sec. 2.3.4), 6×6×1 [6×4×1] $\mathbf{k}$ points were used in the case of (001) [(110)] orientation, respectively. The large lattice vector in direction of the interface (surface) normal (see Sec. 2.3.4) makes the BZ almost two-dimensional (2D), which allows for the two-dimensional sampling. As the unit cell used for the simulation of nanocrystals is largely extended in all three directions, the resulting BZ is infinitesimal, and, hence, the BZ sampling can be restricted to the Γ point.

2.3.3 Frozen-core approximations and pseudopotentials

Despite the significant reduction of the number of degrees of freedom of the many-body problem within the Kohn-Sham formalism, the description of large systems containing several hundred of atoms, is numerically too expensive, if all electrons are considered. Therefore, it is assumed, that only the valence electrons contribute significantly to the chemical bonding between atoms and, hence, have a strong impact on the electronic properties of the system. It is therefore possible, to restrict

the calculations to the valence electrons and to construct an effective atomic core consisting of the strongly localized electrons in the vicinity of the nucleus and the actual core. As the numerical effort scales asymptotically with the number of electrons cubed, this method allows for the treatment of much larger systems than an all-electron treatment. In the present thesis, the following valence electron configurations are considered:

$$\begin{aligned} [\mathrm{Sn}] &= 5s^2 5p^2 \\ [\mathrm{Hg}] &= 5d^{10} 6s^2 \\ [\mathrm{Te}] &= 5s^2 5p^4 \\ [\mathrm{Cd}] &= 4d^{10} 5s^2 \\ [\mathrm{In}] &= 5s^2 5p^1 \\ [\mathrm{Sb}] &= 5s^2 5p^3. \end{aligned} \tag{2.28}$$

(2.29)

The semicore d-electrons of Hg and Cd are so shallow, that they are described as valence states. In the case of some of the bulk calculations and small nanocrystals, additionally the Sn $4d$ electrons were taken into account for the purpose of comparison.

In the core region, the Coulomb potential becomes singular. Its description within the plane-wave expansion would significantly increase the required plane wave cutoff, and, hence, the numerical effort. Therefore, the interaction of the valence electrons with the cores are modeled by pseudopotentials constructed within the Projector-Augmented wave (PAW) method [76] inside a spherical area around the nuclei, the so-called PAW sphere. Products of Kohn-Sham wave functions inside a PAW sphere are described by a projection technique applying the wave functions of an all-electron calculation for free atoms [76].

2.3.4 Modeling of low-dimensional systems

The plane-wave expansion of the wave functions within VASP restricts the calculations to systems with three-dimensional translational symmetry. However, low-dimensional systems such as interfaces, surfaces and nanocrystals violate the translational symmetry in one or three directions, respectively. This problem is avoided by the implementation of an artificial translational symmetry due to the construction of so-called supercells and their repeated application [77]. In the case of a

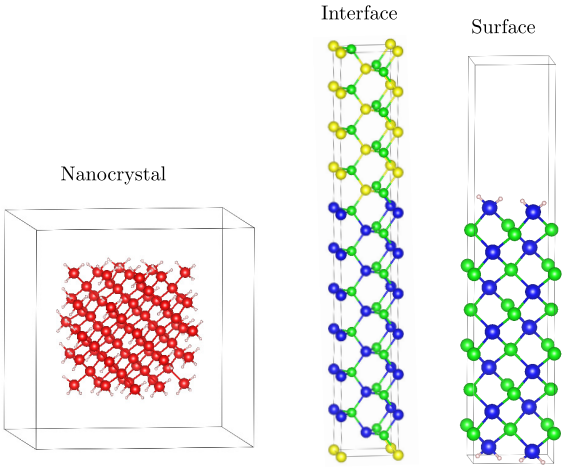

Figure 2.1: Supercells as used for simulation of nanocrystals, interfaces and surfaces.

nanocrystal, the crystal is placed in the center of a cubic supercell, surrounded by vacuum as depicted in Fig. 2.1. This vacuum layer must be sufficiently large to prevent an interaction between the NCs in adjacent supercells. The modeling of surfaces is very similar. The respective supercell is partly filled with material, the other part is made up by vacuum. Thereby, a transition between bulk material and vacuum,i.e., a surface with a certain orientation, is modeled. For the simulation of an interface between two materials, the vacuum part of a surface unit cell is simply replaced by the respective second material (see Fig. 2.1). In both cases, the elongation of the supercell must be large enough to decouple interfaces or surfaces between adjacent supercells.

2.4 Optical properties

The imaginary part of the frequency-dependent dielectric function $\varepsilon(\omega)$ within the independent-quasiparticle approximation is used to describe the optical absorption properties. Excitonic effects are neglected [78]. In the NC case we assume, that the confinement effects overcome the excitonic effects. For positive frequencies it holds

$$\begin{aligned} \text{Im } \varepsilon_{ii}(\omega) \quad = \quad & \frac{e^2\pi\hbar^2}{\epsilon_0 m\Omega_0}\frac{1}{N}\sum_{\mathbf{k}}\sum_{c,v}\frac{2m|\langle c\mathbf{k}|\mathrm{v}_i|v\mathbf{k}\rangle|^2}{[\epsilon_c(\mathbf{k})-\epsilon_v(\mathbf{k})]^2}\times \\ & \times\delta(\epsilon_c(\mathbf{k})-\epsilon_v(\mathbf{k})-\hbar\omega)\ . \end{aligned} \tag{2.30}$$

Here, $|c\mathbf{k}\rangle$ and $|v\mathbf{k}\rangle$ are the wave functions of conduction and valence states, respectively, which are Pauli-Spinors due to the non-collinear spins because of the inclusion of spin-orbit coupling, and $\epsilon_c(\mathbf{k})$ and $\epsilon_v(\mathbf{k})$ are the eigenenergies of the respective band states. N denotes the number of $\mathbf{k}$ points. The optical transition

matrix elements $\langle c\mathbf{k}|v_i|v\mathbf{k}\rangle$ are given by the ith Cartesian components of the velocity operator v_i between the valence and conduction states. Ω_0 denotes the volume of the BZ. For the actual calculations, the longitudinal approach [79] is used to compute the matrix elements of the velocity operator for vanishing wave vectors $\mathbf{q}$ parallel to the ith Cartesian axis:

$$\langle c\mathbf{k}|\mathrm{v}_i|v\mathbf{k}\rangle = \lim_{q_i||\to 0} \frac{1}{\hbar}(\epsilon_c(\mathbf{k}) - \epsilon_v(\mathbf{k}))\frac{1}{|\mathbf{q}|}\langle c\mathbf{k}|e^{iq_i x_i}|v\mathbf{k}\rangle. \tag{2.31}$$

For cubic crystals like α-Sn, and also in the case of nanocrystals with wit T_d symmetry described in simple cubic supercells, the optical properties are isotropic, $\varepsilon(\omega) = \varepsilon_{xx}(\omega) = \varepsilon_{yy}(\omega) = \varepsilon_{zz}(\omega)$. Therefore, in the following, only the scalar $\varepsilon(\omega)$ will be considered, and the tensor character will be neglected. The real part of the dielectric function is obtained by a Kramers-Kronig transformation.

In the case of nanocrystals, additionally photoluminescence spectra and the radiative lifetimes of the excited states are of interest. For the calculation of the photoluminescence spectra, an occupation inversion between the highest occupied and the lowest unoccupied level is considered, and, hence, only the contribution of the respective transition is taken into account in equation (2.30).

The radiative lifetime τ of such an occupation inversion at an absolute temperature T is given by the thermally averaged recombination rate[80]

$$\tau = \frac{\sum_{c,v} \exp\left[-(\epsilon_c(\mathbf{k}) - \epsilon_v(\mathbf{k}))/k_B T\right]}{\sum_{c,v} W_{cv}(\mathbf{k}) \exp\left[-(\epsilon_c(\mathbf{k}) - \epsilon_v(\mathbf{k}))/k_B T\right]}, \tag{2.32}$$

with the Boltzmann constant k_B and the radiative recombination rate

$$W_{c,v}(\mathbf{k}) = \frac{16\pi^2}{3} n \frac{e^2}{4\pi\epsilon_0 h^2 m^2 c^3} \frac{1}{3} \sum_{i=x,y,z} (\epsilon_c(\mathbf{k}) - \epsilon_v(\mathbf{k}))|\langle v\mathbf{k}|\mathrm{v}_i|c\mathbf{k}\rangle|^2 \ . \tag{2.33}$$

between a conduction and a valence state. Here, n is the refractive index of the effective medium consisting of the NCs and their environment. We study freestanding NCs in vacuum, and, hence, set $n = 1$. Since most experiments are performed at room temperature, we set $T = 300$ K. Finally, it has to be mentioned, that the thermalization taken in expression (2.32) means that the thermalization of electrons and holes after their injection is assumed to be more efficient than the radiative (or non-radiative) recombination [80–82].

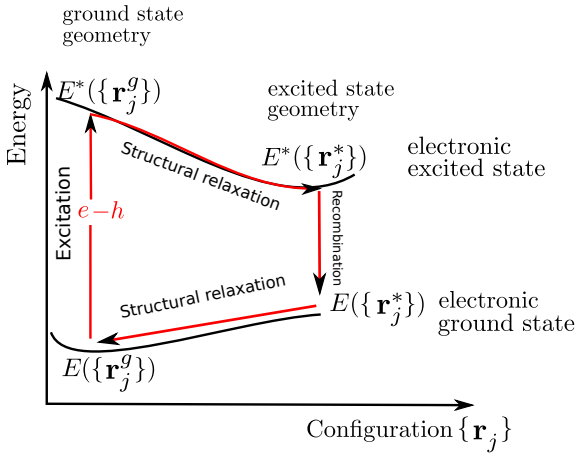

Figure 2.2: Schematic description of the computation of the lowest two-particle excitation energies for nanocrystals within the ΔSCF method.

2.4.1 Approaches for the determination of the excitation energy of zero-dimensional systems

The main problem with the calculation of band gaps including quasiparticle effects and screened Coulomb interaction is, that the computational effort is too large to be sustained for large supercells. However, for zero-dimensional systems without energy band dispersion there is a simple method for the computation of the lowest two-particle excitation energy including both, excitonic and quasiparticle, effects [49]. The method is schematically described in Fig. 2.2. The main idea is to compute the lowest neutral pair excitation energy E^{ex} of the NC from the total energy difference of two self-consistent field (ΔSCF) DFT-LDA calculations.

The neutral pair excitation of the system is modeled by an occupation constraint. An electron is taken from the highest occupied molecular orbital (HOMO), which remains unoccupied, and placed into the lowest unoccupied molecular orbital (LUMO), such that an electron-hole pair is created while the system remains electronically neutral. For degenerated HOMO (LUMO) states, the electron (hole) is averaged over the degenerated states. We assume the electronic excitation to be rather fast such that the atomic ground-state positions $\{\mathbf{r}_j^g\}$ remain unchanged. The lowest pair-excitation energy which should also be observable in optical absorption spectra [83] is then given as the difference of the total energies of the electronically excited system $E^*(\{\mathbf{r}_j^g\})$ with an electron in the LUMO and a hole in the HOMO and the system in the electronic ground-state $E(\{\mathbf{r}_j^g\})$, both remaining in the ground-state atomic geometry:

$$E^{ex}(\{\mathbf{r}_j^g\}) = E^*(\{\mathbf{r}_j^g\}) - E(\{\mathbf{r}_j^g\}) \ . \tag{2.34}$$

The reliability of the lowest two-particle excitation energies obtained within this method has been demonstrated for colloidal and embedded nanocrystals [84–87].

As depicted in Fig. 2.2, the ΔSCF method does also allow for the computation of optical emission properties. The emission does not appear immediately after excitation such that the system has time to minimize its total energy by a relaxation of the atomic geometry in the presence of the electron-hole pair. The total energy of the energetically excited system in the resulting excited-state geometry $E^*(\{\mathbf{r}_j^*\})$ is computed within DFT-LDA by a structural relaxation of the NC with the described occupation constraint that simulates the electron-hole pair. After the structural rearrangement, the recombination of the electron-hole pair takes place and is again assumed to be fast enough such that the system remains in the excited-state geometry during the recombination. Due to the recombination the system transitions from the electronically excited system within the excited-state geometry to the system in electronic ground-state but still within the excited state geometry with the total energy $E_g(\{\mathbf{r}_j^*\})$. The energy of the photon emitted in photoluminescence is the difference between the total energies of two systems in the excited-state geometry before and after recombination

$$E^{ex}(\{\mathbf{r}_j^*\}) = E^*(\{\mathbf{r}_j^*\}) - E(\{\mathbf{r}_j^*\}) \ . \tag{2.35}$$

The photoluminescence energy is consequently red-shifted with respect to the lowest pair-excitation energy, which is associated with the lowest absorption energy. The energetic difference between absorption and emission is known as the optical Stokes shift [88, 89]

$$\Delta_{\text{Stokes}} = E^{ex}(\{\mathbf{r}_j^g\}) - E^{ex}(\{\mathbf{r}_j^*\}) \ . \tag{2.36}$$

After the recombination of the electron-hole pair, the atomic geometry moves into its ground-state configuration again.

2.5 Studied structures

2.5.1 Diamond and zinc-blende structures

All bulk materials studied within this thesis crystallize either in the diamond or zinc-blende structure (see Fig. 2.3(a)). The unit cell is spanned by the primitive basis vectors $\mathbf{a}_1 = (\frac{1}{2}, \frac{1}{2}, 0)$, $\mathbf{a}_2 = (\frac{1}{2}, 0, \frac{1}{2})$, and $\mathbf{a}_3 = (0, \frac{1}{2}, \frac{1}{2})$. In both structures,

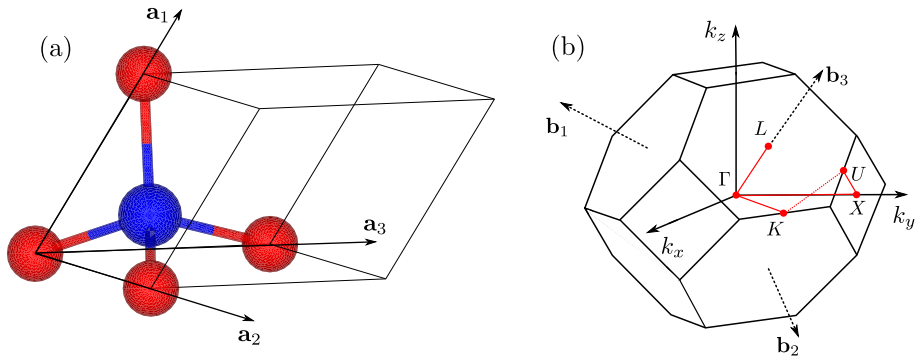

Figure 2.3: (a) Unit cell and atomic positions in a zinc-blende crystal. In the case of a diamond lattice, there is only one species of atoms. The primitive basis vectors are indicated. (b) First Brillouin zone of the fcc lattice. The high-symmetry points and lines, that will be referred to in the next chapters are indicated by red dots and lines, respectively. The primitive lattice vectors $\mathbf{b}_i$ of the reciprocal lattice and the corresponding Cartesian axes are depicted.

the lattice symmetry is face-centered cubic (fcc) with two atoms in the atomic basis at (0,0,0), and $(\frac{1}{4},\frac{1}{4},\frac{1}{4})$ in units of $\mathbf{a}_i$ with $i = 1,2,3$. In the case of the diamond structure, both atoms in the unit cell belong to the same atomic species (e.g. α-Sn), while in the zinc-blende structure (e.g. HgTe, CdTe, and InSb) two different atomic species occur. Every atom is tetrahedrally coordinated to four other atoms with bond angles of $\alpha = 109.4°$. In a zinc-blende crystal, only bonds between different atomic species occur as can be seen from Fig. 2.3. The first Brillouin zone of the zinc-blende and the diamond structure including the high-symmetry points is also depicted in this figure.

α-Sn crystallizes in the diamond structure, while the other considered materials possess zinc-blende structure. The bulk lattice constants derived within the DFT-LDA approach are $a_0 = 6.475$ Å (α-Sn), 6.450 Å (HgTe), 6.460 Å (CdTe) and 6.472 Å (InSb). Therefore, the two latter materials are ideal substrates for the growth of α-Sn and HgTe films because of the same lattice symmetry and the small lattice mismatch. The calculated lattice constant of α-Sn is in agreement with the values measured by Farrow [90] and Davey [91] using X-ray diffraction. A slight underestimation of 5 mÅ (Ref. [90]) and 15 mÅ (Ref. [91]), respectively, within DFT-LDA can be explained by the well-known tendency of the LDA to underestimate bond lengths [51]. The optimized lattice constants of the zinc-blende materials $a_0 = 6.45$ Å (HgTe) and $a_0 = 6.46$ Å (CdTe) slightly deviate from the experimental values $a_0 = 6.453$ Å (HgTe) and $a_0 = 6.48$ Å (CdTe) [92], and $a_0 = 6.48$ Å (InSb) [93], respectively, because of the used XC potential in LDA. However, in another data collection a measured value of $a_0 = 6.460$ Å [94] (CdTe),

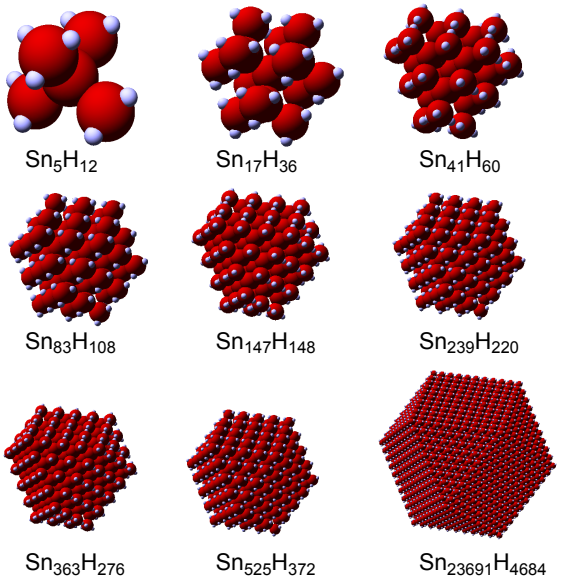

Figure 2.4: Atomic geometries of the studied α-Sn NCs. Tin atoms are depicted as red spheres, while hydrogen atoms are marked white.

much closer to the theoretical lattice constant, has been published.

Despite the fact, that that the space-group symmetries of α-Sn and HgTe (CdTe, InSb) are different, we use the same denotation of energy levels for diamond and zinc blende in order to unify the discussion. Especially, the s-derived Γ_{7c}^{+} level of α-Sn will be here denoted as Γ_{6c} as in the HgTe (CdTe, InSb) case applying the double-group notation [32, 95].

2.5.2 Modeling of α-Sn NCs

Simple cubic supercells are used for the modeling of α-Sn nanocrystals. The nanoclusters are modeled based on a central Sn atom adding other atoms shell by shell according to the tetrahedral coordination of the bulk diamond structure. This construction principle conserves the point-group T_d symmetry of bulk α-Sn[96], which allows for the NC wave functions to be linear combinations of bulk-symmetry wave functions. This construction principle leads to NCs with N_{Sn} =1, 5, 17, 41, 83, 147, 239, 363, and 525 total numbers of tin atoms, corresponding to N_{shell} =0, 1, 2, 3, 4, 5, 7, and 8 numbers of shells, respectively. The edge lengths of the supercells were chosen as integer multiples $n \cdot a_0 = 6.4746$ Å of the α-Sn lattice constant with n =3, 3, 3, 3, 4, 4, 5, 6 in ascending order of the NC size. This assures a decoupling of the NCs in neighboring supercells, because they are separated by more than 15 Å vacuum.

The shape of the NCs, which is depicted in Fig. 2.4, is that of a cubooctahedron

and corresponds to cubes with (001) surfaces with the corners cut off perpendicular to [111] direction forming triangular faces, that connect the midpoints of the rectangular facets at the respective corners. The surface of the NCs therefore exhibits six rectangular {001} and eight equilateral triangular {111} facets. These facets exhibit an alternating behavior with respect to the number of shells. The clusters with even numbers of shells exhibit square {001} facets and, consequently, all {111} facets have the same size. In the cases of odd shell number, the {001} facets form rectangles with the edge length differing by one atom. Hence, there are two different {111} facets with edge lengths according to the two different edge lengths of the rectangular {001} facets.

The Sn atoms at the surface of the NCs exhibit dangling bonds, that would lead to electronic surface states. However, the topic of this work is the investigation of the influences of nanostructuring on the electronic structure undisturbed by these surface states. Therefore, the dangling bonds are saturated with hydrogen atoms to shift the dangling bond states out of the energy region of the fundamental gap [97]. The tin atoms at the {001} ({111}) facets possess two (one) dangling bonds, while some atoms located at the edges between differently orientated facets exhibit three dangling bonds. The total number of passivating hydrogen atoms needed in ascending order of the NC size is N_H =4, 12, 36, 60, 108, 148, 220, 276, and 372. They are positioned in the direction of the dangling bonds in a distance of 1.73 Å from the respective tin atom. This bonding distance of 1.73 Å between Sn and H atoms was determined by a structural minimization of the total energy of the Sn_1H_4 cluster and is in close agreement with the sum of the covalent radii of Sn and H [98].

2.5.3 Modeling of (001) and (110)-orientated interfaces

A CdTe/HgTe/CdTe QW structure with a HgTe layer thickness d_1 is modeled by a unit cell with a sufficient thickness d_2 of the CdTe barrier layers as displayed in Fig. 2.5. Two growth directions [001] and [110] are studied. The (110) surface is the common cleavage face of all zinc-blende crystals. In practice, we investigate $(A)_N(CdTe)_M(001)$ and $(A)_N(CdTe)_M(110)$ superlattices with N atomic monolayers of the well material A=α-Sn or A=HgTe, and the corresponding number of atomic monolayers M in the CdTe case. To keep the notation consistent for all materials and orientations, we use the number atomic layers instead of the number of symmetry-irreducible parts of the slabs to label the structures. Since the $(001)\sqrt{2}\times\sqrt{2}$ [$(110)1\times1$] surface unit cells are squares [rectangles], the superlattices with a lattice constant (d_1+d_2) defined by the $(N+M)$ atomic layers possess a tetrag-

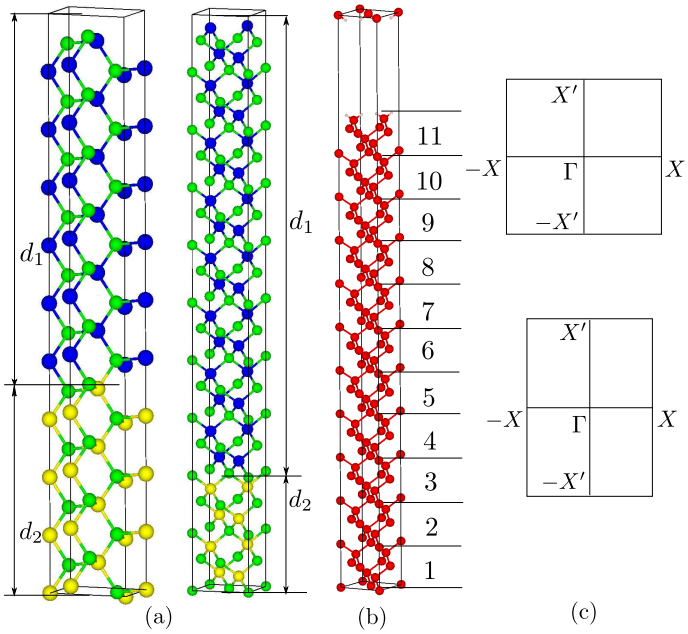

Figure 2.5: (a) Supercells, that are used for the modeling of (110) and (001) quantum wells. Exemplarily, a $(HgTe)_{24}(CdTe)_8(110)$ ($(HgTe)_{32}(CdTe)_8(001)$) is depicted in the left (right) panel. The Cd (Hg, Te) atoms are shown as yellow (blue, green) dots. (b) A $\sqrt{2}\times\sqrt{2}(001)$ α-Sn surface slab. The symmetry-irreducible parts are numbered. Tin atoms are depicted red, while the passivating hydrogen atoms are marker white. In (c) the two-dimensional Brillouin zone of a quadratic (rectangular) 2D unit cell of an interface/surface is depicted together with the corresponding high-symmetry points.

onal [orthorhombic] symmetry. As examples the unit cells of a $(HgTe)_{12}(CdTe)_8(110)$ superlattice, and a $(HgTe)_{16}(CdTe)_8(001)$ superlattice are displayed in Fig. 2.5.

In the case of (001) and [(110)]-oriented HgTe QWs, the two interfaces per superlattice (SL) unit cell, Te-Hg and Te-Cd (CdTe-HgTe and HgTe-CdTe) are polar (nonpolar). However, the irreducible part, which contains four (two) atomic layers in the case of (001) [(110)]-orientation [77], of the slabs are still electronically neutral, and, hence, stoichiometric barriers are used. The number $M = 8$ of atomic monolayers of the barrier material is fixed both cases. It results in a CdTe thickness $d_2 = 1.6$ nm (1.13 nm) using the DFT-LDA lattice constant for (110) [(001)]. It is sufficiently thick to confine electrons and holes in the HgTe layers.

In the case of α-Sn/CdTe(110) QWs, the same supercells as for the respective HgTe QWs are used, because the atomic layers in the barrier material contain one Cd and on Te ion and are therefore electrostatically neutral. In α-Sn/CdTe(001) QWs, however, the CdTe barrier consists of atomic layers containing either Cd or Te ions. To obtain equivalent bonds between the two materials, i.e. the same terminations of the CdTe barrier (Te termination in the actual calculations), on the two interfaces in the supercells, non-stoichiometric CdTe barriers must be used. In

the actual calculations, we set $M = 11$, which yields the stoichiometry $Cd_{10}Te_{12}$.

We assume, that only the α-Sn (HgTe) layers are strained to adapt the lattice mismatch[99]. In the explicit calculations we fix the in-plane lattice constants in accordance to the cubic lattice constant of CdTe, as derived by means of DFT-LDA. Then, using the ratio $R_b = R_b = -\frac{2C_{12}}{C_{11}} = -0.85$ [100] (-1.37) of α-Sn [101] (HgTe) of the elastic constants, characterizing the biaxial strain due to the lattice misfit, and the misfit between the DFT-LDA lattice constants, the distances between layers in [001] ([110]) direction are determined. The electronic structure results are presented in a square (rectangular)-shaped BZ for the (001) [(110)] systems, which are also displayed in Fig. 2.5.

In some calculations, InSb is used as barrier material, however, the construction principle remains the same.

2.5.4 Modeling of α-Sn(001) surfaces

Only symmetric slabs consisting of N irreducible (001) slabs with four atomic layers, i.e., of $4N$ atomic layers in total, are taken into account (see Fig. 2.5). Each of the layers is biaxially strained according to the lattice mismatch to the zinc-blende substrate, on which an α-Sn film of varying thickness is assumed to be pseudomorphically grown. Such gray tin films can be indeed grown by molecular beam epitaxy on CdTe(001) wafers [102, 103].

A strain value of -0.23 % results from the difference in the lattice constants $a_{\mathrm{Sn}} = 6.475$ Å and $a_{\mathrm{CdTe}} = 6.46$ Å (see Sec. 2.5.1). Because of the elastic properties of α-Sn this biaxial strain induces an increase of the layer distances in [001] direction by 0.19 %. Consequently a tetragonal crystal structure with characteristic atomic distances close to those of the unstrained diamond crystal appears. For the purpose of comparison, results for vanishing strain are also presented.

The (001) surface exhibits two half-filled dangling bonds per surface Sn atom. They may give rise to a 2×1 reconstruction with resulting dimer-derived bands near the Fermi level [77]. Here, we passivate each dangling bond by one hydrogen atom in the direction of the dangling bond. In principle, a 1×1 surface could be studied. However, since the clean surface or the surface passivation by Bi [24] leads to a 2×1 reconstruction, here we study larger surface unit cells. To simplify the symmetry considerations we investigate square $\sqrt{2} \times \sqrt{2}$ unit cells with two surface Sn atoms and four passivating hydrogen atoms (see Fig. 2.5). The basis vectors of the two dimensional Bravais lattice point along the cubic axes [100] and [010].

2.6 Tight-Binding Description

Despite the simplifications introduced in the previous sections, the size of systems, that can be treated within DFT is restricted by the computational effort. This becomes exceedingly important, when the description of low-dimensional systems requires the usage of supercells as described in Sec. 2.3.4. Regarding the systems discussed within this thesis, in particular α-Sn NCs and α-Sn (001) surfaces, the system sizes, that can be described within *ab-initio* methods, are sufficient to show thickness-dependent trends of the electronic properties, but in order to confirm those dependencies, a computationally cheaper method is required. To model the properties of systems modeled by supercells, which contain large numbers of atoms, we use an empirical tight-binding (TB) model to investigate system sizes, which are beyond the reach of DFT. A system of independent electrons in an external potential U described by the Hamiltonian

$$H = \underbrace{\left[\frac{\mathbf{p}^2}{2m_e} + U(\mathbf{x})\right]}_{H_0} + \underbrace{\sum_j \eta_j(\mathbf{r}_j)\mathbf{l}_j \cdot \mathbf{s}}_{H_{SO}} \tag{2.37}$$

is considered. Here, H_0 consists of the kinetic energy and the potential U, which is approximated by a sum of radially symmetric potentials $V(d_j)$ located at the sites $\mathbf{r}_j$ of the atoms in the unit cell, which are labeled by j. $d_j = |\mathbf{x}-\mathbf{r}_j|$ is the distance from the site of the jth atom. If $\mathbf{R}$ denotes a lattice vector of the Bravais lattice and $\mathbf{b}_j$ are the vectors of the atomic basis, the atomic positions are given by $\mathbf{r}_j = \mathbf{R} + \mathbf{b_j}$. The second contribution to the Hamiltonian is the spin-orbit interaction, and it holds $\eta_j(d_j) \propto \frac{1}{d_j}\frac{\mathrm{d}V(d_j)}{\mathrm{d}d_j}$.

In a first step, the eigenproblem $H_0\psi_{\nu\mathbf{k}} = \epsilon_n\psi_{\nu\mathbf{k}}$ without SOC is considered. The wave functions are expanded in a basis set of Bloch sums

$$\chi_{\gamma\mathbf{k}} = \frac{1}{\sqrt{N}}\sum_{\mathbf{r}_j} e^{i\mathbf{k}\mathbf{R}}\phi_{\gamma_i}(\mathbf{x}-\mathbf{r}_j) \tag{2.38}$$

of Löwdin orbitals [104] $\phi_{\gamma_j}(\mathbf{x}-\mathbf{r}_j)$. $\mathbf{k}$ is a vector in the Brillouin zone. Those orbitals are basically combinations of atomic orbitals, which transform like the atomic orbitals themselves, but, in contrast to atomic orbitals, Löwdin orbitals located at different atoms are orthogonal to each other, which significantly simplifies the problem. Hence, we use a basis set $|\gamma_j, \mathbf{r}_j\rangle$ of Löwdin orbitals located at the sites $\mathbf{r}_j$, where γ_j is a combined index, which denotes the transformation behavior of the orbital (γ=s, p_x,...), and the atom j ($j = 1, ...N$ with N being the number of atoms), at which it is located in the unit cell. The Bloch sums are special linear combina-

tions of the Löwdin orbitals, that fulfill the Bloch theorem. Within this basis set, the eigenvalue problem of H_0 becomes a set of algebraic equations:

$$\sum_{\delta} \underbrace{\langle \chi_{\gamma\mathbf{k}} | H_0 | \chi_{\delta\mathbf{k}} \rangle}_{E_{\gamma\delta}} c_{n\delta}(\mathbf{k}) = \epsilon_n(\mathbf{k}) c_{n\gamma}(\mathbf{k}). \tag{2.39}$$

It is common, to restrict the evaluation of the matrix elements $H^0_{\gamma\delta}$ to a nearest-neighbor (NN) interaction. We use a basis set of five Löwdin orbitals, that transform like s, p_x, p_y, and p_z atomic orbitals. Following the idea of Vogl et al. [105], an additional s^* orbital is used for a more precise description of the lower conduction bands. The matrix elements of the TB Hamiltonian $E_{\gamma\delta}$ can be expressed as sums over matrix elements between Löwdin orbitals:

$$\langle \chi_{\gamma\mathbf{k}} | H_0 | \chi_{\delta\mathbf{k}} \rangle = \sum_{R} e^{i\mathbf{k}\mathbf{R}} \langle \gamma_j, 0 | H_0 | \delta_k, \mathbf{R} \rangle \tag{2.40}$$

Slater and Koster [106] proposed to use the matrix elements $E_{\gamma\delta}$ as adjustable parameters to reproduce experimental or *ab-initio* results. This procedure is frequently called empirical tight binding method (ETBM). The matrix elements in nearest-neighbor approximation of the Hamiltonian can be classified according to the localization of the involved quantities:

- On-site terms, where both atomic orbitals and the main contribution to the potential U in H_0 are located at the same atom.
- Two-center integrals, where the atomic orbitals are located at different atoms, while the center of an atomic potential is equivalent with one of them.
- Three-center integrals, where all three centers are different.

Parametrization of three-center integrals may improve the band structure results [107], but as they are difficult to describe within the modeling of surfaces, they are neglected here.

The inclusion of spin-orbit interaction requires the expansion of the basis set by the electron spin $\sigma \in \{\uparrow, \downarrow\}$: $|\gamma_j, \mathbf{r}_j\rangle \rightarrow |\gamma_j, \mathbf{r}_j\rangle \otimes |\sigma\rangle = |\gamma_j, \mathbf{r}_j, \sigma\rangle$, resulting in a basis set of Pauli spinors. Consequently, the new basis set consists of 10 Löwdin orbitals. Within this basis expansion, the elements of the Hamiltonian including spin-orbit interaction (2.37) become a sum $H_{\gamma_j\delta_k} = H^0_{\gamma_j\delta_k} + \langle \gamma_j, \mathbf{r}_j, \sigma | H_{SO} | \delta_k, \mathbf{r}_k, \sigma' \rangle$. Following the approach of Boykin [108], the evaluation of the matrix elements is restricted to the onsite and nearest-neighbor interaction. The 12 not-vanishing onsite matrix elements between p orbitals of the same atom can be reduced to one parameter λ_0

for diamond structure. This intraatomic SOC term represents the $\Gamma_{8v} - \Gamma_{7v}$ valence band splitting at the BZ center, if only on-site SOC is considered. The interatomic parameters give rise to wave-vector-induced Rashba and Dresselhaus band splittings, especially the two-fold splitting of the Γ_{8v} band along the [110] direction [109, 110]. The $s-s$, $s-s^*$, and s^*-s^* NN SOC vanishes and we neglect the $s-p$ and s^*-p NN SOC. In the case of a two-atomic diamond-structure crystal $\mathbf{R}$ is a Bravais lattice point whereas $\tau_\mathbf{1}$ represents one of the tetrahedron vectors. In this case, the four interatomic fit parameters are given by [108]

$$\eta_1 = 4i\langle x\mathbf{R}\uparrow|H_{SO}|x\mathbf{R}+\tau_\mathbf{1}\uparrow\rangle \tag{2.41}$$
$$\eta_2 = 4i\langle x\mathbf{R}\uparrow|H_{SO}|y\mathbf{R}+\tau_\mathbf{1}\uparrow\rangle \tag{2.42}$$
$$\eta_3 = 4i\langle x\mathbf{R}\uparrow|H_{SO}|z\mathbf{R}+\tau_\mathbf{1}\uparrow\rangle \tag{2.43}$$
$$\eta_4 = 4i\langle z\mathbf{R}\uparrow|H_{SO}|x\mathbf{R}+\tau_\mathbf{1}\uparrow\rangle. \tag{2.44}$$

with the tetrahedron vector $\tau_\mathbf{1} = \frac{a_0}{4}(111)$, and a_0 as the bulk lattice constant. For the diamond structure, the symmetry constraint $\eta_1 = 0$, and $\eta_3 = -\eta_4$ has to be considered [108].

An *ab-initio* bulk band structure obtained within a HSE06 hybrid functional calculation including SOC is used as benchmark for the fit of the TB parameters. More precisely, 14 of its eigenvalues at the high-symmetry points, five at Γ, three at X, and six at L are used to fit the first-nearest neighbor parameters. During the iterative fitting procedure, the set of matrix elements was modified via a simplex algorithm in order to minimize the deviations of the chosen set of band structure parameters from the reference values computed within the HSE06 functional. The resulting TB matrix elements are listed in Tab. 2.1. As we are interested in strained systems, a d^{-2} scaling of the nearest-neighbor empirical TB parameters with d as the distance between adjacent neighbors [111]. For the description of the hydrogen passivation of the α-Sn(001) surfaces, we use a basis of one hydrogen s orbital and the Sn sp^3s^* hybrid orbitals but neglect ss^* interactions [30].

Parameter	This work	Ref. [30]
E_s	-7.5802	-7.2029
E_p	0.0081	0.0032
E_{s^*}	23.6535	14.1081
$V_{ss\sigma}$	-1.4495	-1.4802
$V_{s^*s^*\sigma}$	-2.0966	0.4795
$V_{sp\sigma}$	1.8612	1.9034
$V_{s^*p\sigma}$	3.5269	2.7564
$V_{pp\sigma}$	2.4642	3.3555
$V_{pp\pi}$	-0.6816	1.6848
Δ_{so}	0.8242	0.64
η_1	0.0000	-
η_2	0.0556	-
η_3	-0.0204	-
η_4	0.0204	-

Table 2.1: First-nearest-neighbor TB parameters for α-Sn in an orthogonal sp^3s^* model including spin-orbit interaction with a splitting Δ_{SO} eV of the p states at Γ. The values are given in the notation of Slater and Koster [94] compared to those of published in Ref. [30]. In addition five intra- and interatomic spin-orbit coupling matrix element are given. All values are in eV. The deviations are mainly a consequence of the inclusion of three-center integrals but the neglect of SOC in Ref. [30].

3 Results

3.1 Bulk materials

For the understanding of the behavior of nanostructures, it is crucial to study the properties of the bulk materials, of which they consist. Therefore, in the present section, the electronic properties of α-Sn, HgTe, CdTe, and InSb are studied in detail. Comparing band structures obtained within the MBJLDA to hybrid functional calculations (see Sec. 2.2.3.3), and experimental results, it is conclusively shown, that the MBJLDA is sufficiently accurate, which allows to apply it to the low dimensional systems studied later on. In the case of α-Sn, the optical absorption and emission characteristics are additionally investigated, because they will be compared to those of α-Sn nanocrystals in the next section. The influence of biaxial strain on bulk α-Sn and HgTe is discussed to understand, how the growth of these materials on the slightly lattice mismatched substrates influences their electronic structure. In addition, a tight-binding band structure of α-Sn is presented to underline the reliability of this approximation, which will later be used to describe thick α-Sn films, in comparison to hybrid functional calculations.

3.1.1 Zero-gap materials with inverted band ordering: α-Sn and HgTe

The band structures of α-Sn and HgTe obtained within HSE06 hybrid functional calculations including spin-orbit interaction are depicted in Fig. 3.1 and compared to the MBJLDA results. Both materials are zero-gap semiconductors, as the four-fold degenerated Γ_{8v} is energetically equivalent with the Fermi energy. In addition, due to the strong relativistic mass-Darwin effect, the s-like Γ_{6c} level is located in-between the two spin-orbit split-off Γ_{8v} and Γ_{7v} levels. This allows for the definition of a "negative" fundamental energy gap $E_g = \epsilon(\Gamma_{6c}) - \epsilon(\Gamma_{8v})$. The MBJLDA band structures give the same band ordering around the Γ point as the HSE06 result for both materials. These findings are in qualitative agreement with various experimental and theoretical findings [1, 2, 23, 112–120].

The fundamental energy differences and spin-orbit splittings at Γ within different approximations are summarized in Table 3.1 and Table 3.2, respectively. We find the hybid functional results to be in good agreement with the MBJLDA values. The fundamental energy gaps computed amount to $E_g^{\mathrm{HSE}} = -0.52$ eV ($E_g^{\mathrm{MBJ}} = -0.23$

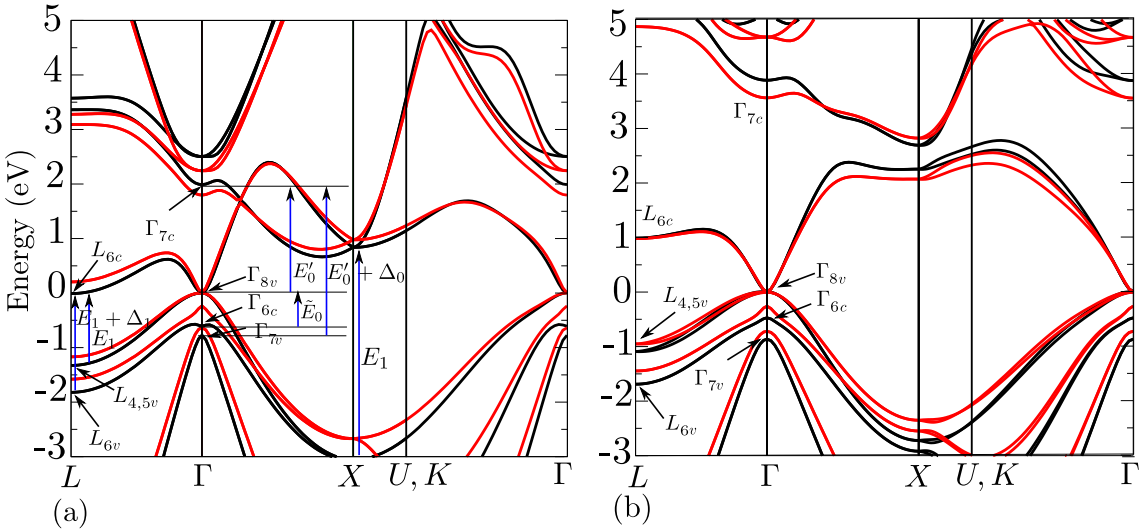

Figure 3.1: Band structures of α-Sn (a) and HgTe (b). The results of hybrid-functional (HSE06) calculations (black lines) are compared to MBJLDA calculations (red line). The irreducible representations of the band states together with their degeneracy is indicated. The Γ_{8v} level is chosen as energy zero. In the case of α-Sn, the optical transitions at the high-symmetry points L, Γ, and X are indicated by blue arrows.

eV) for α-Sn and $E_g^{\mathrm{HSE}} = -0.0.48$ eV($E_g^{\mathrm{MBJ}} = -0.26$ eV) for HgTe, respectively. These values are in reasonable agreement with measured values of $E_g = -0.29$ eV [115] ($E_g = -0.41$ eV [121]) and a result from self-consistent GW quasiparticle calculations using a band structure based on hybrid functionals as starting point, of $E_g = -0.18$ eV [120] for HgTe. On the other hand, non-self-consistent GW calculations starting from a DFT-LDA band structure performed by Sakuma et al. [119] give a value of $E_g = -0.6$, which is by a factor 2 larger than the experimental one. There is a suggestion, that the inclusion of vertex corrections in the GW quasiparticle calculations [122] reduces the difference from the experimental value by 0.1-0.2 eV. The GW quasiparticle result based on a starting electronic structure using the HSE hybrid functional [28] of $E_g = -0.20$ eV for α-Sn [123] is also close to the MBJLDA and experimental values. The spin-orbit splittings at Γ, $\Delta_0 = \varepsilon(\Gamma_{8v}) - \varepsilon(\Gamma_{7v})$, computed within MBJLDA are 0.73 eV (HgTe) and 0.64 eV (α-Sn), which is close to the HSE results of 0.87 eV (HgTe) and 0.68 eV (α-Sn). For HgTe, the spin-orbit-induced valence band splitting within MBJLDA at Γ only differs by approximately 200 meV from the measured value [115] and GW calculations [119]. The computed spin-orbit splitting in α-Sn is in excellent agreement with an experimental value of 0.8 eV [121] and close to the GW result of 0.66 eV [123].

We have to point out, that the order of Γ_{6c} and Γ_{7v} is interchanged within all local and semilocal treatments of XC such as LDA, GGA, and LDA+U. Moreover, these

Material	HSE06	MBJLDA	LDA	exp.
α-Sn	-0.519	-0.229	-0.694	-0.413 [121]
HgTe	-0.476	-0.261	-0.840	-0.29 [115]
				-0.28 [116]
CdTe	1.122	1.547	0.297	1.57 [124]
				1.529 [125]
				1.49 [117]
InSb	0.050	0.311	0.000	0.235 [126]
				0.230 [127]

Table 3.1: Fundamental energy gap of bulk α-Sn, HgTe, CdTe, and InSb within HSE06, LDA, and MBJLDA and their comparison with experimental data. All values in eV.

Material	HSE06	MBJLDA	LDA	exp.
α-Sn	0.680	0.639	0.386	0.8 [121]
HgTe	0.867	0.731	0.789	0.91 [115]
				1.08 [116]
CdTe	0.915	0.810	0.869	0.92 [117]
				0.95 [94]
InSb	0.757	0.740	0.771	0.83 [117]
				0.85 [128]

Table 3.2: $\Gamma_{8v} - \Gamma_{7v}$ spin-orbit splittings of bulk α-Sn, HgTe, CdTe, and InSb within HSE06, LDA, and MBJLDA and their comparison with experimental data. All values in eV.

XC functionals result in negative $\Gamma - L$ gaps and, hence, metallic band structures in the case of α-Sn. This problem can be overcome by adding a fraction of short-range nonlocal Fock exchange within the HSE06 functional or by modeling exact exchange within the MBJLDA method. Within both methods, the L_6 level is energetically above the Γ_{8v} one.

It can be concluded, that the MBJLDA is the only method, that combines reasonable electronic structure results concerning level ordering, band dispersion, and energetic distances with a computational effort, which can be sustained for large systems such as heterostructures modeled by supercells containing more than 100 atoms.

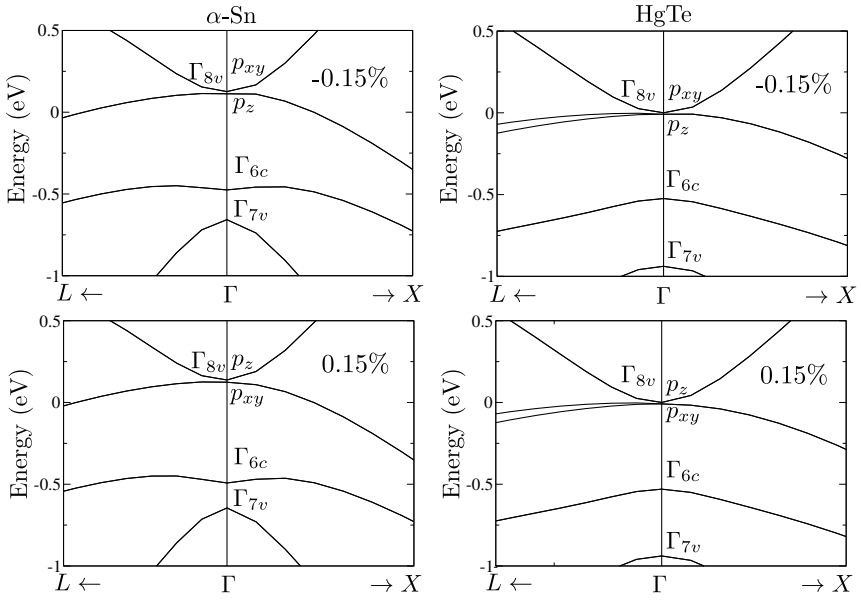

Figure 3.2: Band structures of biaxially strained α-Sn (left panels) and HgTe (right panels) for -0.15% (compressive), and 0.15% (tensile) strain. The Fermi level is chosen as energy zero and only the most important bands in the vicinity of Γ are presented. The level symmetries as well as the orbital momentum character are indicated. Despite the tetragonal symmetry of the strained crystals, the zinc-blende notation is kept.

3.1.2 Influence of small biaxial strain on the electronic structure of α-Sn and HgTe

One of the main topics of the present work is the investigation of electronic properties of α-Sn and HgTe quantum well structures. As described above, CdTe and InSb are nearly lattice-matched materials with the same tetrahedral lattice symmetry and, therefore, the most suitable substrates for the growth of the two zero gap semiconductors. However, due to the small differences in the lattice constants, the confined materials HgTe and α-Sn are biaxially strained when grown on these substrates.

The influence of 0.15% biaxial compressive and tensile strain on the band structures of α-Sn and HgTe is depicted in Fig. 3.2. The main effects of the strain with respect to the electronic structure are the same for both materials, α-Sn and HgTe. Due to the strain-induced symmetry-lowering, the fourfold degeneracy of the Γ_{8v} level is lifted. It is split into two sets of even-parity Kramers doublets, independent of the sign of the biaxial strain. As it is indicated in Fig. 3.2, the sign of the strain only determines the ordering of the p_z and the p_{xy}-like Γ_{8v} doublets. In the case of compressive (tensile) strain, the upper bands are p_{xy} (p_z)-like, while the lower ones, which remain occupied, possess p_z (p_{xy}) character. Correspondingly, the gap

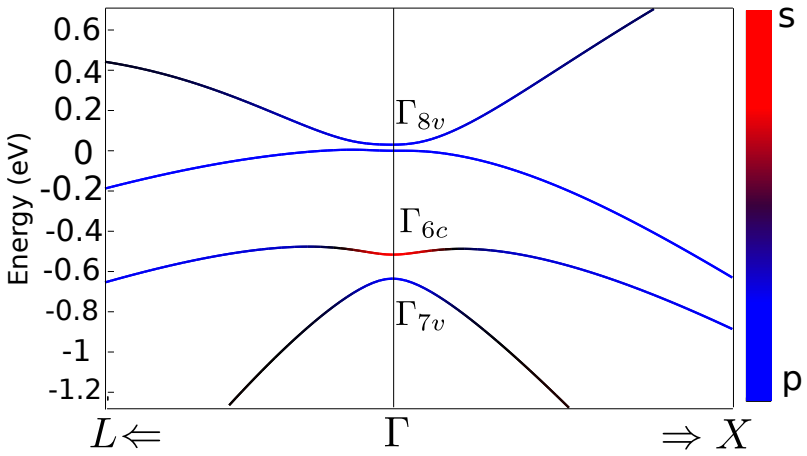

Figure 3.3: Tight-binding band structure of 0.15% compressively strained α-Sn. The projections of the band states on atomic s and p orbitals is indicated by colors.

opening may be characterized by $E_g^{\text{strain}} = \Xi_b \epsilon_b$ with a biaxial deformation potential $\Xi_b = 9.3eV$ ($\Xi_b = 6eV$) measured for the biaxial strain $\epsilon_b = \pm 0.0015$ in the case of α-Sn (HgTe). According to the definition of a topological insulator, a small fundamental band gap in the bulk material [3, 129] is necessary for the occurrence of metallic surface or edge states. Indeed, the strain-induced gap in combination with the strong SOC suggests to study the topological properties of α-Sn and HgTe.

For α-Sn as well as in the case of HgTe, the level ordering $\Gamma_{7v} < \Gamma_{6c} < \Gamma_{8v}$ remains unchanged and the absolute positions of the Γ_{7v} and Γ_{6c} levels are only slightly shifted in energy with respect to the unstrained materials for both, tensile and compressive strain.

3.1.3 Tight-binding results: strained α-Sn

Because of the fitting procedure described in Sec. 2.6 the characteristic energy differences of the HSE band structure are reproduced in the unstrained case. The Slater-Koster representation for the nearest-neighbor interaction and the d^{-2} scaling law, however, also allow for the study of strained α-Sn. The TB band structure of 0.15% compressively strained α-Sn is depicted in Fig. 3.3. The behavior found in Fig. 3.2 is reproduced. This concerns the band ordering (i) $\Gamma_{7v} < \Gamma_{6c} < \Gamma_{8v}$, (ii) the band splittings E_0 and Δ_{SO} at Γ, (iii) the camel-back or Mexican-hat shape of the Γ_{6c} band, and (iv) the splitting of the Γ_{8v} states into p_z-like and p_{xy}-like bands. The band gap opening due to the biaxial strain ϵ is rather similar. The biaxial deformation potential in TB approximation amounts to $\Xi = 14.3$ eV. That means, that for $\epsilon = \pm 0.0015$ a fundamental gap $\Delta E_g^{\text{strain}} = 21.5$ meV occurs. Interestingly,

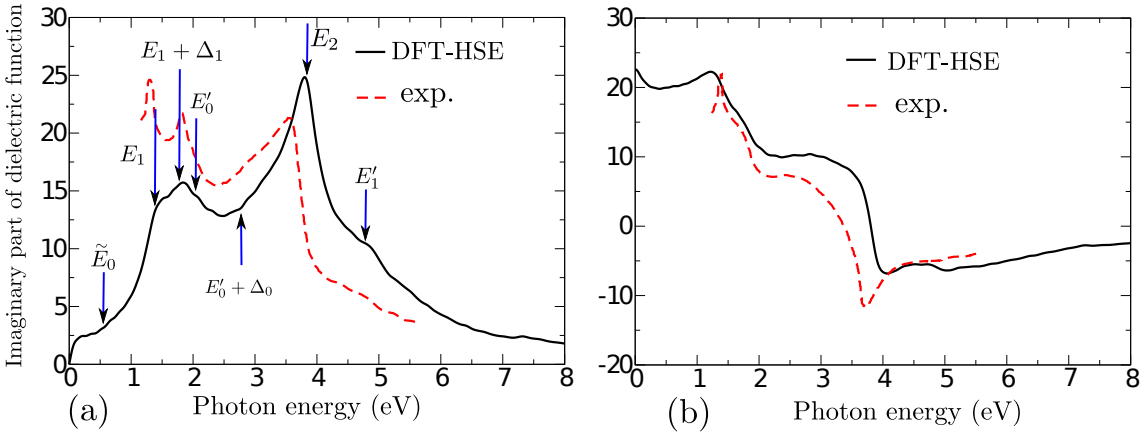

Figure 3.4: Imaginary (a) and real part (b) of the photon energy-dependent dielectric function computed within the independent-particle approximation using the HSE06 hybrid functional compared to experimental results [131]. The energetic positions of the optical transitions in the band structure in Fig. 3.1 are indicated in the imaginary part.

the interatomic spin-orbit-coupling contributions guarantee the correct splittings of the p-derived valence bands. While the Γ_{7v} band does not split for finite wave vectors, Γ_{8v} bands do. This is however not visible in Fig. 3.3 due to the small range around Γ, that is plotted to clearly depict the strain-induced gap. In agreement with the irreducible representations of the small point group of the wave vector within the double group notation for the true diamond symmetry [110, 130] the level Γ_{8v} splits into Δ_6 and Δ_7 (along the Δ line ΓX), Λ_4, Λ_5, and Λ_6 (along the Λ line ΓL), and Σ_5 and Σ_5 (along the Σ line ΓK), respectively.

3.1.4 Optical properties of α-Sn

The imaginary and real part of the photon energy dependent dielectric function computed within the independent-(quasi)particle approximation (see Sec. 2.4) using the HSE06 hybrid functional are displayed in Fig. 3.4 and compared to experimental results obtained by spectral ellipsometry [131]. The imaginary part of the dielectric function in Fig. 3.4(a) possesses no absorption edge in accordance with the zero-gap of the bulk band structure described in Sec. 3.1.1. The first peak-like structure appears in an energy range between 1.5 and 2 eV and is related to the energies of the E_0', $E_0' + \Delta_0$, and the E_1', $E_1' + \Delta_1$ transitions, which are indicated in Fig. 3.1. The maximum of this first structure is close the $E_0' + \Delta_0$ interband transition, which underlines the importance of the inclusion of spin-orbit interaction in the calculations. The second peak is much sharper than the first one and appears between 3.5 and 4 eV with its maximum about 150 meV lower in energy than the

E_2 transition. This disposition is likely to be caused by other transitions, that are energetically close to the E_2 transition, which may distort the E_2 peak and shift its maximum to the present position.

The results are in qualitative agreement with the ellipsometry measurements of Höchst et al. [131] concerning the line shape and peak positions. The absorption maxima caused by the E_1 and $E_1 + \Delta_1$ transitions near the L point at 1.35 eV and 1.80 eV are in close agreement to the ellipsometry results. The theoretical E_2 peak near 3.7 eV appears to be a blue shifted by about 250 meV with respect to the measured one. Deviations between the calculated and the measured results are found concerning the peak heights. The measured heights of the low-energy peaks related to the E_1 and $E_1 + \Delta_1$ are about 30% higher than our HSE06 results, while the measured intensity of the E_2 peak is about 20% lower. As the attractive electron-hole interaction generally leads to a redshift of the higher interband transitions and a redistribution of spectral strength from higher to lower energies [31, 132–134], the differences in peak heights and positions are likely to be caused by the neglected excitonic effects in our calculations.

The real part of the dielectric function and the comparison with measured values is shown in Fig. 3.4(b). The value for vanishing photon energy equals the dielectric constant $\epsilon_\infty = \mathrm{Re}\epsilon(0) = 22.6$, which is in close agreement with the experimental value $\epsilon_\infty = 22.6$ [111]. The real part of the dielectric function becomes negative for photon energies above 3.8 eV, which is close to the E_2 energy. The line shape is similar to that measured by Höchst et al. [131] despite slightly shifted peak positions. The lowest measured peak at about 1.4 eV is blue-shifted by about 150 meV compared to the theoretical value, while the measured minimum of the real part of the dielectric function near the E_2 energy is shifted by 300 meV toward lower energies with respect to the calculated one. Both peaks within the measured function appear to be much sharper than the calculated ones. It can be summarized, that the independent-(quasi)particle approximation seems to give reasonable results for the optical properties of bulk α-Sn and, consequently, should be applicable to study the effects of electronic confinement in α-Sn NCs.

3.1.5 Conventional tetrahedrally coordinated semiconductors: CdTe and InSb

The band structures of CdTe and InSb are depicted in Fig. 3.5, and the results of hybrid-functional calculations within the HSE06 approach are compared to MBJLDA-derived results. The atomic orbital symmetry of the bands is indicated as well. Both materials are direct semiconductors with an s-type Γ_{6c} conduction

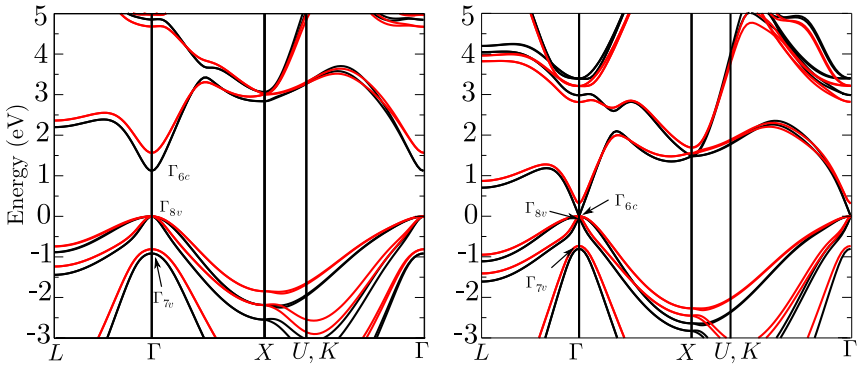

Figure 3.5: Band structures of CdTe (a) and InSb (b). The results of hybrid-functional (HSE06) calculations (black lines) are compared to MBJLDA calculations (red line). The irreducible representations of the band states together with their degeneracy is indicated. The Γ_{8v} level is chosen as energy zero.

band edge at Γ. The valence band edge is formed by the p-type Γ_{8v} level the in both cases. Below the Γ_{8v} valence band, the spin-orbit split-off Γ_{7v} level is located. The characteristic energies obtained within different approximations are also summarized in Tab. 3.1 and Tab. 3.2.

The fundamental energy gaps $E_g = \epsilon(\Gamma_{6c}) - \epsilon(\Gamma_{8v})$ of CdTe are given by 1.122 eV (HSE06) and 1.547 eV (MBJLDA). The value calculated within MBJLDA is in very good agreement with room-temperature measured values of 1.529 eV as well as low-temperature measured gaps of 1.57 eV [124, 125].

In the case of InSb, the LDA gives a wrong band degeneracy at Γ, as the four fold degeneracy of the Γ_{8v} valence level is lifted. Moreover, the fundamental gap is closed. Despite the fact, that the HSE06 approach gives the right band degeneracy, the fundamental band gap $E_g^{HSE} = 50$ meV is still significantly underestimated within HSE06 compared to the experimental values of about 230 meV (see Table 3.1). Using the MBJLDA, a fundamental gap of 310 meV is obtained, which is much closer to the experimental value. This result is in excellent agreement with the LDA-$\frac{1}{2}$, which is another approximate QP approach [135] and gives a value of $E_g = 0.23$ eV [136].

The spin-orbit splittings within HSE06 between the Γ_{8v} and the Γ_{7v} level amount $\Delta_{SO}^{HSE} = 0.92$ eV in the case of CdTe and 0.76 eV for InSb. The MBJLDA values $\Delta_{SO}^{MBJ} = 0.81$ (CdTe) and $\Delta_{SO}^{MBJ} = 0.74$ (InSb) are also in reasonable agreement with experimental findings.

In summary, the band structure calculations show, that the MBJLDA yields reasonable results in good agreement with both, experimental findings and HSE06 hybrid functional calculations and can therefore be used for the treatment of het-

erostructures containing of InSb, CdTe, α-Sn, and HgTe.

3.2 Topological properties of the bulk band structures

3.2.1 Topological invariants

The topology of the ground-state band structure of an insulating bulk system can be characterized by $\mathbb{Z}_2$ topological invariants [3, 4, 137, 138]. There are four $\mathbb{Z}_2 = (\nu_0; \nu_1, \nu_2, \nu_3)$ invariants that allow to distinguish three categories of materials: ordinary insulators, strong TIs, and weak TIs in three dimensions. The strong TIs are characterized by $\nu_0 = 1$ allowing for the existence of spin-polarized surface- or edge states and, hence, the QSH phase [3, 6, 10, 138]. The QSH phase is characterized by these chiral edge states giving rise to intrinsic spin currents without external magnetic fields which are quantized to $2e^2/h$. These states are robust in the presence of weak disorder of the system and therefore topologically protected and, hence, ν_0 is called the strong $\mathbb{Z}_2$ invariant, because it distinguishes the strong TIs from the weak TIs. The weak TIs refer to $\nu_0 = 0$, while some or all of the ν_k, $k \in \{1, 2, 3\}$, equal one. However, topologically non-trivial ν_k also give rise to chiral edge states but they depend on the choice of the lattice vectors and are not preserved in the presence of weak disorder [3, 6]. The weak $\mathbb{Z}_2$ numbers are nonetheless important, when clean surfaces are studied. In the case of normal insulators, all four $\mathbb{Z}_2$ invariants are zero, and no chiral edge states occur. In two dimensional systems such as germanene, there is only one $\mathbb{Z}_2$ invariant, which distinguishes normal insulators and topological insulators [3, 138].

For systems with inversion symmetry, the four invariants can be determined from the parity of the occupied Bloch wave functions at the time-reversal invariant momenta (TRIM) points of the Brillouin zone [3]. These momenta are special $\mathbf{k}$ points Γ_i, that satisfy the condition $-\Gamma_i = \Gamma_i + \mathbf{G}$ for a reciprocal lattice vector $\mathbf{G}$. There are eight (four) TRIM points in three (two)-dimensional systems [3]. The parities of the occupied, twofold Kramers-degenerate TRIM pairs determine the topological invariants. The parities can be calculated as expectation values of the parity operator [3, 138]. However, the evaluation of the matrix elements of the parity operator requires inversion symmetry, which is not present in HgTe. In both materials, the strain is necessary to lift the fourfold degeneracy of the Γ_{8v} states to obtain an insulating ground state, and, hence, the symmetry labels of the unstrained lattice symmetry do in principle not apply for the resulting tetragonal structures. Nonetheless, the $\mathbb{Z}_2$ class of strained HgTe and α-Sn have been determined applying the symmetry labels of the ideal diamond-lattice symmetry with inversion symmetry based on

arguments of adiabatic continuity [3].

Another possibility proposed by Fu and Kane [3, 137] is the determination of the $\mathbb{Z}_2$ invariants from the Pfaffian of the matrix elements of the time-reversal operator using the occupied band states at TRIM points as basis set. Despite the resulting $\mathbb{Z}_2$ invariants calculated by means of the Pfaffian matrix method are gauge independent, the method itself depends on a gauge transformation [3, 137]. However, using *ab-initio* methods, the electronic wave functions of different band states and at different **k**-points do not have a fixed phase relation to each other but random phase factors. This makes a gauge fixing of the wave functions obtained from *ab-initio* calculations non-trivial [139–142].

Both methods to evaluate the topological class from the parities of the occupied bands as well as the Pfaffian matrix method are consequently not appropriate to calculate the $\mathbb{Z}_2$ class of materials lacking inversion symmetry and using *ab-initio* methods.

3.2.2 Numerical approach to $\mathbb{Z}_2$ invariants

In 2011, Yu et al. [139] proposed an expression of the $\mathbb{Z}_2$ invariant for insulating bulk band structures using the non-Abelian Berry connection. This method does not require any gauge-fixing of the wave functions nor inversion symmetry and and can therefore be directly applied to *ab-initio* calculated wave functions. To evaluate the topological character of the materials considered in this thesis, this method was implemented in the VASP code in cooperation with Lars Matthes.

According to the Fu-Kane theory, the number of the Kramers pair switchings modulo 2 along a line connecting two time-reversal invariant momenta is equivalent to the topological invariant of the system [3, 138]. Time-reversal symmetry requires twofold degeneracy of the band states at both TRIM points (Kramers pairs). However, along the path connecting these TRIM points, the degeneracy is lifted and Kramers-pair switchings may take place. An odd number of Kramers pair switchings is directly related to an odd number of crossings between the respective surface state and the Fermi energy and, consequently, the existence of spin-polarized surface states, which is identical to the QSH phase. This topic is discussed in detail elsewhere [3, 6, 137]. Yu et al. [139] showed, that in the two-dimensional case, the Kramers pair switching is equivalent to the "partner switchings" of the Wannier function centers (WCC) during a closed loop in the Brillouin zone.

The starting point for the actual calculation is, that the evolution of the Wannier charge centers can be related to the phase of the eigenvalues of the position operator $\mathbf{X}$ projected onto the occupied band states. This eigenvalue problem of the position

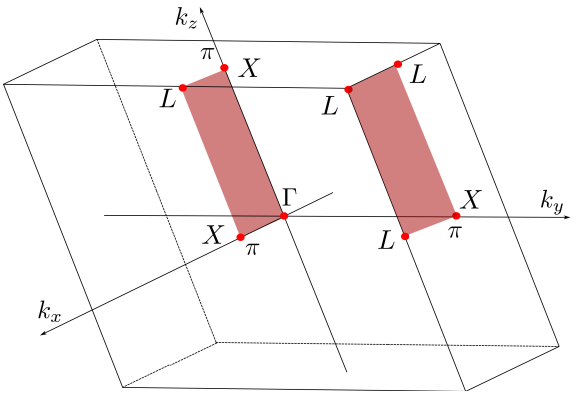

Figure 3.6: Visualization of the two-dimensional subsystems, that are used for the computation of the topological invariants. The reciprocal lattice vectors $\mathbf{b}_i$ $(i = 1, 2, 3)$ of a fcc Bravais lattice are indicated together with the planes defined by $k_j = 0$ and $k_j = \pi$ $(j = x, y, z)$. The 2D subsystems defined by $k_y = 0$ and $k_y = \pi$ are shaded red exemplarily. TRIM points are depicted as red dots.

operator is then solved by a transfer integral method. In a first step, the calculation of the $\mathbb{Z}_2$ invariant of two dimensional systems is explained. The treatment of three dimensional systems can then be reduced to its two dimensional sub systems. A two-dimensional Brillouin zone spanned by the two reciprocal lattice vectors $\mathbf{b}_x$ and $\mathbf{b}_y$, which are not required to be orthogonal to each other, is considered. The Brillouin zone is discretized in $N_x \times N_y$ intervals with the interval lengths $\Delta k_{x,y} = \frac{2\pi}{N_{x,y} a_0}$, where $\frac{\pi}{a_0}$ is the distance between Γ and the BZ boundary. In order to keep the notation consistent with the literature [139, 142], the values of the k_i are from now on given in units of $\frac{1}{a_0}$. This means, that the k_i run from 0 to π for a full path through the BZ parallel to $\mathbf{b}_i$. This procedure is vizualized in Figure 3.6. We calculate the overlap matrices between the Bloch periodic parts $|n, k_x, k_y\rangle$ of the occupied wave functions along lines parallel to $\mathbf{b}_1$ with fixed k_y:

$$(F_{i,i+1}(k_x, k_y))^{m,n} = \langle m, i\Delta_{k_x}, k_y | n, (i+1)\Delta_{k_x}, k_y \rangle. \tag{3.1}$$

Here, n and m denote the band number and run over the $2N$ occupied bands, where the factor two represents the Kramers degeneracy, and $i = 0...N_x$ defines the position in the discretized BZ. Consequently, $F(k_x, k_y)$ is a $2N \times 2N$ matrix. The overlap integral fix the phase between adjacent Bloch states even in the absence of gauge invariance. In a next step, the $2N \times 2N$ matrix $D(k_y)$ is calculated as the matrix product of all $F_{i,i+1}(k_x, k_y)$ along a line parallel to $\mathbf{b}_1$:

$$D(k_y) = F_{0,1} F_{1,2} F_{2,3} \dots F_{N_x-2,N_x-1} F_{N_x-1,0} \tag{3.2}$$

The last multiplication with $F_{N_x-1,0}$ is critical for the purpose of gauge fixing, because it connects the last point of each path parallel to $\mathbf{b}_1$ with the respective starting point yielding a closed loop in $\mathbf{k}$ space. The matrix $D(k_y)$ is diagonalized yielding $m = 1..2N$ complex eigenvalues $\lambda_m(k) = |\lambda_m(k)|e^{i\theta_m(k_y)}$. Their phases $\theta_m(k_y)$ are identified with the position of the Wannier charge centers and invariant under a $U(2N)$ unitary transformation of the occupied band states. Therefore, the arbitrary phase factors resulting from the independent calculation of different wave functions at different $\mathbf{k}$-points within *ab-initio* calculations are eliminated.

The topological invariant of the system is calculated by the number of crossings of an arbitrary horizontal reference line connecting two TRIM points with k_y running from zero to π with the Wannier center evolution curves $\theta_m(k_y)$ mod 2.

For three-dimensional systems it is possible to derive all four $\mathbb{Z}_2$ invariants dividing them in two-dimensional subsystems [139, 140] as depicted in Fig. 3.6. We consider six 2D subsystems in reciprocal space defined by one of the momenta fixed at $k_i = 0$ and $k_i = \pi$ with $i \in \{x, y, z\}$, each containing four TRIM points. In Fig. 3.6, the two 2D subsystems $k_y = 0$ and $k_y = \pi$ are highlighted in red exemplarily. The weak topological indices $\nu_k = (\nu_1, \nu_2, \nu_3)$ are identified with the $\mathbb{Z}_2$ indices of the planes $k_i = \pi$. They obviously depend on the choice of the reciprocal lattice vectors and, hence, are not protected against weak disorder. The strong $\mathbb{Z}_2$ index ν_0 is equivalent to the sum of the $\mathbb{Z}_2$ invariants of two "opposite" $k_i = 0$ and $k_i = \pi$ planes mod 2 for each of the three pairs given by $i = 1, 2, 3$. A strong TI therefore requires, that each pair of 2D subsystems the respective $k_i = 0$ and $k_i = \pi$ planes have different $\mathbb{Z}_2$ invariants. However, there is some redundancy involved in the choice of the actual planes used for the calculation of ν_0 as each of the three pairs in $k = 1, 2, 3$ gives the same result [140]. The strong $\mathbb{Z}_2$ index is therefore obviously independent of the choice of the reciprocal lattice vectors.

3.2.3 Application to bulk crystals

The resulting WCC evolution curves are shown in Figs. 3.7 (slightly biaxially strained α-Sn), and 3.8 (slightly biaxially strained HgTe). In the cases of α-Sn and HgTe it is clearly visible, that all three of the $k_i = 0$ related 2D subsystems exhibit an topologically non-trivial behavior with $\mathbb{Z}_2 = 1$. The reference lines are crossed by an odd number of WCC evolution curves indicating an odd number of Kramers pair switchings. The three opposite faces in the BZ $k_i = \pi$, in contrast, show no crossing or an even number of crossings between the reference line and the WCC evolution curves resulting in $\mathbb{Z}_2 = 0$. It follows, that for each pair of the opposite subsystems $k_i = 0$ and $k_i = \pi$, the $\mathbb{Z}_2$ invariants differ by one. The strong

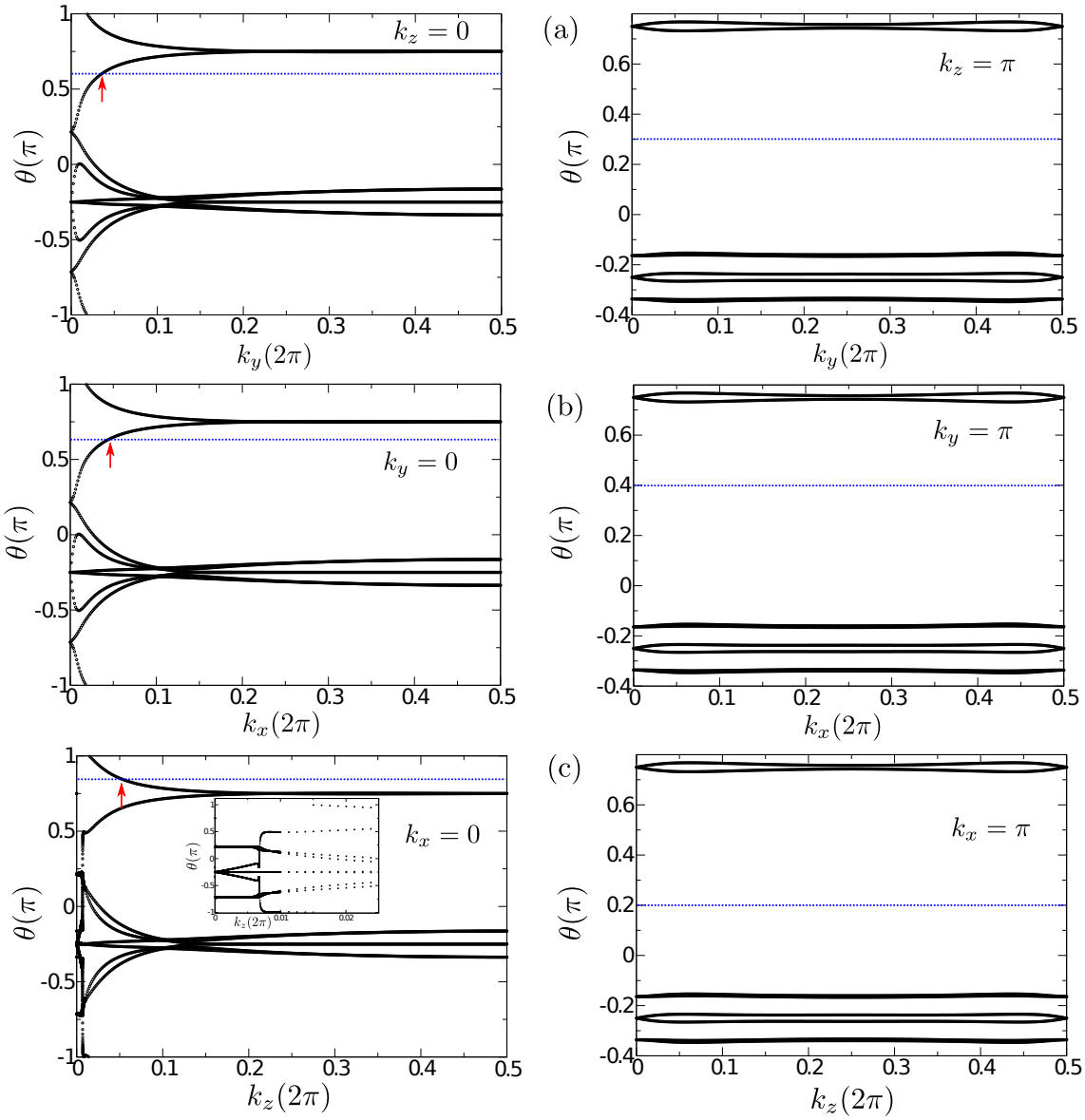

Figure 3.7: WCC evolution curves (black circles) of α-Sn for the six 2D subsystems of the diamond lattice. The reference lines are depicted in blue. Red arrows indicate the crossing points of the WCC curves and the reference line.

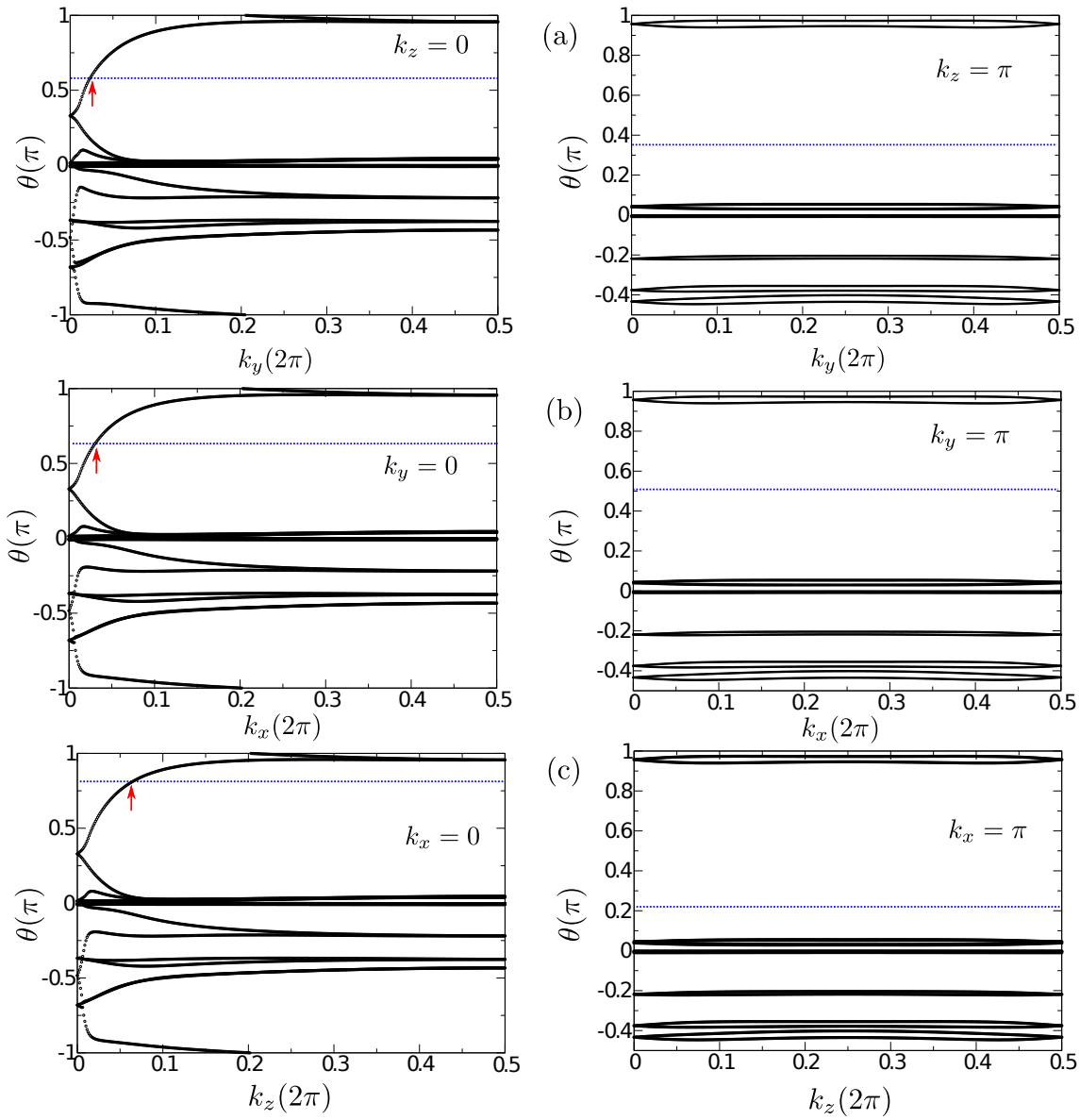

Figure 3.8: WCC evolution curves of HgTe for the six 2D sub systems of the zinc-blende lattice. The reference lines are depicted in blue. Red arrows indicate the crossing points of the WCC curves and the reference lines.

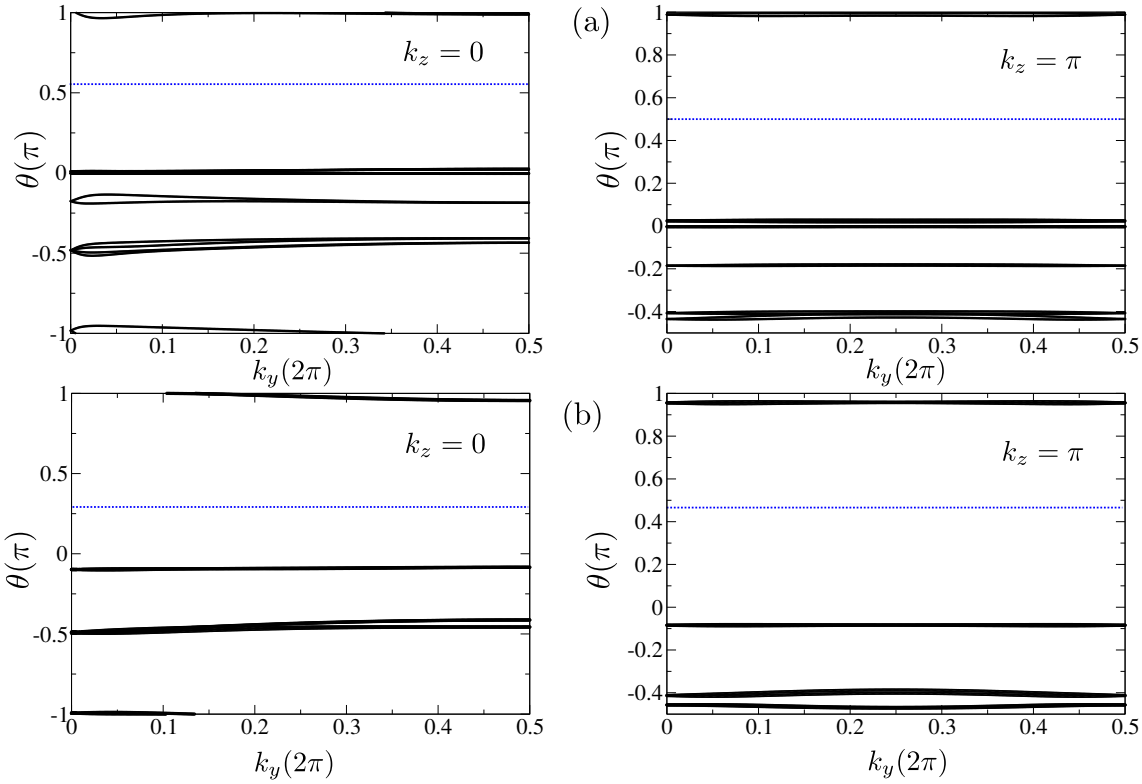

Figure 3.9: WCC evolution curves of CdTe (a) and InSb (b) along k_y for $k_z = 0$ and $k_z = \pi$ of the zincblende lattice. The reference line is depicted in blue. No crossings between the reference line and the WCC evolution curves occur.

$\mathbb{Z}_2$ index of the three-dimensional system ν_0 consequently equals one, identifying both materials as strong topological insulators. The weak topological indices, which are identical with the $\mathbb{Z}_2$ index of the three faces belonging to $k_i = \pi$, equal zero for all $i \in \{x, y, z\}$. The resulting $\mathbb{Z}_2$ class of biaxially strained α-Sn and HgTe is $(1; 0, 0, 0)$, which is in accordance with predictions based on parity evaluation for α-Sn combined with arguments based on adiabatic continuity [3]. For HgTe, a $\mathbb{Z}_2$ analysis using the WCC evolution tracking has been previously done by Yu et al. [139], finding strained HgTe to be a strong topological insulator. However, the weak $\mathbb{Z}_2$ indices have not been derived in the respective work.

Interestingly, test calculations performed with the ideal unstrained structures (see Sec. 2.5) came to the same result, that both, α-Sn as well as HgTe, are strong topological insulators with $\nu_0 = 1$. This is astonishing as it contradicts somehow the original picture of an insulating bulk system [3]. The driving factor for the strong TI character of the both materials might be the band inversion with occupied Γ_{6c} and two empty Γ_{8v} states in contrast to other semiconductors as discussed in Sec. 3.1. The consequences of these findings for the existence of topological surface or edge states in low-dimensional structures of both materials will be studied in detail in the following sections.

The WCC evolution curves along k_y for $k_z = 0$ and $k_z = \pi$ of CdTe and InSb are depicted in Fig. 3.9. The other faces are not shown, because they are topologically equivalent to the latter ones. All 2D subsystems are characterized by a trivial $\mathbb{Z}_2$ index, as the reference lines do not cross the WCC evolution curves. Consequently, CdTe and InSb can be identified as topologically trivial insulators with the $\mathbb{Z}_2$ class $(0; 0, 0, 0)$

3.3 Zero-dimensional systems: α-Sn Nanocrystals

In this section, free-standing α-Sn nanocrystals (see Sec. 2.5.2) are investigated. In a first step, structural issues arising from the nanostructuring and the thermodynamic stability of the NCs is briefly discussed. The main part of the section deals with the electronic structure. It is shown, that the symmetry of the bulk states around the fundamental energy gap is roughly conserved and that in the case of small clusters, the energetic ordering of the band states is interchanged with respect to bulk α-Sn. Because the density of states must converge toward the bulk situation for infinitely large diameter, there has to be a topological transition at a critical diameter, where the level ordering is interchanged. This critical thickness is determined by a fit to *ab-initio* calculations and confirmed within a tight-binding scheme. The reliability

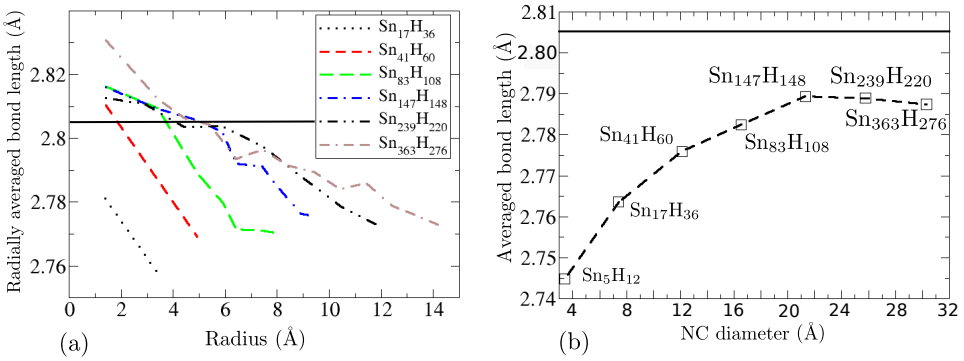

Figure 3.10: Bonding geometry of the α-Sn NCs. (a) Radially averaged bond length versus the distance of the bond midpoint from the NC center and (b) total average of the bond length depending on the NC diameter. The bulk bond length is indicated by the horizontal solid black line.

of the *ab-initio* results is confirmed by ΔSCF calculations of the NC-diameter dependent lowest two-particle excitation energies. Finally, the influences of the electronic structure and its size dependence on the optical absorption and emission properties is discussed.

3.3.1 Geometry

The atomic geometries of the NCs were optimized minimizing the Hellmann-Feynman forces (see Sec. 2.3.1) acting on tin atoms below with the constraint of conservation of the T_d symmetry. The resulting radially averaged Sn-Sn bond lengths depending the distance of the middle of the bond to the NC center are shown in Fig. 3.10(a). The Sn-Sn bond length are maximal near the NC center and decrease toward the surface. In the case of NCs with $N_{\mathrm{Sn}} \geq 41$, the bond length between the atomic shells near the NC center is larger than the bulk value of d =2.804 Å. Due to the distinct decrease of the bond length with increasing distance from the NC center, the bond length becomes even smaller than the bulk value for distances larger than half the NC radius from the NC center. Consequently, tensile strain appears near the NC center while compressive strain acts near the surface. These results are similar to results found for other group-IV NCs [84, 87, 96, 143]. The compressive strain near the surface can be explained by surface stress effects, which have been described for spherical drops [144]. The tensile strain near the NC center might be a consequence of additional degrees of freedom compared to the bulk situation.

The total average of all Sn-Sn bond length depending on the NC diameter is displayed in Fig. 3.10(b) for all NCs. As the majority of the bonds are located near

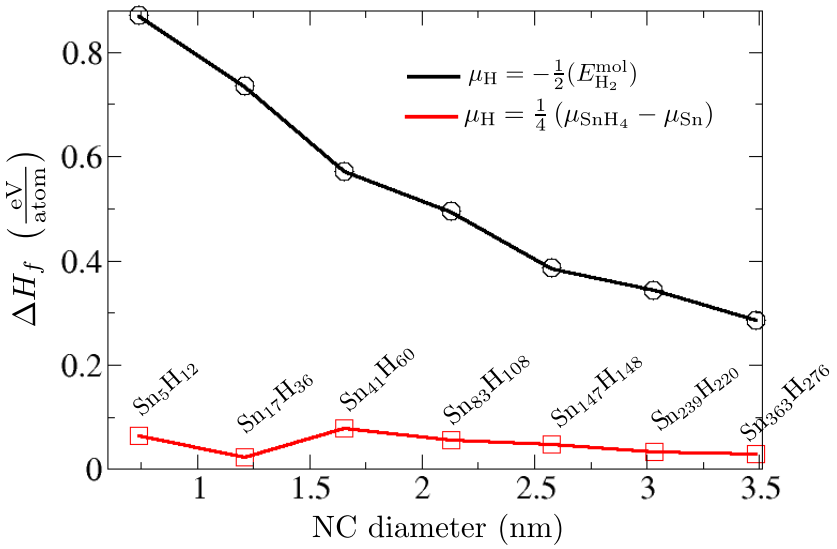

Figure 3.11: Enthalpy of formation for tin-rich conditions depending on the NC diameter for two choices of the hydrogen reservoir.

the surface, where the material is compressively strained with respect to the bulk material, the tensile strain near the NC center is overcompensated so that the total average bond length is smaller than the bulk value for all NCs studied. For large NC diameter, the average bond length has to converge toward the bulk value, which is clearly visible in Fig. 3.10(b) as well. The slight decrease of the average bond length for the two largest NCs $Sn_{239}H_{220}$ and $Sn_{363}H_{276}$ is very likely related to the lower breaking criterion for the atomic forces during the geometrical relaxation due to the computational effort (see Sec. 2.3.1).

3.3.2 Enthalpy of formation

The question of thermodynamic stability of the NCs can be discussed in terms of the enthalpy of formation ΔH_f as difference between the total ground state energy $E_{NC}(N_{Sn}, N_H)$ calculated within DFT and the chemical potentials μ_{Sn} and μ_H of the particle reservoirs per atom

$$\Delta H_f = E_{NC}(N_{Sn}, N_H) - N_{Sn}\mu_{Sn} - N_H\mu_H. \tag{3.3}$$

The choice of the chemical potentials allows for the simulation of a wide range of growth conditions. The enthalpy of formation is calculated depending on the difference $\Delta\mu_{Sn} = \mu_{Sn} - \mu_{Sn}^{bulk}$ between the chemical potential of tin μ_{Sn} and the

bulk value $\mu_{\mathrm{Sn}}^{\mathrm{bulk}} = -E_{\mathrm{bulk}}^{\alpha-\mathrm{Sn}}$, which is assumed to be equal to the DFT ground state energy of bulk α-Sn per atom. Allowing for a variation of $-\infty < \Delta\mu_{\mathrm{Sn}} \leq 0$, the upper bound simulates Sn-rich conditions where bulk α-Sn acts as reservoir, whereas lower values simulate Sn-poor conditions. From equation (3.3) it is obvious, that the enthalpy of formation depends linearly on the chemical potential of tin and becomes minimal for tin-rich conditions $\mu_{\mathrm{Sn}} = \mu_{\mathrm{Sn}}^{\mathrm{bulk}}$. Therefore, tin-rich conditions are favorable for the preparation of the NCs.

The results for the enthalpy of formation depending on the NC diameter are displayed in Fig. 3.11. Two different growth conditions concerning the hydrogen reservoir are modeled. First, the molecular hydrogen is simulated setting $\mu_{\mathrm{H}} = \frac{1}{2}\mu_{\mathrm{H_2}} = -\frac{1}{2}E_{\mathrm{mol}}^{\mathrm{H_2}}$ with $E_{\mathrm{mol}}^{\mathrm{H_2}} = 6.7$ eV being the total DFT-LDA (see Sec. 2.2.3.2) ground state energy of a H_2 molecule. The second possible scenario is the usage of SnH_4 molecules as hydrogen reservoir. This can be modeled setting $\mu_{\mathrm{H}} = \frac{1}{4}[E_{\mathrm{SnH_4}} - \mu_{\mathrm{Sn}}]$ with the binding energy $E_{\mathrm{SnH_4}} = 16.53$ eV of an SnH_4 molecule. Using molecular hydrogen as reservoir, the enthalpy of formation converges toward zero for large nanocrystals indicating that large NCs are energetically favored compared to small clusters (black line in Fig. 3.11. Therefore, if diffusion of Sn atoms is possible, tin atoms might diffuse from small NCs which, hence, become even smaller and eventually vanish, to larger NCs. This process is called Ostwald ripening [145]. However, the enthalpy of formation is significantly lower and its dependence on the NC diameter nearly vanishes, if SnH_4 molecules are used as hydrogen reservoir (red line in Fig. 3.11). It can be concluded, that the enthalpy of formation strongly depends on the growth conditions and that the formation with a gas of SnH_4 molecules is energetically favorable.

3.3.3 Electronic Structure: Size-dependent level symmetry and topological transition

Due to the huge real-space unit cells, the Brillouin zones are very small. Consequently, the eigenvalues become discrete and no **k**- dispersion occurs. Hence, only the Γ-point is needed to characterize the NC energy levels. As an example, Fig. 3.13 displays the eigenvalue spectrum of the $Sn_{17}H_{36}$ nanocrystal in DFT-LDA approach as well as the corresponding angular-momentum projected density of states. The density of states shows that the highest occupied levels are mainly formed by atomic Sn $4p$ states, whereas atomic $5s$ states yield the main contributions to the lowest unoccupied eigenstates. This is remarkable, because it implies that the ordering of s- and p- derived states is inverted with respect to the bulk situation. The influence of Sn $3d$ states has been found to be negligible in the energetic vicinity of the

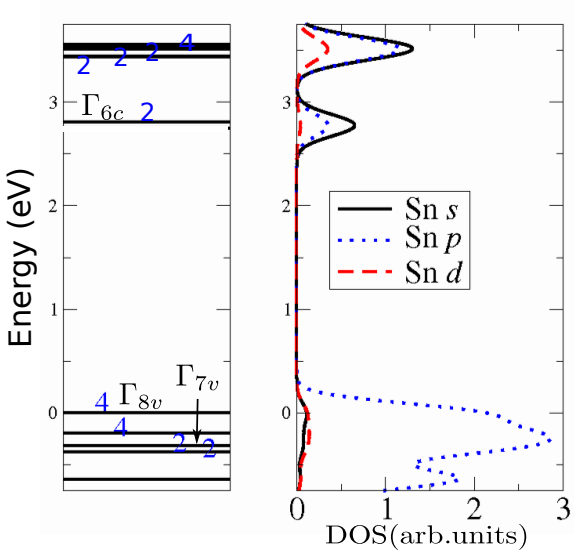

Figure 3.12: Energy eigenvalues and angular-momentum-resolved density of states of the $Sn_{17}H_{36}$ nanocrystal in the energy range of the fundamental gap. The bulk-derived symmetry of the corresponding wave functions are labeled. The level degeneracy is marked by numbers 2 and 4.

fundamental gap. The same holds for the contributions of the passivating hydrogen atoms.

However, the projection on spherical harmonics is not sufficient for the identification of the level symmetry [146, 147]. Assuming that due to the T_d symmetry of the nanocrystals, the NC wave functions are symmetry-equivalent to bulk eigenstates, we calculate the overlap between the bulk Bloch states $\phi_\alpha^{\mathbf{k}j}(\mathbf{x})$ and the nanocrystal eigenstates $\psi_\beta^n(\mathbf{x})$ to determine the probability to find the symmetry of a bulk wave function in a NC eigenstate [146, 148]. Because the edge lengths of the NCs are multiples of the bulk lattice constant, it is possible to use them as non-primitive unit cells for α-Sn bulk, if they are totally filled with Sn atoms. The high-symmetry eigenstates Γ_{8v}, Γ_{7v}, and Γ_{6c} of this bulk system can then be identified by their eigenvalue, because the spacial average of the electrostatic potential, which defines the energy zero in each calculation, is the same for both, the primitive and the non-primitive bulk unit cell. Consequently, the wave function overlap between the bulk state and the NC state can be expressed as

$$P(n,m,\mathbf{k}) = \sum_{i=n}^{n+d_{NC}} \sum_{j=m}^{m+d_B} \left| \sum_{\alpha\beta} \int \mathrm{d}^3\mathbf{x} \psi_\alpha^i(\mathbf{x}) (\phi_\beta^{j\mathbf{k}}(\mathbf{x}))^* \right|^2 . \tag{3.4}$$

Here, n and m indicate the corresponding eigenvalues, and d_B (d_{NC}) denotes the degeneracy of the bulk (NC) state. Equation (3.4) has been evaluated for the

HOMO, LUMO and energetic close states of the nanocrystals and the Γ_{8v}, Γ_{7v}, Γ_{7c}, and Γ_{6c} states of bulk α-Sn at $\mathbf{k} = \Gamma$. There are only three combinations around the fundamental energy gap of the NC of bulk- and NC wave functions with an overlap close to one. All other combinations lead to a vanishing overlap and obviously no hybridization or multi-bulk band coupling occurs. We obtained the same result applying this projection technique within the tight-binding method. This is in accordance to what has been reported by Luo et al. using a similar projection technique in the case of colloidal InAs, InP, CdSe, and Si NCs [146]. Therefore, we can clearly identify the bulk- symmetry of three NC states that are also indicated in Fig. 3.12:

- LUMO $\leftrightarrow \Gamma_{6c}$
- HOMO $\leftrightarrow \Gamma_{8c}$
- HOMO-2 $\leftrightarrow \Gamma_{7c}$

The degeneracy of the states is also in agreement with that of the respective bulk states and is a consequence of the spin orbit splitting. Astonishingly, the energetic level ordering is indeed inverted with respect to that of α-Sn bulk. However, for infinitely large NC diameter, the density of states and, hence, the band ordering of α-Sn NCs must converge toward that of the bulk system. In addition, from Fig. 3.13, which shows the energy level schemes depending on the NC size, it becomes obvious, that due to the decreasing spacial confinement the fundamental HOMO-LUMO gap decreases wit increasing NC size. That means, that the energetic distance between the Γ_{8v}-derived HOMO state and the Γ_{6c}-derived LUMO state decreases with rising NC diameter. Together with the necessity of the convergence of the density of states toward the bulk DOS, it has to be concluded, that, for a certain critical NC size d_c, a level crossing between the Γ_{8v}- and the Γ_{6c}-like NC state occurs. For thicknesses above (below) the critical one the NC HOMO state possesses Γ_{6c} (Γ_{8v}) symmetry while the LUMO can be identified with the bulk Γ_{8v} (Γ_{6c}) level.

Unfortunately, the critical thickness is too large to be directly observed by means of *ab-initio* calculations. Therefore, the energy eigenvalues of the Γ_{8v}- and the Γ_{6c}-derived NC states was fitted to an inverse diameter dependence with the constraint of convergence toward the inverted Γ_{8v}-Γ_{6c} band gap of bulk α-Sn. The result is displayed in Fig. 3.14(a). We find the crossing of the HOMO-and LUMO level to occur at a critical thickness of 11.46 nm. For comparison, we applied the tight-binding approximation (see Sec. 2.6) without interatomic spin-orbit coupling to calculate the critical diameter [30]. The results are plotted in Fig. 3.14(b). NCs up

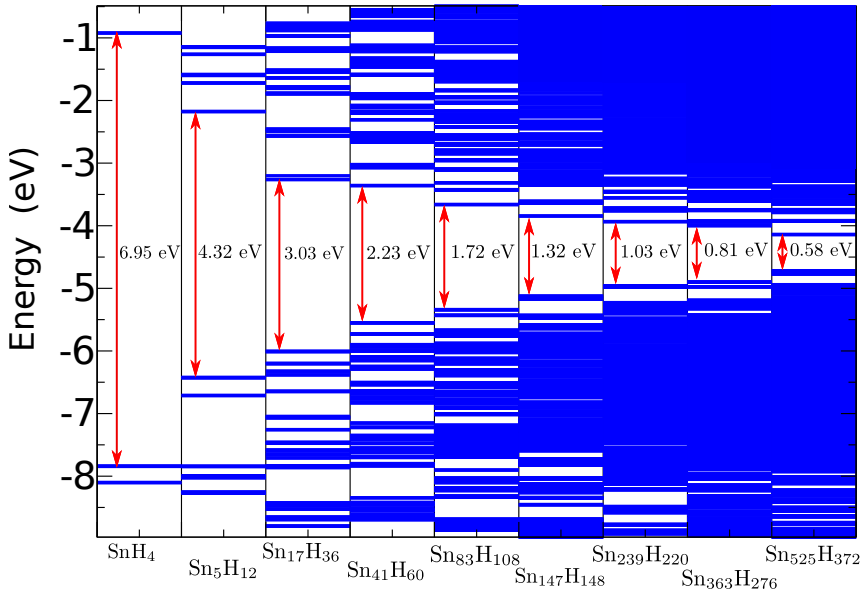

Figure 3.13: Energy eigenvalue spectrum of the α-Sn nanocrystals depending on the NC size. The fundamental HOMO-LUMO energy gaps are indicated by red arrows. The energy scales of the different calculations are aligned by the vacuum level of the electrostatic potentials.

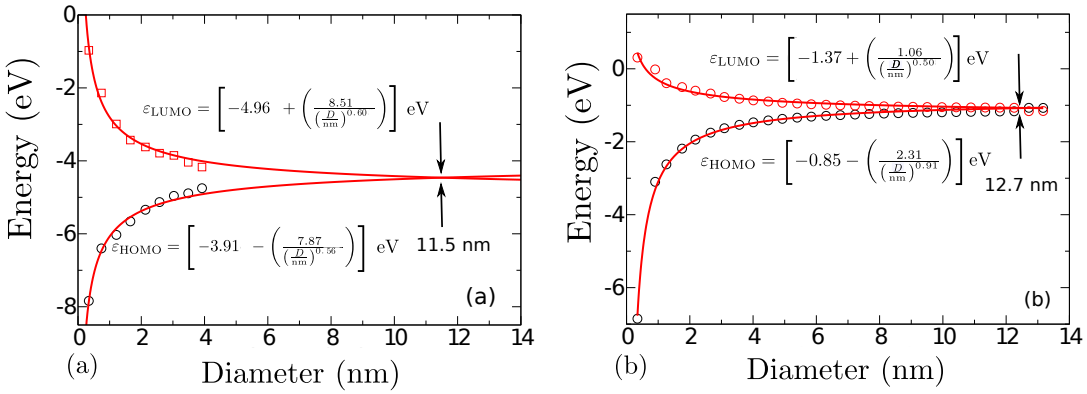

Figure 3.14: NC diameter dependent energetic positions of the Γ_{8v}-, Γ_{6c}-, and Γ_{7v}- derived nanocrystal eigenstates and fitted dependencies. The critical thickness d_c of HOMO-LUMO level crossing is indicated. In (a) *ab-initio* results are depicted, (b) shows tight-binding results.

to 19335 Sn atoms and 4092 H atoms are investigated. However, the identification of the transition within TB is difficult due to the problem of identification of the symmetry character of the HOMO and LUMO states. Therefore, we have fitted the diameter dependence similar as for the *ab-initio* values and identified the critical diameter as the crossing value of the fit curves for the two levels at $d_c = 12.7$ nm. The fit functions of the NC diameter D dependent energy levels denoted in Fig. 3.14(a) and (b) exhibit a dependence on $D^{-\beta}$ with $\beta < 1$. For a 3D spherical potential well model, a D^{-2} dependence of the confinement energy would be obtained [83]. However, *ab-initio* calculations of PbSe, PbTe, SnTe [83] and Ge and Si NCs [87, 149] found a $1/D^{\beta}$ proportionality of the confinement energy with $\beta < 1$. Therefore, the results found in the case of α-Sn NCs seem to be reasonable. The slightly larger diameter found within the TB approximation is a consequence of a fit of the TB parameters to the HSE06 band structure of α-tin. In Sec. 3.3.4 it will be shown, that the HSE values for the pair excitation energies are slightly larger than the LDA ones and, hence, result in a level crossing at somewhat larger diameters.

3.3.4 Lowest pair-excitation energies

The investigation of the topological transition described in the previous section 3.3.3 is based on Kohn-Sham eigenvalues computed within the LDA, which are known to significantly underestimate quasiparticle energy gaps [49]. In this section, it will be shown, that the applied method yields reasonable quasiparticle gaps in the case of zero-dimensional systems and the results described above are thereby verified.

The question to be answered is, how the presence of an electron hole pair influences the fundamental band gap with respect to the electronic ground state. In order to understand this influence, it is appropriate to compare the lowest electron-hole pair excitation energies within three different approximations, the LDA Kohn-Sham gaps, the HSE06 Kohns-Sham gaps, and the ΔSCF method, because they take different aspects of many-particle interactions into account. The results are depicted in Fig. 3.15

The LDA neither regards for quasiparticle corrections, nor excitonic effects. The use of the hybrid HSE06 functional additionally takes into account the short range part of the non-local Fock exchange (see. Sec. 2.2.3.3) and, therefore, quasiparticle corrections are modeled [57, 150]. This results in an increase of the fundamental gap of approximately 1 eV with respect to the LDA gap as can be clearly seen in Fig. 3.15. Unfortunately, NCs with more than 41 Sn atoms cannot be treated within HSE06 due to the computational effort. Most interesting are the excitation energies calculated within the ΔSCF method. They deviate by not more than 30

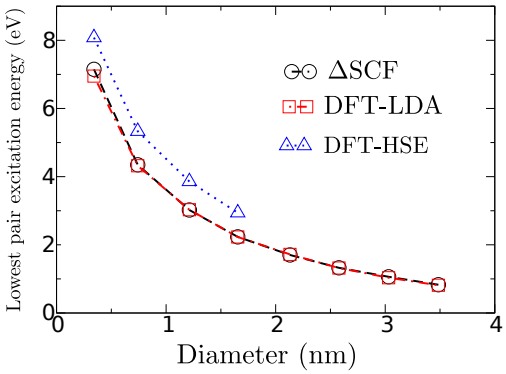

Figure 3.15: Size-dependent lowest pair excitation energies of the NCs obtained from three different approximations.

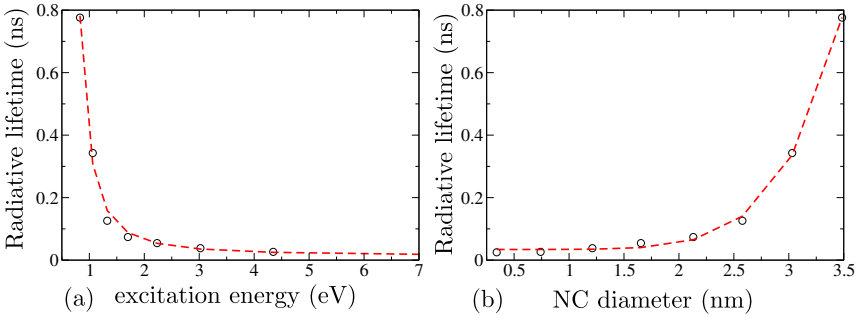

Figure 3.16: Radiative lifetimes of the excited NC states. The dependencies on the NC diameter (a) and on the excitation energy (b) are depicted.

meV from the KS gaps computed within LDA for all NCs with more than one tin atom. Conclusively, the excitonic effects which are additionally taken into account with respect to the HSE06 computations cancel the gap-increasing effect of the quasiparticle corrections. This is in accordance to results reported for Si, Ge, SnTe, PbSe, and PbTe NCs [83, 84, 87, 143] and seems to be a general observation for nanostructures [87, 151]. In the case of SnTe, PbSe, and PbTe nanodots, the DFT-LDA KS gaps underestimate the lowest pair-excitation energy computed within ΔSCF by about 50 meV, which is in close agreement with our result of 30 meV for α-Sn NCs.

The main conclusion from these observations is, that the DFT-LDA based results concerning the determination of the critical thickness presented in Sec. 3.3.3 are verified.

3.3.5 Radiative lifetimes

The radiative lifetime of the excited electron-hole pairs at room temperature in equ. (2.32) depending on the NC diameter and depending on the excitation energy, respectively, is shown in Fig. 3.16. Due to the strong dependence of the lowest pair excitation energy on the NC diameter, the lifetimes also vary significantly with the NC size. We observe an increase from 0.01 ns for the smallest cluster SnH_5 toward 1 ns in the case of $Sn_{363}H_{276}$. The fitted diameter dependence results to $\tau(D) = 0.034\ \text{ns} + \left(\frac{D}{3.65\ \text{nm}}\right)^{6.44}\ \text{ns}$. The excitation-energy dependence of the radiative lifetime can be fitted exponentially:

$$\tau(E^{ex}) = 0.011\ \text{ns} \cdot \exp\left(\frac{3.456\ \text{eV}}{E^{ex}}\right). \tag{3.5}$$

A similar exponential dependence of the lifetime on the excitation energy has been found experimenally for Si and mixed $Si_{1-x}Ge_x$ nanocrystals by laser-induced pyrolysis [152].

The values obtained for the α-Sn NCs are one order of magnitude smaller than those that have been published for Ge NCs [80, 153, 154]. This can be understood in analogy to the lifetimes of Si NCs which are larger than that of Ge NCs by several orders of magnitude [80, 154, 155]. The indirect band gap of silicon decreases the recombination probability with respect to Ge, which has a direct band gap that is only slightly smaller than the indirect one. Such differences have also been measured [111, 156]. The zero-gap of α-Sn can therefore be expected to further increase the recombination probability and therefore to decrease the lifetime of α-Sn NCs with respect to germanium clusters.

3.3.6 Size dependent absorption- and emission properties

The optical absorption spectra, that are identified with the imaginary part of the dielectric function of the investigated NCs, are depicted in Fig. 3.17 together with the photoluminescence peaks. The peak positions of the lowest two-particle excitation energy are shifted manually by several meV to match the values obtained within the ΔSCF method. The photoluminescence (PL) peaks are also taken from ΔSCF calculations. This assures that quasiparticle and excitonic effects are taken into account (see Sec. 3.3.4). A Lorentzian lifetime broadening of 0.1 eV is applied. For a better understanding of the peak structure, the optical absorption maxima are related to the oscillator strengths of the dipole-allowed transitions, which are indicated in the energy-level schemes. The angular-momentum resolved densities of states are also given to illustrate the s- and p character of the states and exemplify,

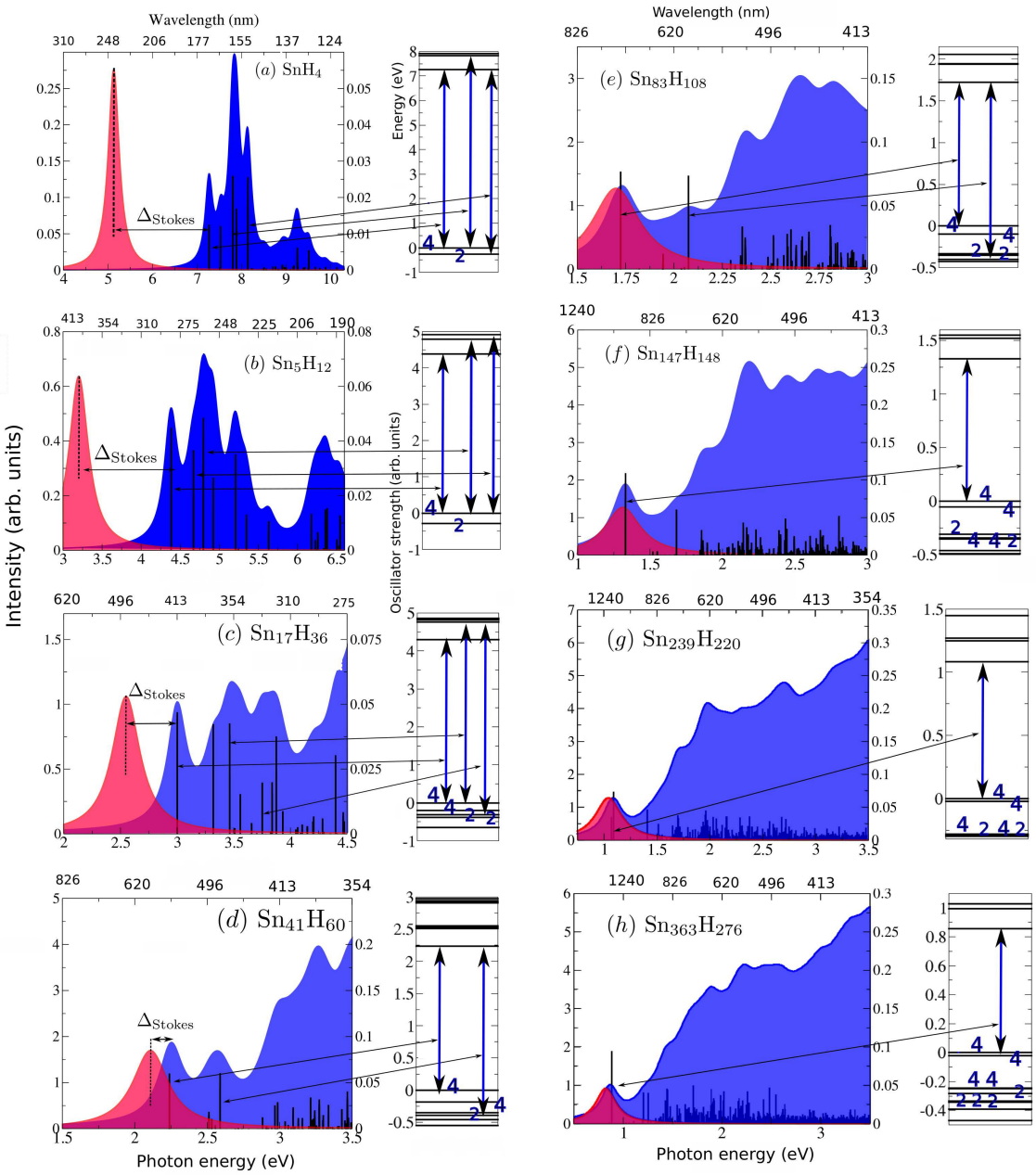

Figure 3.17: Imaginary part of the dielectric function (red) and photoluminescence (blue) of the α-Sn NCs depending on the photon energy. The oscillator strengths of the dipole-allowed transitions around the fundamental gap are indicated by vertical black lines and the corresponding optical transitions are identified in the energy level schemes. The angular-momentum-resolved densities of states are depicted in the panels.

why certain transitions are dipole-allowed or not.

There is a clear red-shift of the absorption edge with increasing NC diameter due to the decreasing confinement and the thereby reduced HOMO-LUMO gap. For all NCs studied, the peak related to the HOMO-LUMO transition is clearly resolved despite of the chosen lifetime broadening of $\eta = 0.1$ eV. This is caused by the the large oscillator strength of this transition because of the band state inversion with respect to the bulk system that has been discussed in the previous section 3.3.3. All clusters studied are smaller than the critical thickness, consequently the HOMO states have a clear p- or Γ_{8v}-character, whereas the LUMO states are formed by s orbitals and have Γ_{6c} symmetry. Therefore, the respective optical transition is dipole allowed. In addition, the HOMO$-1\rightarrow$LUMO transition from the second highest occupied state into the LUMO appears to be dipole-forbidden and its dipole-transition matrix element vanishes for all NC sizes. This transition is energetically close to the HOMO-LUMO transition and would otherwise overlay the first peak due to the chosen lifetime broadening.

In the case of the smaller clusters, there is a clear peak structure of the optical absorption spectrum and each peak can be related to a certain transition from occupied to unoccupied states as indicated in Fig. 3.17. This underlines the importance of the inclusion of SOC in the calculations, because there are significant contributions to the absorption spectra of transitions from spin-orbit split-off Γ_{7v}-like energy levels into the LUMO or energetically close levels. With increasing NC size, the density of states in the energetic vicinity of the fundamental gap increases and much more optical transitions in the same energy interval become possible, which leads to a smoothening of the absorption spectra with increasing NC thickness because of the lifetime broadening.

For a further increase of the NC diameter, a convergence of the absorption spectrum toward the imaginary part of the bulk dielectric function (see Sec. 3.1.4) can be expected due to the convergence of the density of states toward the bulk one. This is not visible in the spectra presented in Fig. 3.17, because the NCs are still even smaller than the critical thickness of level-crossing of the HOMO and LUMO states which has been discussed in Sec. 3.3.3.

Figure 3.17 also shows the lifetime broadened photoluminescence peaks as derived from ΔSCF calculations. Due to the optical Stokes shift, which has been discussed in detail in Sec. 2.4.1, they are red-shifted with respect to the absorption edge. The decreasing influence of the Stokes shift with increasing NC size due to the decreasing impact of the electron-hole pair on the NC geometry is clearly visible. In the case of the small clusters, the PL and lowest absorption peaks are well separated, while

for NCs larger than the $Sn_{41}H_{60}$ one, the PL and the lowest absorption peak can be hardly distinguished.

3.4 Electronic structure of α-Sn(001) surfaces and films

From the analysis of the topology of the bulk band structure in Sec. 3.2, it follows, that strained α-Sn is a strong topological insulator [3]. In this section, (001) orientated films of 0.23% biaxially strained α-Sn with a hydrogen surface passivation are investigated concerning the occurrence of the characteristic topological surface states (TSSs), we use this denotation as a compromise to illustrate their character and their localization simultaneously. The strain models a pseudomorphic growth on a CdTe substrate (see Sec. 2.5.4). The thickness dependence, spin polarization and the energetic position of the TSSs with respect to the characteristic bulk-like eigenstates investigated and compared to theoretical predictions and photoemission studies. Small films up to a thickness of 40 monolayers of α-Sn can be treated within the HSE06 approach, for larger slabs the computational cost become too large. The transition between material and vacuum in the slab causes large density gradients, which makes the application of the MBJLDA method impossible as explained in Sec. 2.2.3. Hence, we are restricted to treat slabs larger than 40 ML of α-Sn within LDA, which is however justified as the wrong bulk band ordering (see Sec. 3.1.1) only affects the occupied bands and therefore does not change the topological invariant. Consequently, the TSSs and their properties should be observable within LDA as well. This is further justified, because the L point of the bulk BZ is not folded onto Γ of the surface BZ and, hence, the the wrong L_{6c} level cannot influence the surface band structure near Γ.

3.4.1 Thin α-Sn films: *ab-initio* description

In Fig. 3.18, the electronic band structure results within LDA are depicted. The results are shown in the vicinity of Γ around the Fermi level. As expected from the band inversion in the bulk and the resulting strong topological invariant, two linear bands crossing at Γ are clearly visible in the surface band structure in Fig. 3.18 obtained within DFT-LDA. The three-dimensional view on the dispersion of the two linear bands in Fig. 3.18 indicates, that the two linear bands form a nearly isotropic Dirac cone with a Fermi velocity of 0.46 (0.41) $\times 10^{-6}$ m/s of the upper (lower) cone. The energy of the crossing point, the Dirac point, lies about $E_D = -0.05$ eV below the Fermi level, which is identified with the highest occupied state. Therefore, both linear states are located below the fundamental gap and, hence, are occupied.

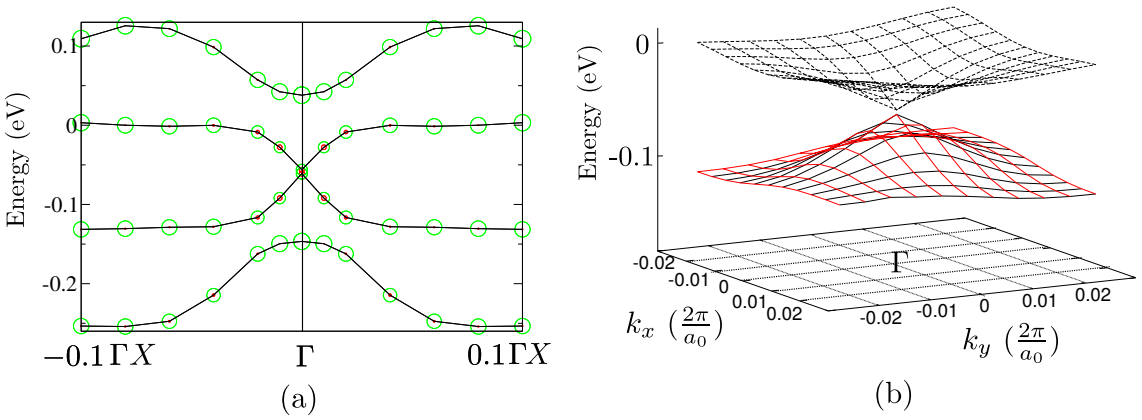

Figure 3.18: Electronic band structure of a 44 monolayer α-Sn(001)$\sqrt{2} \times \sqrt{2}$ slab with 0.23% biaxial strain with hydrogen passivation within LDA. The projections onto atomic s (p) orbitals are indicated by the size of red (green) circles (a). A three dimensional view on the Dirac cone around the Γ point is shown in (b). The Fermi energy is chosen as energy zero.

This fact contradicts the conventional picture of a topological insulator, where the edge states are considered to be metallic, i.e., they are expected to cross inside the fundamental gap. In the case of strained α-Sn this would imply a crossing of the TSSs inside the strain-induced Γ_{8v} gap [4, 9, 25, 129, 138]. Additionally, the projections on atomic orbitals show significant contributions up to 30% of atomic s orbitals, which would not be expected for Γ_{8v}-derived states. This might be an indication of a contribution of the Γ_{6c} band despite the rather underestimated Γ_{6c} energy of -0.69 eV within DFT-LDA (see Sec. 3.1.1). The energetic position of the Dirac point below the Fermi level as well as the s contributions are in agreement with the experimental detection of a topological state emerging from a bulk like Γ_{6c} s-derived level in α-Sn films grown on an InSb substrate [23, 24].

Despite these deviations of the properties of the linear states from the expectations, Fig. 3.19 provides evidence of the topological character of the states, that form the Dirac cone. The wave-function squares of the TSSs averaged over planes perpendicular to the surface normal versus the distance from the surface are shown together with the local magnetization density of the TSSs. Despite the atomic oscillations, the envelope functions in Fig. 3.19(a) show, that the states are located at the surface with an exponential decay of the probability density inside the material with a decay constant of about 10.1 Å. This localization is characteristic for edge states. As a consequence of the rather fast decay of the envelope functions, the overlap of the wave functions from both sides of the 71.2 Å thick slab is negligibly small.

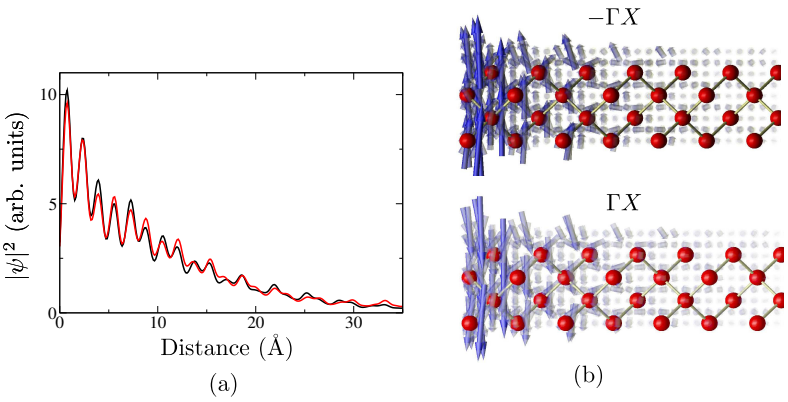

Figure 3.19: Topological properties of the band states forming the Dirac cone. (a) The localization behavior is shown by the wave functions square averaged over planes perpendicular to the surface normal depending on the distance from the surface Sn layer. The wave function of the lower cone is depicted in red, while the black line indicates the upper one. (b) Local magnetization density of the two linear bands. The local spin orientation is indicated by blue arrows. Red dots show the positions of the Sn atoms.

Therefore, the used slab size is sufficient to investigate the TSSs. The spin polarization of the TSSs is clearly visible from Fig. 3.19(b). The linear states possess a spin polarization inside the surface plane perpendicular to the surface normal. At each **k** point, the upper and lower cone exhibit opposite spin polarizations to each other. In each cone, the local magnetisation rotates by 180 degrees comparing opposite directions including the Gamma point. As an example, Fig. 3.19(b) displays the rotation comparing the ΓX and $-\Gamma X$ direction in the upper cone with $\Gamma X||[100]$.

In summary, it is shown, that the Dirac cone is formed by a pair of helical surface or edge states. However, due to the energetic position of the Dirac point below the Fermi level, the states, that form the Dirac cone are occupied and strained α-Sn therefore does not fulfill the original definition of a TI. If the Fermi level would be shifted below the Dirac point, the helical edge states would give rise to spin channels where electrons with different spins travel in opposite directions, and, hence, the QSH effect. It has indeed ben shown experimentally, that high doping of the α-Sn with up to 16% Te atoms can shift the Fermi level below the Dirac point [23].

The results obtained applying the HSE06 XC functional to a 40 ML slab are depicted in Fig. 3.20. As discussed in Sec. 3.1.1, the HSE06 functional corrects the errors of the LDA with respect to the $\Gamma_{8v}-\Gamma_{7v}-\Gamma_{6c}$ band ordering and negative $\Gamma-L$ gap in α-Sn bulk due to the fraction of non-local Fock exchange (see Sec. 2.2.3). The band structure in Fig.3.20(a) is similar to that shown in Fig. 3.18. However, the linear character of the two bands forming the Dirac cone is significantly reduced and a gap of 160 meV is opened between the upper and the lower cone. The main reason

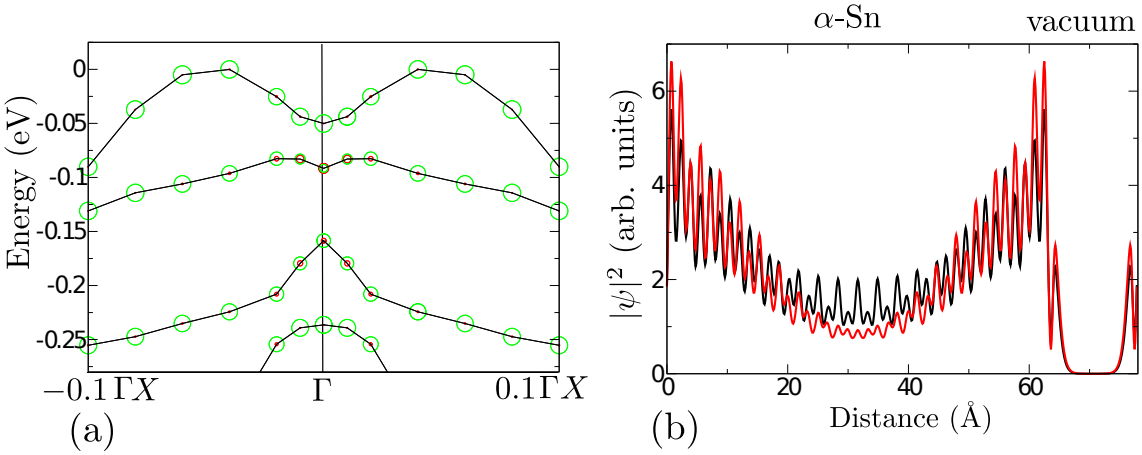

Figure 3.20: (a) Electronic band structure of a 40 monolayer α-Sn(001) slab with 0.23% biaxial strain with hydrogen passivation within HSE06. The projections onto atomic s (p) orbitals are indicated by the size of red (green) circles. The Fermi energy is chosen as energy zero. (b) The envelope functions of the upper (black line) and lower (red line) TSS in the entire unit cell. The two surfaces of the material slab and the vacuum layer are visible.

is the modified spatial variation of the states with respect to that found within DFT-LDA. From the envelope functions in Fig. 3.20(b) it is obvious, that the decay constant of 23 Å is much weaker than that of 10.1 Å of the LDA calculation. This leads to a significant overlap of the wave functions inside the material slab. This interaction causes the formation of a bonding and an antibonding combination of the TSSs and, hence, a level splitting and a gap opening. Test calculations indeed show a decreasing gap with increasing slab thickness. Strong interference between the top and the bottom of α-Sn(001) films grown on InSb was also found to open a gap between the upper and lower Dirac cone experimentally [24], which is in qualitative agreement to our findings within HSE06. Differences in the characteristic thickness may be caused by the two different terminations of the α-Sn film in experiment (α-Sn-air and α-Sn-InSb) in contrast to the symmetric surfaces used for the present calculations.

The position of the Dirac point $E_D = -0.15$ eV is shifted toward lower energies with respect to the LDA result, which is closer to the experimental value $E_D = -0.3$ eV [23]. A further downward shift of the Dirac point with increased slab size as well as a decreasing and eventually vanishing gap between the TSS states due to the decoupling of the wave functions is expected.

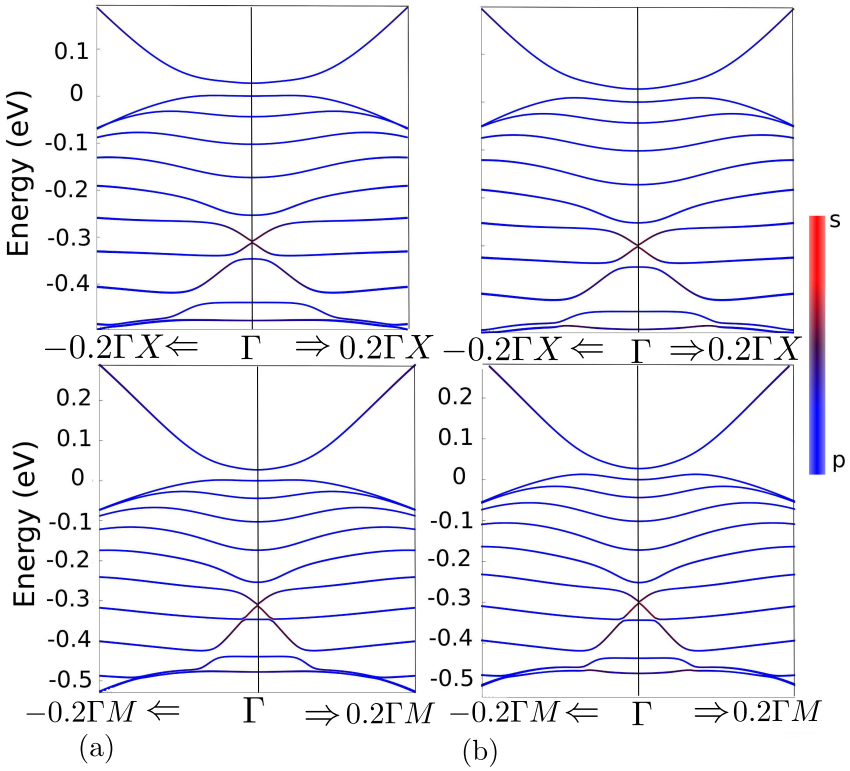

Figure 3.21: Band structure of repeated α-Sn slabs of 84 ML thickness along two high-symmetry directions $\Gamma X \parallel [100]$ and $\Gamma M \parallel [110]$ in the $(001)\sqrt{2} \times \sqrt{2}$ surface BZ obtained in the framework of the TB method. (a) 0.23 % biaxially strained, (b) unstrained. The s- and p-character of the underlying states is illustrated by red and blue colors, respectively. The Fermi level defines the energy zero.

3.4.2 Thick α-Sn films: Tight-binding description

3.4.2.1 Topological character

For a further investigation of the thickness dependence of the TSSs, it is appropriate to apply a tight-binding description to investigate thicker films, that are beyond than what is computationally possible within DFT. The electronic structure of α-Sn slabs with 84 ML is presented in Fig. 3.21 for two opposite high-symmetry directions in the surface BZ for strained as well as unstrained material. Many slab bands occur between the Fermi level position and the region of the Dirac point as a consequence of the used slab approximation. Many of these may be not detectable in ARPER experiments with a large surface sensitivity. The strain does hardly influence the band structures. Conical linear bands are clearly visible, independent of the $\mathbf{k}$ orientation with a Dirac point at an energy of $E_D = -0.3$ eV. A projection of the linear band states onto atomic orbitals confirms the strong s-character predicted by *ab-initio* methods and measurements [23].

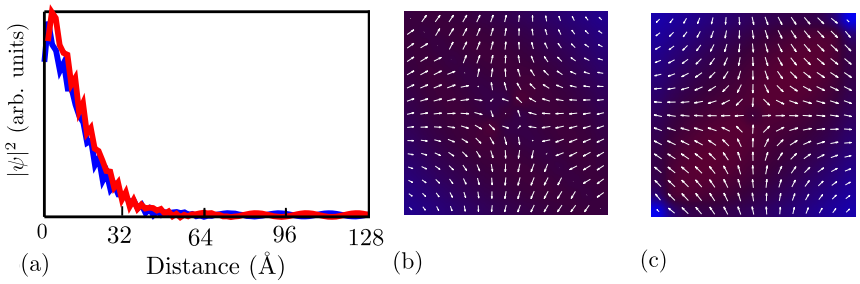

Figure 3.22: (a) Envelope functions for the two linear states crossing at Γ as obtained from the eigenvectors of the TB theory for a slab of slightly strained 160 ML versus the coordinate along the surface normal. Only one surface, i.e. one half of the slab, is considered. The envelope function belonging to the upper (lower) cone is depicted in red (blue). The spin polarization of the upper (lower) cone is shown in (b) ((c))versus **k** in the surface BZ. The center of each panel is chosen at the Γ point. The edge lengths are $0.02\frac{\pi}{a_0}$. The color scheme of the background is the same as used in Fig. 3.21 and indicates the atomic orbital character of the band states.

The topological character of the states near E_D is further illustrated in Fig. 3.22(a). The wave-function squares of the linear states crossing at $E_D = -0.33$ eV have been examined. Two topological edge states separated by 3 meV, which are embedded by projected bulk states, are identified. The TSSs are localized within about 25 atomic layers below each surface and rapidly decay into the bulk regions in qualitative agreement with the results of the *ab-initio* studies. The decay constant amounts to 9 Å. Despite the hydrogen passivation of the surfaces, edge states appear near the slab surfaces. They are obviously protected against surface modifications, which in combination with their localization is a strong indication their topological nature. Since for the studied slab thickness their overlap vanishes, only a negligible gap occurs near the Dirac point.

Another verification for the topological character of these states is their spin polarization. We evaluated the spin polarization as the expectation value of the spin operator with the resulting two-component Pauli spinors. The results for the TSSs are represented in Fig. 3.22. The direction of the spin polarization varies only inside the surface plane and has no component perpendicular to the surface. The spin is rotated by 2π along a circular isoenergy line around Γ of both, lower and upper, Dirac cones confirming their helical character. These results are in formal accordance to the classification of strained α-Sn as strong TI with one Dirac point localized at Γ by Fu and Kane [3]. Considering only the TSS localized at one slab surface, the upper and lower cone show opposite spin polarization. This fact is in agreement with the *ab-initio* results in Fig. 3.19(b) and experimental findings [24].

Nevertheless, there are three surprising features, which somehow contradict the

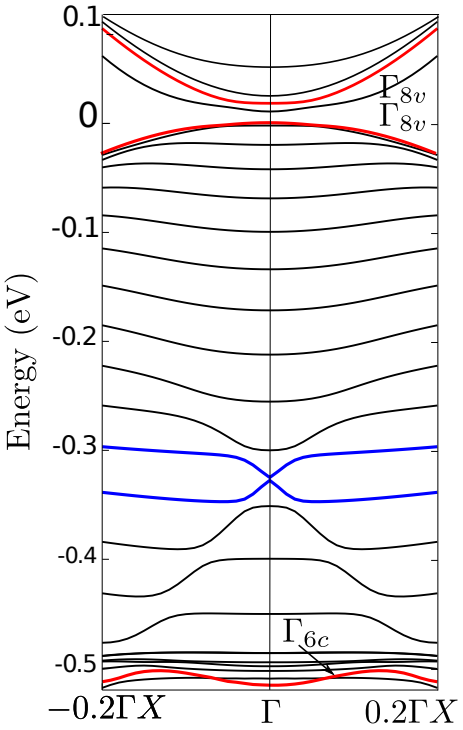

Figure 3.23: Band structure of the (001) surface of α-Sn within the TB method. The band states which show a strong overlap with bulk states at high-symmetry points are indicated by red lines and the respective bulk symmetry is given. The bands mainly related to TSSs are depicted in blue.

conventional picture of topological surface states bridging the strain-induced fundamental Γ_{8v} gap visible from Fig. 3.21: (i) The Dirac cone appears below the strain-induced fundamental gap and is consequently completely occupied by electrons. The slab band structure remains insulating. (ii) Biaxial strain hardly influences the band structure of the slab. (iii) The linearity of the TSS-derived bands is distributed over more bands than the two ones actually crossing at the Dirac point. Energetically close bands develop a linear dispersion continuing the Dirac-cone shape into the Brillouin zone away from Γ. This effect is more pronounced for the lower cone in the [110] direction (lower panels in Fig. 3.21) compared to the [100] one. The three bands below E_D significantly change their dispersion in the vicinity of Γ toward a cone lineshape. In the following sections, these properties will be discussed in detail.

3.4.2.2 Energetic position of the TSSs with respect to the bulk α-Sn derived states

A complete interpretation of the electronic structure results requires a detailed analysis of slab, bulk-derived, and topological states. As an example, the band structure of a thick strained α-Sn slab with a thickness of 160 ML is displayed in Fig. 3.23.

The insulating character of this slab is clearly visible. The Fermi energy lies in the fundamental gap. The Dirac point and the Dirac cones are clearly visible at and around -0.33 eV.

It is obvious, that 11 twofold-degenerate occupied slab bands occur between the upper TSS band near E_D and the Fermi level. In order understand the symmetry and the origin of these subband states, we have studied the overlap integrals of slab band states and bulk states at Γ, X, and L points. We found substantial bulk contributions only for the red bands in Fig. 3.23. The contribution of the irreducible representations of Bloch states at X is vanishing in agreement with the large energetic distances of 1 or 3 eV of these states to the Fermi level (see Sec. 3.1.1). Despite their relatively large energetic distance of -1.3 eV from the Fermi level, the uppermost L valence bands contribute to the two slab bands around the Fermi level. Interestingly, the lowest band with significant contributions of bulk levels is mainly derived from s-like Γ_{6c} states, but also shows some admixture of L_{6c} states. Even the two topological states 3 and 4 forming the apex of the Dirac cones near $E_D = -0.33$ eV exhibit bulk contributions of 10 % Γ_{8v} (13 % Γ_{6c}) in the upper (lower) TSS. However, these projections are significantly lower in comparison to the three other states. The gap of the slab system is mainly formed by light-hole Γ_{8v} and heavy-hole Γ_{8v} states. However, the situation is not completely understood due to the additional slab band in the gap close to the lowest conduction band. This result again indicates deviations from the conventional picture of a 3D topological insulator for strained α-Sn. The TSSs do not appear between the splitted Γ_{8v} states, rather between the heavy-hole-like Γ_{8v} and the Γ_{6c} states almost in agreement with the interpretation of the experimental results [23, 24]. Moreover, in Fig. 3.21(b) it is demonstrated, that the strain-induced Γ_{8v} gap is not necessary for the formation of the TSSs. In any case, the trivial picture, that the TSSs appear in the Γ_{8v} gap opened by strain [3, 23, 129], is invalid here. The reason is, that the use of model Hamiltonians does not account for the real behavior of the slabs versus their thickness.

3.4.2.3 Thickness dependence and observability of TSSs

The question arises how our findings relate to the observation of Dirac cones with a Dirac point below the Fermi level and a lower cone in an energy interval up to -0.6 eV by means of ARPES [23, 24]. For that reason we study the slab band structure of a thick 244 ML slab in a wider range of $\mathbf{k}$ points around the Γ point of the surface BZ and a slightly larger energy region in Fig. 3.24. First of all, in Fig. 3.24(a) the high density of slab bands with a minimum or maximum near the Fermi energy

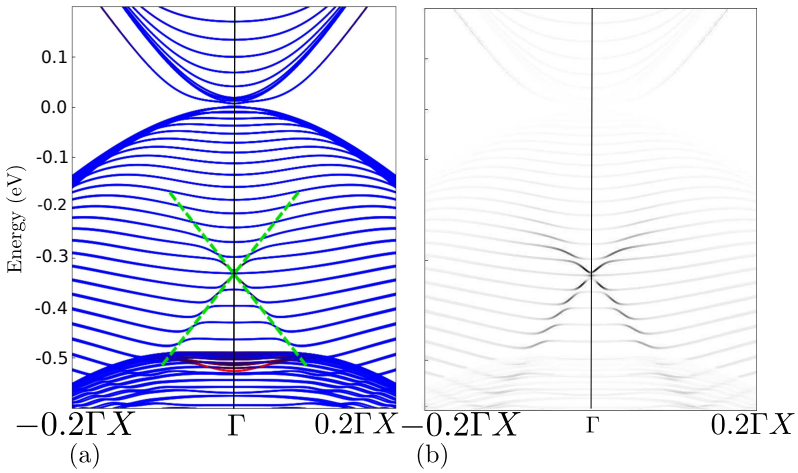

Figure 3.24: (a) Band structure (blue lines) of a 244 ML slab of strained α-Sn around Γ. The Fermi level is used as energy zero. The blue lines essentially represent p-derived states, whereas the red line indicates s-derived states. The green dashed lines guide the eyes to identify the pieces of the TSS-derived bands with linear wave-vector dispersion. (b) Projection of the band states onto atoms in layers close to the surface. The darkness indicates, that the corresponding states possess a large probability to find them closer to the surface, whereas subbands belonging to states more located in the bulk-like region of the slab are practically not anymore visible.

and low-lying bands with a camel-back-like dispersion near −0.5 eV are obvious. The upper bands around the Fermi level look very much as the two bulk Γ_{8c} bands with opposite dispersion but slightly split by strain. The red part of the lower band can be identified with the bulk Γ_{6c} band [30]. These bands have been observed experimentally for relatively large photon energies, i.e., large escape depths of the photoelectrons [23]. The occupied slab bands in between allow the identification of the Dirac point $E_D = -0.33$ eV and linear subbands around Γ in an extremely small energy interval of the order of 0.05 eV as discussed above. However, in Fig. 3.24(b) the adjacent upper and lower subbands show piecewise a linear band dispersion. These pieces seemingly form a much larger Dirac cone, in particular for energies below E_D. The resulting Fermi velocity amounts to $v_F = 0.58 \times 10^6$ m/s, which differs somewhat from the value obtained for the two bands that actually cross at E_D, but is in good agreement with the *ab-initio* and experimental values. In order to demonstrate the topological character of the states leading to the linear segments of the subbands, all band states were projected to Sn atoms in atomic layers below the surface. An exponential weakening is assumed with a decay constant of the order of the escape depth of photoelectrons for small photon energies. The layer contributions are displayed in Fig. 3.24(b) by a decreasing intensity with increasing distance to the surface. The results are qualitatively identical with ARPES results

for photon energies of about 20 eV and, hence, for a pronounced surface sensitivity [23].

Reducing the thickness of the α-Sn slabs, we found qualitatively similar results but with a smaller number of slab bands in the same energy regions. Thereby, the linear dispersion is distributed over a smaller number of subbands and is, hence, less visible. Moreover, there is a clear effect on the Dirac point position with respect to the Fermi level. It almost shows an exponential behavior with a saturation of the position near $E_D = -0.33$ eV with rising slab thickness. Such a tendency has been observed experimentally by Ohtsubo et al. [24] with $E_D = -0.2$ eV for about 30 ML in reasonable agreement with our result. The corresponding value observed by Barfuss et al. [23] is however smaller. The discrepancy may be a consequence of band bending appearing in real semiconductor samples grown on InSb(001) substrates which are likely n-type.

3.5 Two-dimensional nanostuctures: α-Sn and HgTe quantum wells

In this chapter, QW structures based on α-Sn and HgTe are studied within DFT-LDA and MBJLDA. The topological transition in HgTe/CdTe QWs is verified and the influence of real-structure effects such as atomic interface geometry, interface electrostatics, growth direction and the effects of the well material are investigated. Moreover, the properties of QW structures made by the different zero-gap semiconductors α-Sn and HgTe are compared. The two well materials possess different space groups O_h^7 (diamond structure) and T_d^2 (zinc-blende structure) (see Sec. 2.5.1). The spin-orbit interaction, in particular that in the p-derived valence states, is different due to the contribution of both atoms in the unit cell (α-Sn) and mainly the anion (HgTe) to the states at the top of the valence bands, and the different local electrostatic properties due to the different bonding character in the QW layers and their interfaces with the CdTe barrier material. Therefore, the similarities and differences of the two embedded zero-gap semiconductors on the formation of quantum-well, edge and interface states is studied in detail. In the first part, the interface electrostatics and band offsets between barrier and well materials are discussed, which allows for a detailed analysis of the composition of interface states later on. The second part starts with an investigation of the electronic properties of QWs with a (001) interface normal direction, which exhibit the topological transition from a trivial insulating phase into the QSH phase for both, HgTe and α-Sn QWs. This discussion is followed by the analysis of (110) orientated QWs, where significant differences in

the electronic structures of HgTe and α-Sn are occur. While HgTe/CdTe(110) QWs behave similarly to the (001)-orientated QWs, is shown, that despite the protected character of the edge states, a break in time-reversal symmetry anticipates the occurrence of the QSH phase. This is further demonstrated by electronic-structure calculations of α-Sn/InSb and HgTe/InSb(110) QWs.

3.5.1 Band offsets and interface electrostatics

QW thickness		Orientation	
d_1 (nm)	N	ΔE_v (eV)	
		(110)	(001)
0.9	4	0.53	-
2.1	12	-	0.45
2.8	12	0.48	-
4.0	24	-	0.37
4.5	28	-	0.25
4.8	20	0.23	-
5.3	32	-	0.18
5.7	24	0.13	-

Table 3.3: Valence band discontinuities for (110) and (001) HgTe-CdTe QWs depending on the QW thickness d_1 and the respective number of monolayers. The positive sign indicates, that the HgTe Γ_{8v} level is inside the CdTe gap.

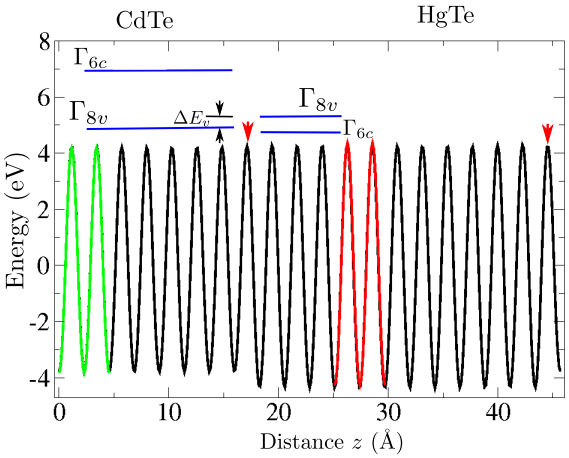

Figure 3.25: (Color online) Plane-averaged electrostatic potential $V_{es}(z)$ (black line) of a $(HgTe)_{12}(CdTe)_8(110)$ superlattice with a period $d_1 + d_2$=47 Å. Two oscillations of the potentials of HgTe bulk (red line) and CdTe (green line), used for alignment of band states, are depicted. Since the relative positions of the bulk band edges is known (see blue levels in inset), the valence band discontinuity ΔE_v can be directly read. The space-averaged electrostatic potential of the superlattice is used as absolute energy zero. The vertical red arrows indicate the interface positions.

The bulk band structures discussed in Sec. 3.1 indicate the formation of type-III heterostructures between the zero-gap semiconductors HgTe and α-Sn and a semiconductor with reasonable fundamental gap of more than 1 eV such as CdTe [95]. The Γ_{8v} level of the zero-gap material is located inside the fundamental band gap of the wide gap semiconductor, such that the bottom of the conduction subband and the top of the valence subband of the interface are formed in the same semiconductor layer, here HgTe and α-Sn. Hence, the situation is very similar to the type-I case with a finite positive gap [95]. However, theoretical predictions and experimental findings show, that in a HgTe/CdTe quantum well structure the band gap should be almost continuously varied from a negative band gap to a zero one or even to a positive gap as a function of the HgTe thickness d_1 [7, 26]. This topological transition has to depend on the band discontinuities between HgTe and CdTe [157]. In the present section, we discuss these quantities, in particular the valence band offset $\Delta E_v = \varepsilon(\Gamma_{8v}, \mathrm{A}) - \varepsilon(\Gamma_{8v}, \mathrm{CdTe})$ between the Γ_{8v} level in A=HgTe and A=α-Sn, respectively, and the Γ_{8v} one in CdTe. The "conduction band" offset ΔE_c is more difficult to define because of the negative *sp* gap in HgTe and α-Sn. Nonetheless, a reliable possibility could be the difference between the Γ_{6c} levels in CdTe and HgTe α-Sn, respectively.

The calculation of reasonable band offsets, which are comparable with experimental values, is difficult because of the presence of interfaces. The so-called natural band discontinuities can serve as a first approach by aligning the corresponding two bulk band structures. One reasonable possibility is the use of the branch points E_B [157–159]. The main idea is the existence of a charge neutrality level in the fundamental gap, where the character of electronic states changes from acceptor- to donor-like. We use the approximate method of Schleife *et al.* [159], which leads to band discontinuities for cubic and hexagonal compounds in reasonable agreement with experimental data for many semiconductors [159, 160] in combination with band structure calculations based on HSE06 XC functionals. With respect to the Γ_{8v} position, we find E_B = 0.71 eV (CdTe), 0.10 eV (HgTe), and -0.52 eV (α-Sn) in great agreement with results of other computations [157]. The resulting natural band discontinuity between HgTe and CdTe $\Delta E_v = 0.72$ eV is still smaller than the fundamental gap of CdTe but too large in comparison with other calculations and measured values [124, 157, 161, 162] indicating, that the branch-point method might not be applicable to HgTe/CdTe heterosystems. In α-Sn/CdTe heterostructures, a larger natural valence band discontinuity of $\Delta E_v = 1.26$ eV is predicted compared to the HgTe/CdTe interface, which is in agreement with an experimental value of $\Delta E_v = 1.1$ eV [163].

The determination of the band offsets by the alignment of branch points derived from bulk band structure calculations neglects effects of the real interfaces and the electrostatics in heterostructures [160, 164]. Another problem in real QW structures is related to confinement of electrons and holes in the well material HgTe or α-Sn, respectively, that should reduce the band discontinuities. Therefore, in a second approach, the valence band discontinuities using the plane-averaged electrostatic potentials $V_{es}(z)$ derived from the local part of the Kohn-Sham one with z parallel to the SL axis of the investigated HgTe/CdTe superlattices and the corresponding bulk systems, are determined. As the energetic positions of the bulk band edges Γ_{8v} and Γ_{6c} relative to the bulk potentials $V_{es}(z)$ are known, the band discontinuities of a given superlattice can be formally derived from the comparison of $V_{es}(z)$ for bulk compounds and the superlattice. This procedure is visualized in Fig. 3.25 for the (110) case of a HgTe/CdTe QW structure. The direct comparison is possible, since the amplitudes and widths of the oscillations with the atomic layers remain the same in the superlattices, independent of the interfaces, their distances, and the small confinement in the HgTe (α-Sn) films, respectively. Only the relative position of the oscillations in the HgTe (α-Sn) and CdTe layers seems to be influenced, mainly by the electrostatics in the superlattice.

The resulting valence band discontinuities ΔE_v between HgTe and CdTe are summarized in Table 3.3. They depend on the HgTe QW thickness d_1 and the QW orientation, (110) and (001). As a surprise, the ΔE_v values decrease with increasing thickness d_1. For small QW thicknesses $d_1 < 3$ nm, the results are in excellent accordance with more recent experimental findings of $\Delta E_v = 0.53$ eV [124], while in the case of intermediate thicknesses $d_1 \approx 4$ nm the results in Table 3.3 are close to values $\Delta E_v = 0.35 \pm 0.06$ eV from earlier measurements [157]. The ΔE_v calculated for the largest QW thicknesses are small, in agreement with the early assumptions of vanishing valence band offsets based on the common-anion rule [165]. In the case of an HgTe/CdTe interface, this rule states, that the valence band edges at either side of the interfaces are formed by Te states, and, as the Te atoms in HgTe and CdTe are equivalent even with regard to the crystal symmetries, the valence band edges are nearly energy-matched resulting in a small valence band discontinuity [165]. The observed tendency is rather independent of the QW orientation. For relatively small QW thicknesses of $d_1 = 2.1$ nm ((001)) and 2.8 nm ((110)) the offsets only differ by 30 meV. However, it is questionable, if the determination of band discontinuities does make sense for HgTe layers smaller than 1 nm as has been done in Ref. [124], because it is improbable, that such a small layer behaves like HgTe bulk. In any case the valence band offsets in Table 3.3 indicate, that at least one hole state should be

confined in the HgTe layers independent of the actual value d_1.

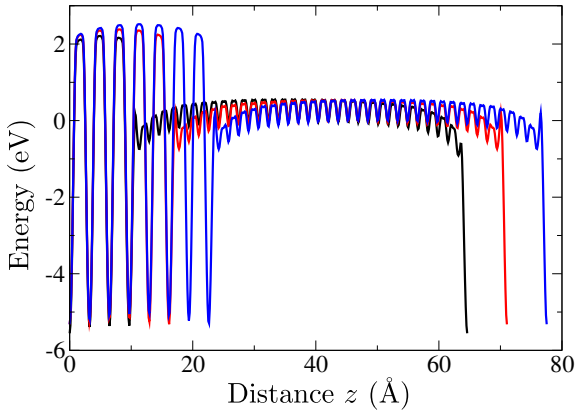

Figure 3.26: (Color online) Plane-averaged electrostatic potential $V_{es}(z)$ of $Sn_{66}Cd_6Te_8(001)$ (black line), $Sn_{66}Cd_{12}Te_{14}(001)$ (red line), and $Sn_{66}Cd_{16}Te_{18}(001)$ (blue line) QWs. The space-averaged electrostatic potential of the superlattice is used as absolute energy zero.

In α-Sn (110) superlattices, the valence band discontinuity calculated via the alignment of the electrostatic potentials amounts to $\Delta E_v = 1.1$ eV, which is in excellent agreement with the experimental value $\Delta E_v = 1.1$ eV [163]. and is rather independent of the QW thickness. Moreover, this value is by a factor 2 larger than the largest value calculated for HgTe QWs, which is in qualitative agreement with the results obtained using the branch point method. This trend is even more pronounced in α-Sn/CdTe QWs with (001) orientation. Actually, we find the fundamental gap of these QW structures to be completely inside the projected valence bands of CdTe, which seems to be obviously unphysical. However, as will be discussed in the next section 3.5.2, the required thicknesses of the α-Sn layer are much larger than those of HgTe in the respective QW structures, which inevitably limits the barrier thickness of CdTe to 9.6 Å for reasons of computational cost. In addition, as explained in Sec. 2.3.4, due to the structure of the CdTe barrier consisting of polar layers in (001) direction, non-stoichiometric barriers must be used to avoid an intrinsic electrostatic saw-tooth potential. The small barrier thickness together with the violated stoichiometry may be the reason for the rather unphysical band discontinuities. This is verified by the comparison of the plane-averaged electrostatic potentials of QWs containing 16 double layers of α-Sn but increasing CdTe barrier thicknesses of 9.6 Å, 16.1 Å, and 22.5 Å in Fig. 3.26. It is obvious, that the electrostatic potential in the α-Sn region 10 Å away from the interface is well converged, as the atomic oscillations are equally high. In the CdTe part of the QW, there is a clear upward shift of the atomic oscillations with increasing barrier thickness. The difference between the smallest barrier and the largest one amounts roughly 300

meV. This upward shift of the energy scale of the superlattice with respect to that of CdTe bulk causes the conduction band minimum of bulk CdTe to be just above the conduction band minimum of the respective supercells. However, the envelope of the maxima of the atomic oscillations of the electrostatic potential is not flat even in the case of the largest barrier considered here, indicating that the potential is not yet completely converged and a further increase would therefore lead to a further decrease of the valence band discontinuity. The valence band discontinuities is found to be independent on the thickness of the α-Sn layer. Therefore, the situation with the fundamental gap being inside the projected bulk gap of CdTe, which is found for the 22.5 Å wide CdTe barrier, will be considered in the discussion of the electronic band structure, despite the fact, that in the actual calculations smaller CdTe barriers were used. The different confinement situations cause significant differences in the subband structure between HgTe and α-Sn superlattices, which will be discussed in the following sections.

In the case of an $(HgTe)_{12}(InSb)_8(110)$ QW, the valence band discontinuity amounts to $\Delta E_v = 0.22$ meV. Because of the small fundamental energy gap $E_g = 0.31$ eV of InSb (see Sec. 3.1), the Γ_{8v} level of HgTe is much closer to the conduction band edge of InSb than its valence band edge, which implies, that the situation is similar to the α-Sn/CdTe interfaces.

3.5.2 Electronic properties of HgTe/CdTe(001) and α-Sn/CdTe(001) QW structures

3.5.2.1 Subband dispersion and orbital symmetry of the QW states close to the Fermi level

The QP subband structures of the $(\alpha\text{-Sn})_N(CdTe)_{11}(001)$ and $(HgTe)_M(CdTe)_8(001)$ multi-QW structures with varying well thicknesses N=49, 53, and 57 (M =24, 28, and 32) are displayed in Fig. 3.27. They are derived from those of the corresponding superlattices and plot versus the 2D BZ of the $(001)\sqrt{2} \times \sqrt{2}$ interface [77] around the Γ point in the cubic directions $\pm\Gamma X \parallel[\pm 100]$ (toward the midpoint of an edge) in a relatively small energy interval around the Fermi energy. The subbands are mainly derived from states formed in the respective well material HgTe and α-Sn. In the HgTe QWs, only the lower occupied subbands possess contributions from CdTe as indicated by the energetic overlap with the projected bulk valence band structure of CdTe in Fig. 3.27. In the α-Sn QW structures, due to the different valence band discontinuity between α-Sn and CdTe (see Sec. 3.5.1), the projected conduction band edge of CdTe is energetically close to the conduction band edge of the QW structures. All heterostructures represent insulators with an extremely

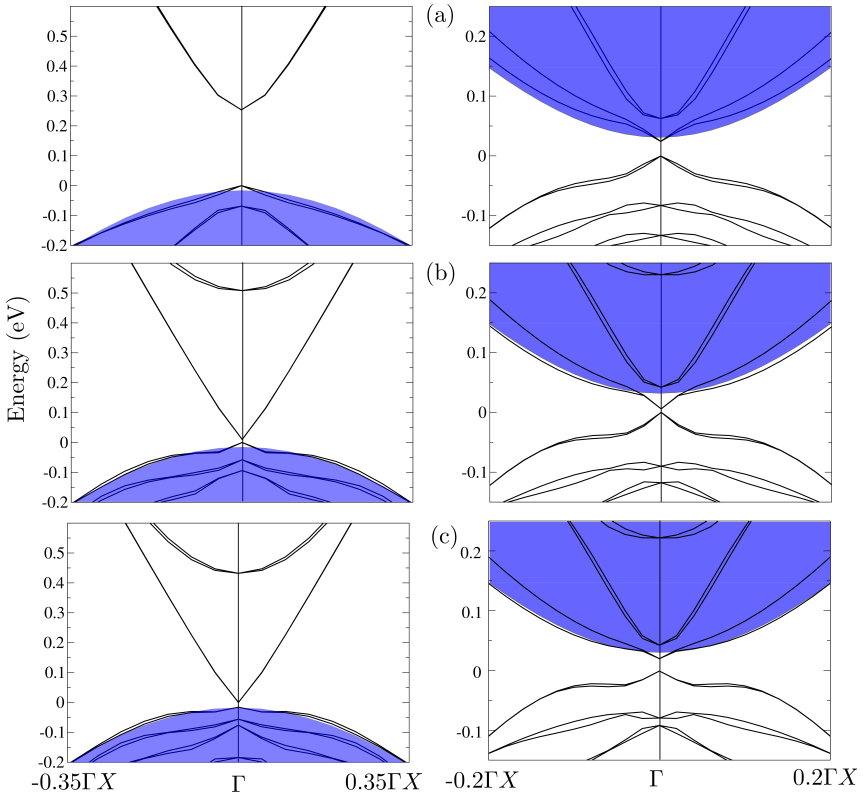

Figure 3.27: Subband structures of $(\alpha\text{-Sn})_N(\text{CdTe})_{11}(001)$ (left panels) and $(\text{HgTe})_M(\text{CdTe})_8(001)$ (right panels) superlattices for different QW thicknesses $M = 24$ ($N = 49$) (a), $M = 28$ ($N = 53$) (b), and $M = 32$ ($N = 57$) (c). The blue background indicates the projected bulk band structure of the CdTe barrier material. The energy of the highest occupied SL state is used as energy zero.

small fundamental gap at Γ for the SLs with $N = 53$ or 57 (M =28 or 32).

The subband structures in Fig. 3.27 exhibit a drastic variation with the thickness of the HgTe and α-Sn QWs, respectively, due to confinement effects on electron and hole states. In order to classify the (sub)band ordering, their orbital character at Γ with varying QW thickness is depicted in Fig. 3.28. The lowest-energy p- and hence Γ_{8v}- derived subband may contain holes (H) in conventional semiconductor band structures such as CdTe. The highest-energy s- and hence Γ_{6c}-derived subband may be an electron (E) band for normal band ordering. For $N < 28$ in HgTe QWs ($M < 53$ in α-Sn QWs), the orbital-symmetry projections in Fig. 3.28(a) show, that the lowest unoccupied level is mainly formed by s orbitals, whereas in the subband below the Fermi level at Γ the projections onto p orbitals dominate. A trivial insulator with a similar ordering of the band symmetries as in bulk CdTe appears in these QWs. For large enough thicknesses e.g. $N = 57$ ($M = 32$), the subbands of the QW structures are inverted in agreement with the bulk band structure of HgTe (α-Sn)(see Sec. 3.1.1). The inverted subband structure, especially the inversion

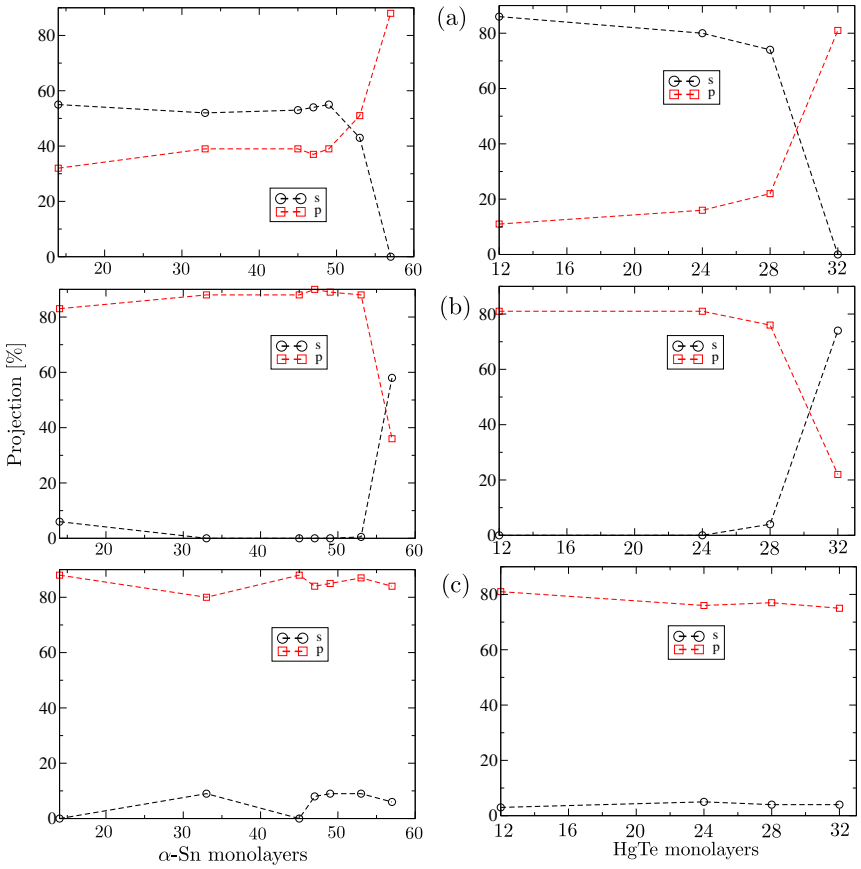

Figure 3.28: Contributions of atomic s- and p orbitals to the subband states close to the Fermi level of $(\alpha\text{-Sn})_N(\text{CdTe})_{11}(001)$ (left panels) and $(\text{HgTe})_M(\text{CdTe})_8(001)$ (right panels) superlattices depending on the QW size. In (a), the lowest unoccupied subband is depicted, while (b) refers to the highest occupied subband, and (c) shows the second highest occupied subband.

between E and H subbands near Γ, leads to the occurrence of the quantum spin Hall effect, i.e., a topologically nontrivial phase [7, 26]. When the thickness of the QW is increased, the energy of the H (E) subband increases (decreases) as a result of the quantum confinement. As a consequence, formally a level crossing should appear at a critical thickness of $d_c \approx 4.6$ nm and $d_c \approx 8.5$ nm in HgTe Qws and α-Sn QWs, respectively, as described in Fig. 3.29. A further increase of the HgTe (α-Sn) thickness toward $d_1 = 5.3$ nm ($d_1 = 9.4$ mn) causes an inversion of the energetic ordering of s- and p- derived subbands toward the bulk situation of HgTe (α-Sn) as shown in Fig. 3.28. However, it has to be underlined, that especially the atomic s contributions are restricted to the Γ point. Away from Γ, there is a rapid increase in atomic p orbital character. In summary, a level-inversion for $d < d_c$ is observed in (001) QW structures of both materials. From Fig. 3.28(c), it is obvious, that the second highest occupied subband is formed by atomic p orbitals, independently of the QW thickness and remains, hence, uninfluenced by the topological transition.

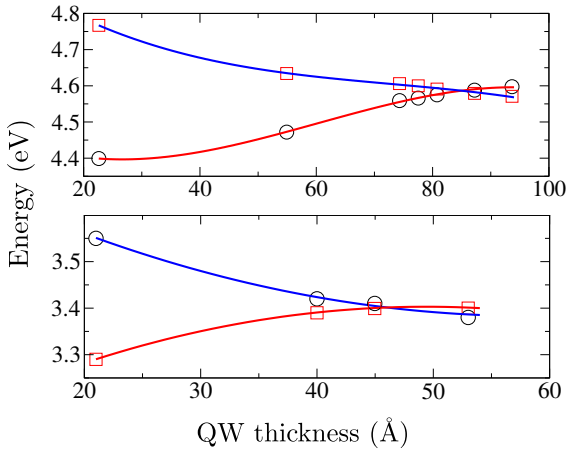

Figure 3.29: (Color online) Thickness variation of *s*- and *p*-derived subband energies E (blue) and H (red) at Γ for the α-Sn(001) (upper panel) and HgTe(001) (lower panel) QWs with CdTe barriers. The cubic interpolation of the band energies indicates a level crossing for both materials.

It has to be mentioned, that the critical thickness d_c in HgTe QWs derived from Fig. 3.29(b) is somewhat smaller than the corresponding thicknesses derived theoretically from models using an effective four-band $\mathbf{k} \cdot \mathbf{p}$ model Hamiltonian [3, 5]. The reasons are (i) that the true symmetry is broken down to the axial rotation symmetry around the interface normal and inversion symmetry, (ii) the consideration of only four bulk bands, and (iii) the neglect of interfaces and true energy barriers. The *ab-initio* value of d_c is also smaller than the experimental value [7]. Experimentally the QW thicknesses are taken from the growth data for modulation-doped HgTe/$Hg_{0.3}Cd_{0.7}$Te QW structures fabricated by molecular beam epitaxy [7]. The findings indicate that the nominal 5.5 nm structure shows the behavior of a trivial insulator, while the 7.3 nm structure exhibits the QSH insulator state. The thicknesses have been calibrated by x-ray reflectivity measurements. The reduced Cd content and, hence, the much smaller barriers make the precise classification of an interface position unlikely and may change the critical thickness d_c. Recently, Anversa et al. published *ab-initio* results obtained within the GGA approximation with an additional intraatomic Coulomb interaction of localized electrons for HgTe/CdTe(001) QWs [166]. The topological transition was found to occur between 5 and 6.6 nm, strongly depending on the CdTe barrier thickness. Unfortunately, no values for comparison of the α-Sn QW results have been published so far.

Most interesting is the intermediate region with an almost vanishing gap at Γ. For instance, for $d_1 = 4.8$ nm in HgTe Qws and $d_1 = 8.08$ nm in α-Sn Qws (Fig. 3.27(b)), the lowest empty and highest occupied subbands are nearly degenerate at Γ and show a linear $\mathbf{k}$ dispersion parallel to the interfaces with a Fermi velocity of

$v_F = 0.69 \times 10^6$ m/s and $v_F = 0.19 \times 10^6$ m/s, respectively, in $\Gamma \to X$ direction. As a result, Dirac cones, although, in the case of HgTe QWs, slightly smoothed off near their apex due to the gap opening, are formed. For the HgTe QW, there are drastic differences between the empty and the occupied subbands. In the occupied case, the linear character is restricted to an extremely small region around Γ. In the case of α-Sn as well material, the upper cone is restricted to a much smaller region around the Γ point compared to the HgTe case, and, consequently, the lower cone exhibits a very similar shape. However, the orbital picture is somewhat different from that, which was predicted from toy models in both QW structures. The linear conical bands near Γ do not only consist of p states. Rather s contributions are observed in the first empty subband, i.e., in the upper Dirac cone for both well materials. Near the level crossing, some orbital mixing appears in contrast to the model studies [3, 5]. Apart from the apex regions in HgTe QWs, the Dirac cones are a direct QW realization of massless Dirac fermions, electrons and holes. The predictions by means of a tight-binding method, that the bulk inversion asymmetry of the zinc-blende structure leads to a shift from the center of the BZ to asymmetric $\mathbf{k}$ points near Γ, where an actual crossing of the E and H bands happens, at least partially due to the SOC-induced band splitting discussed above[167], cannot be confirmed. One reason could be an overestimation of the interatomic SOC within the tight-binding method, because it uses the same matrix element as for the intraatomic SOC.

The symmetry inversion and the existence of linearly dispersed states is, however, insufficient for the identification of a QSH phase. In the following sections, their edge character and chirality of the subbands bridging the fundamental gap will be shown. Nevertheless, the inverted region is referred to as QSH phase from now on.

3.5.2.2 Localization properties of the QW states close to the Fermi level: edge states

In order to find out the relation of the Dirac-cone like features to edge states, the localization of the highest occupied, the second highest occupied, and the lowest empty states on the QW thickness d_1 are visualized in Fig. 3.30. Their wave-function squares are plotted along the interface normal. The atomic oscillations are clearly visible. The variation of the maxima may be interpreted as the behavior of an envelope function, which may be comparable with results of the $\mathbf{k} \cdot \mathbf{p}$ theory. Qualitatively, are very similar for both well materials, HgTe and α-Sn, comparing the respective QWs in the same topological phases, i.e. the trivial insulating phase (3.30(a)), the transition region (3.30(b)), and the QSH phase (3.30(c)).

In the case of the smallest QWs, which are considered as trivial insulators (see

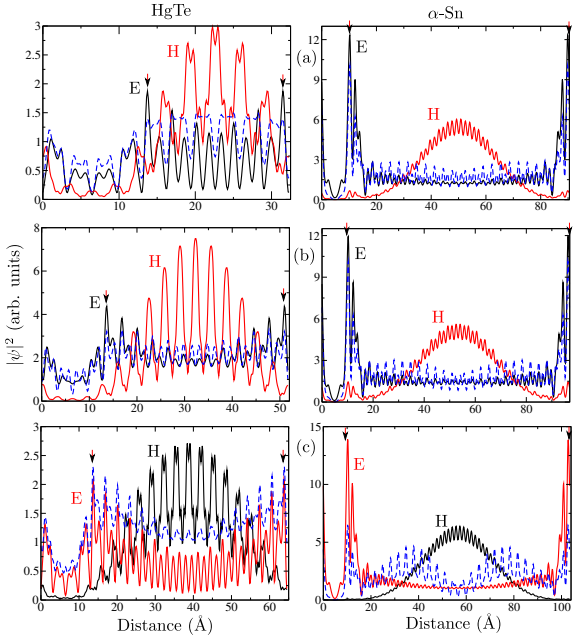

Figure 3.30: (Color online) Wave-function square of the lowest unoccupied (black), the highest occupied (red), and the second-highest occupied (blue) states at Γ averaged over planes perpendicular to the QW orientation [001] as a function of the distance z for different QW thicknesses of 2.1 nm (a), 4.5 nm (b), and 5.3 nm (c) of HgTe QWs (right panels), and 8.1 nm (a), 8.8 nm (b), and 9.4 nm (c) of α-Sn QWs (left panels). Red arrows indicate the position of the interfaces.

Fig.3.30(a)), the probability density of the lowest unoccupied state is localized at the respective interface decaying exponentially inside the HgTe (α-Sn) layer. Inside the QW layer, the probability density is close to zero, indicating the decoupling of the interface states on both sides of the barrier. The shape of the envelope functions is more pronounced in the case of the α-Sn QWs due to the much larger well thickness with respect to the HgTe QW. Due to the localization at the barrier between the topological insulator HgTe (α-Sn) and the trivial insulator CdTe, but inside the topological non-trivial bulk material, and, hence, at the edge of the bulk TIs, states with a similar localization probability will be referred to as edge states. In the case of both well materials, the envelope function of the highest occupied state clearly exhibits the shape of an $n = 1$ confined state in a rectangular QW, which is localized inside the well material and has a negligibly small probability density inside the barrier CdTe layer. The second highest unoccupied state in the α-Sn QW has an elevated probability density at the edges very similar to the lowest unoccupied one, however, there are two much smaller maxima inside the α-Sn layer, similar to an $n = 2$ confined QW state. Hence, there seems so be some kind of intermixing of confined states with edge states, which is remarkable, as edge states are considered to be topologically protected. However, in the used fully self-consistent procedure

including XC on the MBJLDA level (see Sec. 2.2.3.4), and a real atomic structure of the interfaces and barrier materials with finite band discontinuities an intermixing is possible. The states only have to follow the tetragonal symmetry of the multi-quantum well structures. In the case of the HgTe QW, the second highest occupied band is a clear $n = 1$ confined state with one maximum of the envelope function, which is mainly localized inside the HgTe layer.

For the QWs near the critical thickness of level inversion (see Fig.3.30(b)), the localization properties do not change significantly. The only difference is found in the HgTe QW, where the second highest occupied state shows a spatial variation which is characteristic for edge states. Consequently, near the critical thickness, the picture is similar for both well materials. The highest occupied states are identified as $n = 1$ confined states, while the second highest occupied states as well as the lowest unoccupied states exhibit edge state like localization properties. The only difference is, that in the HgTe QWs the decay of the envelope functions inside the HgTe layer is rather slow.

In the inverted regime, i.e. the largest QWs studied, which is shown in Fig. 3.30(c), there is a significant change in the localization properties of the states close to the Fermi energy. For the HgTe QW, the second highest occupied state still shows edge-state like localization, while in α-Sn, the combination of a $n = 2$ QW state with a strong localization at the edges is increased with respect to that shown in Fig. 3.30(b). In the case of both well materials, the envelope functions of the highest occupied and the lowest unoccupied state are interchanged with respect to the situation in Fig. 3.30(b), corresponding to the interchange in the respective atomic s and p orbital symmetries, i.e., the topological transition, which has been described in Sec. 3.5.2.1.

It can be concluded, that the inversion of the band symmetries at $d = d_c$ causes a significant change of the character of the states closest to the Fermi level. QW states with strong p character exhibit properties of an edge state independent of their occupation, while those with strong s contributions tend to be $n = 1$ confined states. The transport measurements [26] of n-modulation-doped HgTe/$Hg_{0.3}Cd_{0.7}$Te structures indicate transport in edge states with a thickness above the critical one. According to Fig. 3.30(c), the electrons are however filled into a $n = 1$ QW state. Nonetheless, one has to take in mind, that for the low-barrier material the situation could be closer to the situation depicted in Fig. 3.30(b) where indeed electrons are filled into the corresponding edge state which we should not only discuss in terms of its localization. In a small range around the Γ point, even the $n = 1$ QW state in Fig. 3.30(c) gives rise to a subband with linear dispersion. However, the low-barrier

$Hg_{0.3}Cd_{0.7}Te$ material may change the situation drastically with respect to the character of the lowest subband states at Γ but also with respect to the enlargement of the critical thickness d_c. In addition, the QW size-dependent localization of the second highest occupied state makes clear, that the edge character is not restricted states with linear dispersion. This fact indicates, that in a real quantum well structure around Γ the electron- and hole-like edge states may embed a conventional QW state.

3.5.2.3 Spin polarization of the edge states: characterization of the QSH phase

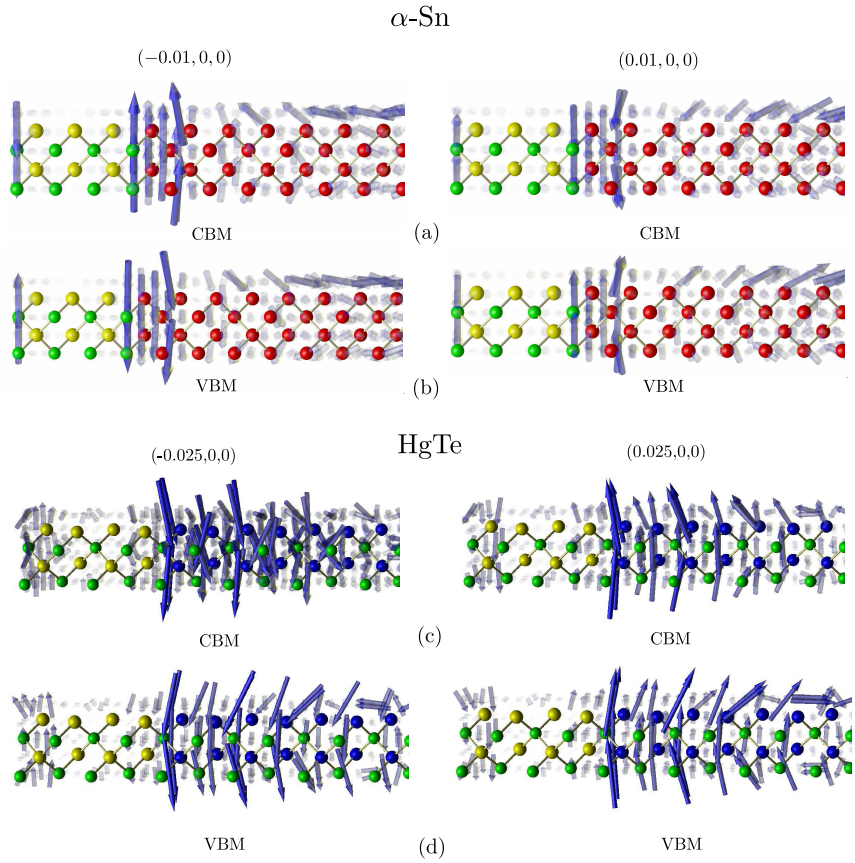

Figure 3.31: Local magnetization of the lowest unoccupied state (a) and (c), and the highest occupied state (b) and (d) in the vicinity of the Γ point in $\pm\Gamma X$ direction of a $(\alpha\text{-Sn})_{53}(CdTe)_{11}(001)$ QW (upper panels) and a $(HgTe)_{28}(CdTe)_8(001)$ (lower panels) in the region of the respective interface. A view from [010] is depicted. The points (b_1,b_2,b_3) mark the location of the considered state in **k** space in units of the reciprocal lattice.

The local spin orientations at Γ for the QW structures with $d_1 = 4.8$ nm (HgTe) and $d_1 = 8.8$ nm (α-Sn), i.e., the closest values to the critical thicknesses, are depicted in Fig. 3.31 for the highest occupied and lowest unoccupied subbands in

the vicinity of the Γ point in $\pm\Gamma X$ direction. In the case of both well materials the characteristic features are very similar, except that in α-Sn QWs, they are restricted to a much smaller area around the Γ point. For both, the highest occupied as well as the lowest unoccupied subband, the local magnetization (see Figs. 3.31) is mainly perpendicular to the interface normal and shows a rotation of π between the $-X \rightarrow \Gamma$ and the $\Gamma \rightarrow X$ direction. This switch between $-X \rightarrow \Gamma$ with a certain spin orientation and $\Gamma \rightarrow X$ with another one is a consequence of the time-reversal symmetry. The resulting spin polarization together with the linear dispersion of the underlying bands is a clear indication for the topological character of the states and gives rise to the quantum spin Hall effect. The fact that they are topologically protected will be demonstrated in Sec. 3.5.3 by their independence of the QW orientation for the HgTe case.

3.5.3 Electronic properties of HgTe/CdTe(110) and α-Sn/CdTe(110) QW structures

3.5.3.1 Electron and hole subbands

In the last section 3.5.2 it was shown, that in (001)-orientated α-Sn and HgTe quantum wells with CdTe as confining material, a critical thickness exists, where a topological transition from a trivial insulating phase into the QSH phase occurs. For both well materials, this transition is accompanied by the formation of helical edge states, that give rise to intrinsic spin currents. In the present section, quantum wells with (110) orientation are studied. Here, we focus on the changes in the electronic structures with respect to the (001) orientated QWs, which are caused by the different unit cell geometry. The arrangement of atoms in the two dimensional (110) unit cell is significantly different from that of the (001) one. This causes a break of the inversion symmetry in α-Sn QWs resulting in significant differences of the electronic properties of HgTe/CdTe(110) and α-Sn(110) superlattices.

The subband structures of three multi-QW structures are compared for α-Sn and HgTe QW films of varying thickness sandwiched between CdTe barriers in Fig. 3.32. There are several qualitative similarities but also quantitative discrepancies between the two different QW materials. All the superlattice systems represent insulators but with very different fundamental energy gaps varying in the range 0.01 to 0.1 eV. The presented subbands are mainly derived from α-Sn or HgTe states. In HgTe quantum wells the contributions from CdTe to the highest occupied and the lowest unoccupied subbands is small as indicated by the energetic overlap with the projected bulk valence band structure of CdTe in Fig. 3.32. The same holds for α-Sn QWs despite the large valence band discontinuity.

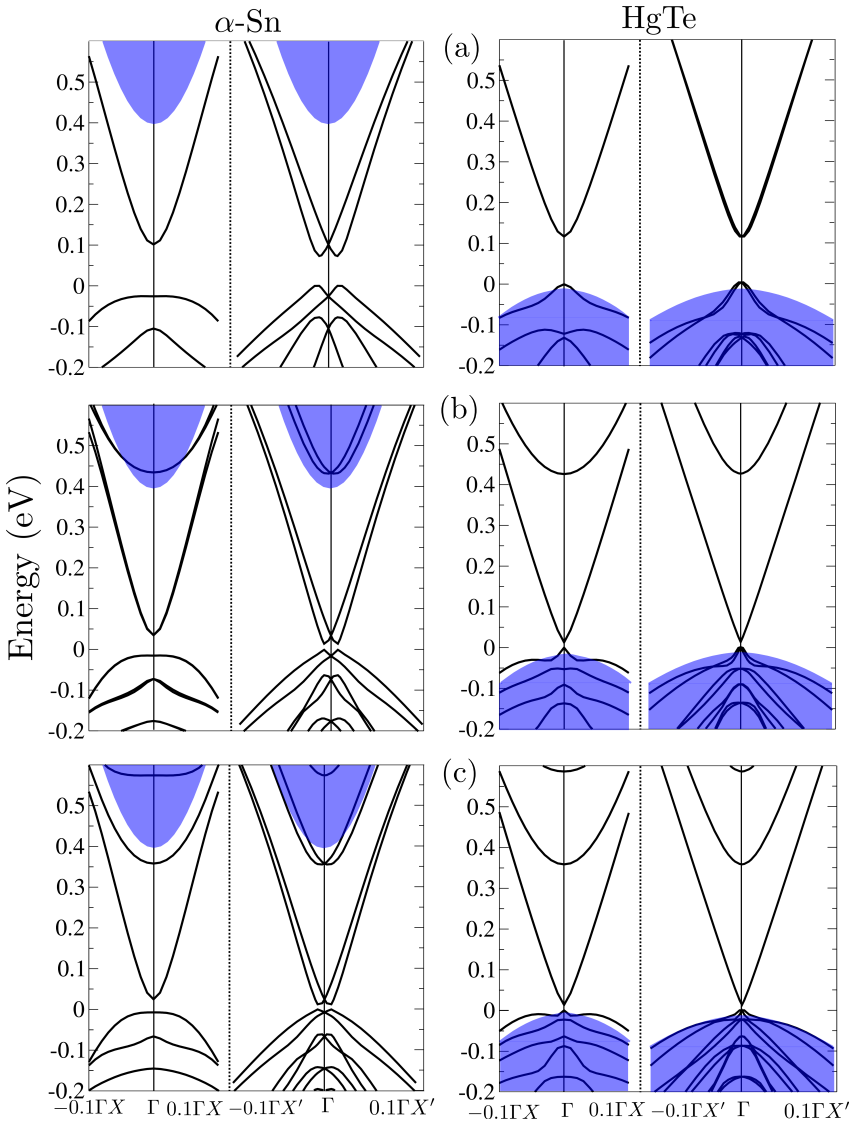

Figure 3.32: Subband structures of $(\alpha\text{-Sn})_N(\text{CdTe})_8(110)$ (left panels) and $(\text{HgTe})_N(\text{CdTe})_8(110)$ (right panels) superlattices for different QW thicknesses $N = 12$ (a), 20 (b), and 24 (c). The blue background indicates the projected bulk band structure of the CdTe barrier material. The energy of the highest occupied QW state is used as energy zero.

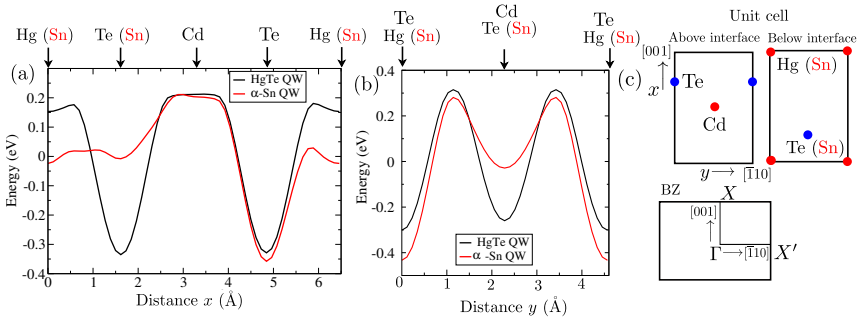

Figure 3.33: Plane-averaged local electrostatic potential for α-Sn and HgTe QWs along the x (a) and y (b) axis of the interface unit cell parallel to the interface. Only the potential of the atomic layers directly above and below the interface are taken into account. In addition, the geometry, positions of ions, high-symmetry directions and high-symmetry points of the interface unit cell and the corresponding BZ are illustrated in (c).

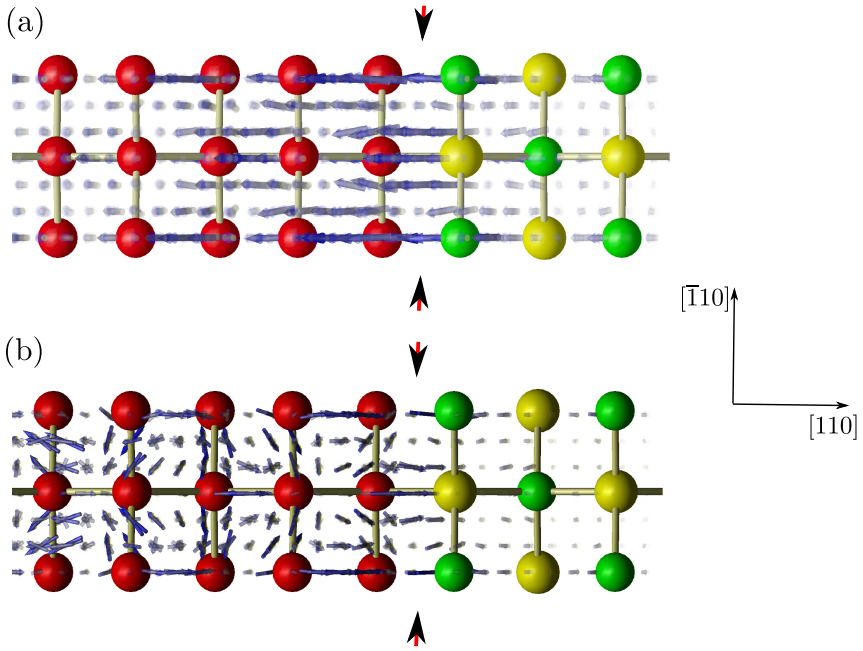

Figure 3.34: Local magnetization (blue arrows) of the highest occupied state (a) and the second highest occupied state (b) of a $(\alpha\text{-Sn})_{12}(\text{CdTe})_8$ QW in the vicinity of Γ in $\Gamma X'$ direction in the region of the interface. Blue spheres indicate tin atoms, and Cd (Te) atoms are depicted in red (yellow).

In contrast to the ΓX direction the subbands along $\Gamma X'$, i.e., parallel to $[\bar{1}10]$, show a **k**-vector-induced splitting of all s- and p-derived subbands mainly due to spin-orbit interaction. The reason is the reduced point-group symmetry of the (110)1×1 unit cell compared to the (001)$\sqrt{2} \times \sqrt{2}$ one [32]. Additionally, within α-Sn QWs with $N < 32$, several splittings are accompanied by a displacement of the two parabolas along $\Gamma X'$ or $-\Gamma X'$ away from the Γ point. It seems to be a clear consequence of a Rashba effect [109] as a consequence of the different electrostatic situation at the interface between CdTe and α-Sn compared to the HgTe/CdTe case. This is illustrated in Fig. 3.33. In the CdTe layer at the interface, one Te and one Cd atom are located at (0.5|0.5) (in units of the edge length) and (0.75|0) in the rectangular 1×1 interface unit cell (see Sec. 2.5.3), respectively in the surface unit cell. The coordinates (x|y) are illustrated in Fig 3.33 (c). In the case of HgTe as well material, with a HgTe layer nearest to the interface, the positions of Te (0.25|0.5) and Hg (0|0) atoms in combination with the atomic positions in the CdTe layer give rise to a mirror symmetrical electrostatic potential along the [001] (x) direction. This is clearly visible in Fig. 3.33(a). Along the $[\bar{1}10]$ (y) direction, two minima of the electrostatic potential caused by the Te atoms at $y = 0$ (inside the CdTe layer), and $y = 0.5$ (inside the HgTe layer) lead to a symmetric electrostatic potential as well. Consequently, in the case of HgTe(110) QWs embedded in CdTe(110) barriers, the electrostatic potential in the vicinity of the interface is symmetric in both high-symmetry directions of the surface unit cell as shown in Figs. 3.33 (a) and (b). Because of the (110) interface between two II-VI compounds with nearly equal bond ionicities [168] no electron transfer should occur perpendicular and parallel to the interface. Therefore, no asymmetry is visible in Figs. 3.33 (a) and (b). In the case of α-Sn QWs, however, the Te and Hg atoms at (0.25|0.5) and (0|0), respectively, are replaced by Sn atoms. The potential minimum caused by the Te atom inside the HgTe layer in HgTe QWs is not present. In order to fill the two resulting interface bonds Sn-Te and Sn-Cd with two electrons a transfer of half an electron is necessary between the two Sn dangling bonds of the α-Sn(110) surface pointing toward the CdTe(110) surface. In the spatial average this electron transfer gives rise to a dipole in [001] direction. Consequently, the deep potential minimum at the position of a Te atom in the HgTe surface does not anymore occur at the position of the corresponding Sn atom in the α-Sn QW case. Therefore, an asymmetric potential in [001] direction in the surface unit cell is formed as can be clearly seen in Fig. 3.33(a). Along the normal $[\bar{1}10]$ direction, the electrostatic potential is symmetric similar to the HgTe case (see Fig. 3.33(b)). The difference of the two minima along [001] creates an effective non-uniform electric field F_x in

[001] direction.

This resulting electric field causes the large splitting of subbands in $\Gamma X'$ direction parallel to $[\bar{1}10]$ in the α-Sn superlattices as well as the displacement of the subband extrema. Both effects can be explained with a simple Rashba spin-orbit Hamiltonian $H_{SO}^{\text{Rashba}} \propto (\mathbf{k} \times \mathbf{F}) \cdot \mathbf{s}$ with the spin operator $\mathbf{s}$ [109]. The electric field $\mathbf{F}$ has only an F_x component parallel to the [001] direction. The 2D Bloch wave vector $\mathbf{k}$ is pointed in y direction parallel to $[\bar{1}10]$, i.e., $\Gamma X'$. Consequently, if the spin has a component parallel to the interface normal the Rashba splitting effect occurs. For the opposite direction of $\mathbf{k}$ parallel to the x axis along [001] the Rashba coupling vanishes.

The local magnetization of the two highest occupied states of a $(\alpha\text{-Sn})_{12}(\text{CdTe})_8$ superlattice is depicted in Fig. 3.34 for a $\mathbf{k}$ point near Γ along $[\bar{1}10]$. For both states the spin has a strong component parallel to the interface normal. The spin orientations of the two displaced parabola are opposite to each other, the same holds for the other pairs of displaced parabolic subbands. Together with the localization of the corresponding wave functions at the interfaces and, hence, in the region of the electric field induced by the interface potential asymmetry, the occurring Rashba splittings are explained. For increasing QWs, however, the localization behavior of the states changes such that a larger fraction of the wave functions is located inside the QW. Consequently, the influence of the interface potential step and, hence, the Rashba splitting decreases as clearly demonstrated in Fig. 3.32. For QWs larger than 28 monolayers of α-Sn, no visible Rashba splitting is observed (not shown here).

Different confinements and $\mathbf{k}$-induced spin-orbit splittings of subbands in the α-Sn QWs compared to HgTe QWs significantly influence the topological transition versus the QW thickness. This is demonstrated in Fig. 3.35. It shows the contributions of atomic s and p orbitals to the lowest unoccupied, the highest occupied, and the second highest unoccupied subband at Γ depending on the QW thickness. In the case of HgTe quantum wells, a topological transition from a trivial insulator to a quantum-spin Hall phase occurs at a critical thickness of 46 Å [32]. Figure 3.35 shows that for QW thicknesses smaller than 12 double layers of HgTe, the lowest unoccupied subband at Γ is mainly formed by atomic s orbitals, while the highest occupied subband at Γ shows strong p contributions. As the s (p)-like subband can be identified with the $\Gamma_{6c}(2)$ ($\Gamma_{8v}(4)$)-level character of bulk zinc-blende or diamond structure crystals, the HgTe QWs with $d_1 < d_c$ show a band ordering which is similar to that of the trivial insulator CdTe. With increasing QW thickness, the energy of the s-derived subband is lowered, whereas the p-like subband is shifted toward higher energies. Consequently, at a critical thickness of $d_c = 4.6$ nm there

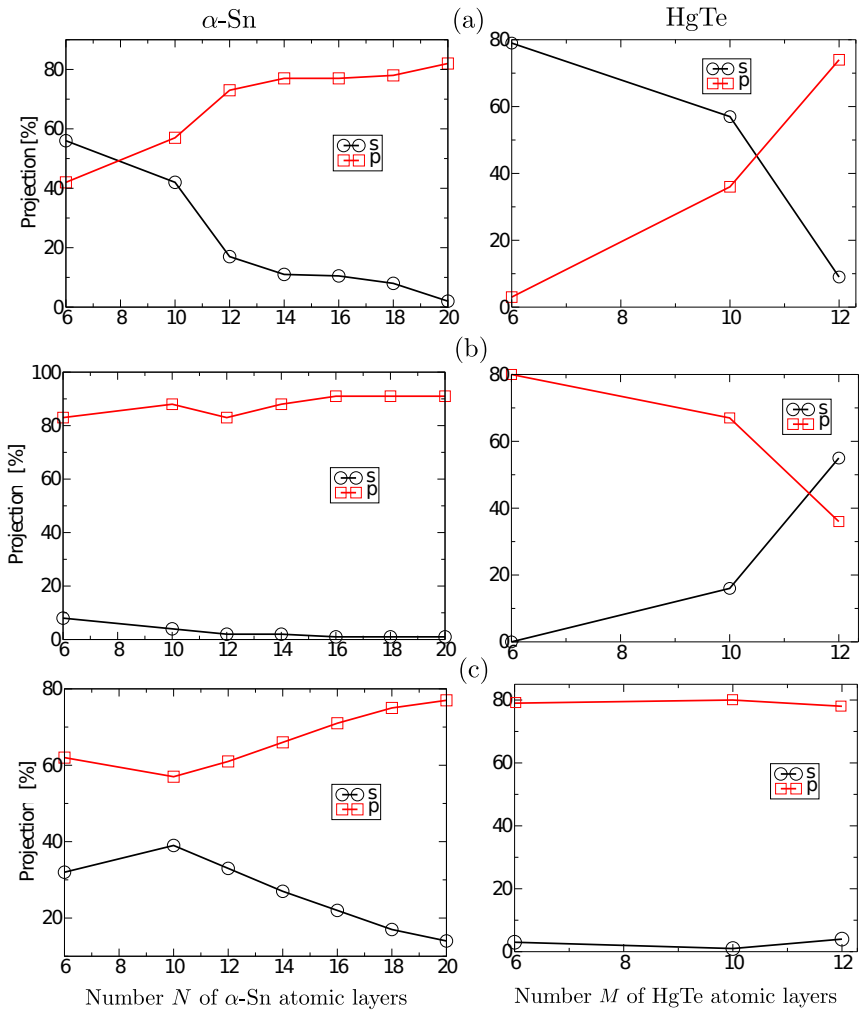

Figure 3.35: Contributions of atomic s- and p orbitals to the subband states close to the Fermi level of $(\alpha\text{-Sn})_N(\text{CdTe})_8(110)$ (left panels) and $(\text{HgTe})_M(\text{CdTe})_8(110)$ (right panels) superlattices depending on the QW size. In (a), the lowest unoccupied subband is depicted, while (b) refers to the highest occupied subband, and (c) shows the second highest occupied subband.

is a crossing of subbands and the level ordering is interchanged, which leads to an ordering $\Gamma_{6c} < \Gamma_{8v}$ similar to that of HgTe bulk. In Fig. 3.35 this transition can be understood by the symmetry change of the lowest unoccupied subband from s- to p-like which is accompanied by the inverse change of the highest occupied band from p- to s-character. This topological transition is identical to that observed in the HgTe (001) quantum wells, which has been discussed in the previous section 3.5.2. Moreover, the fact, that the edge states occur independently on the interface orientation is a clear indication for their topologically protected character.

In α-Sn QWs the situation is different. Figure 3.35 (left panels) indicates, that the lowest unoccupied subband behaves similarly to that of HgTe QWs. For $N = 12$, the lowest unoccupied subband shows nearly 60 % s contributions, the remaining 40 % are due to p orbitals (see Fig. 3.35(a)). With increasing thickness, the percentage of s character decreases rapidly while there is an increase in the portion of atomic p contributions. At a QW thickness of 14 (110) atomic layers of α-Sn, the ratio of p and s percentages is approximately 5:1. For even larger QWs, the atomic s orbital fraction becomes negligibly small and the band has a clear p character. The highest occupied subband, which is depicted in Fig. 3.35(b), is clearly p-derived for all QW sizes. Finally, the second highest occupied subband (see Fig. 3.35(c)) shows a similar behavior as the lowest unoccupied one, but the contribution of atomic s orbitals does not decrease as rapidly as in the case of the lowest unoccupied subband. This band with pronounced s character below the Fermi level might be related to the fact that the Γ_{6c} level of α-Sn is much closer to the valence band edge than that of HgTe in the HgTe QW case due to the significantly larger valence band discontinuity in α-Sn QWs. Even for the largest QWs studied, the second highest occupied subband shows 15 % s contributions. It can be summarized, that despite the fact that there is an interchange in the orbital character of the lowest unoccupied subbands similar to that in HgTe QWs, the corresponding symmetry modification in the highest occupied subband is not observed. Therefore, a topological transition with an inversion of the band ordering can be hardly identified. Minor contributions of atomic d orbitals are not shown in the figure. They result from bulk CdTe bands due to the large valence band discontinuity that has been discussed above.

To further investigate a possible interchange in the band ordering in the case of α-Sn QWs, the energetic positions of the three subband states closest to the Fermi level depending on the QW thickness are plotted in Fig. 3.36. It is obvious, that the fundamental energy gap decreases with increasing QW thickness from 119 meV (N=12) to 9 meV (N=20). This could be an indication that there might be a crossing of the highest occupied and the lowest unoccupied subband for even larger

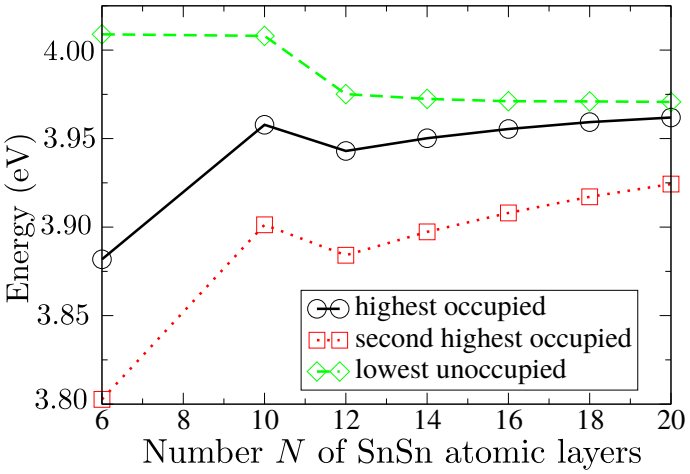

Figure 3.36: Energetic position of the highest occupied, second highest occupied, and lowest unoccupied subband at Γ depending on the QW thickness for α-Sn QWs embedded in CdTe. The average electrostatic potential is used to align the energy scales of the diffent $(\alpha\text{-Sn})_N(\text{CdTe})_8(110)$ QW structures.

QWs. However, as discussed above and shown in Fig. 3.35 (left panels), for large QWs, both levels are mainly formed by atomic p orbitals. A crossing would therefore not indicate an inversion of the band ordering. The decrease of the fundamental gap which is shown in Fig. 3.36 is therefore more likely caused by the decreasing spatial confinement due to the increased α-Sn layer. It can be concluded, that no indication for an interchange of the band ordering of Γ_{8v} and Γ_{6c} has been found in α-Sn(110) QWs embedded in CdTe barriers.

The assumption, that the bonding situation with resulting local potential anisotropy and non-uniform electric field inhibits the topological transition in α-Sn, can be further verified by the investigation of HgTe/InSb(110) multi-QW structures, where the barrier material CdTe is replaced by InSb, a III-V compound. The band structure of a $(\text{HgTe})_{20}(\text{InSb})_8(110)$ QW as depicted in Fig. 3.37(a), is very similar to that of a $(\alpha\text{-Sn})_{20}(\text{CdTe})_8(110)$ QW (left panel in Fig. 3.32 (b)) concerning the displacement of the band extrema away from Γ and the large subband splittings in $\Gamma X'$ direction. Therefore, it does not show the QSH effect like the $(\text{HgTe})_{20}(\text{CdTe})_8$ QW of the same size (see right panel in Fig. 3.32(b)). Consequently, the different bonding situation at the HgTe/InSb (II-VI compound - III-IV compound) interface compared to that of the CdTe/HgTe (II-VI compound - II-VI compound) interface in combination with the different confinement situation must be responsible for the drastic changes in the electronic subband structure of the superlattice. This can again be understood by an electron transfer between the interface Hg-Sb and Te-In interface bonds of about 0.25 electrons along [001]. The resulting asymmetry of the electrostatic potential in [001] direction in the interface region, which is shown in

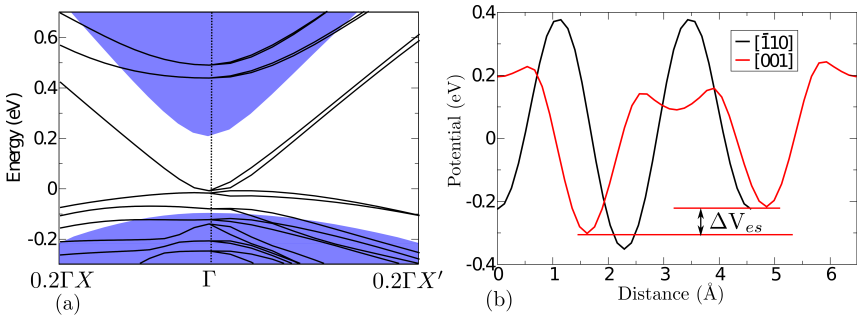

Figure 3.37: (a) Electronic band structure of a $(HgTe)_{10}(InSb)_4(110)$ QW. The blue background indicates the bulk band structure of InSb projected onto the interface BZ. (b) Local potential in the interface region of the same QW averaged over planes parallel to the interface normal in [001] (red line) and [$\bar{1}$10] direction (black line). The asymmetry of the electrostatic potential in [$\bar{1}$10] direction is indicated by the maximum potential difference ΔV_{es}.

Fig. 3.37(b), is similar to the situation at the α-Sn/CdTe interface. With regard to the interface electrostatics, the In and Sb atoms in the first atomic layer behave qualitatively similar to the two Sn atoms in the first atomic layer in the well film. In addition, as pointed out in Sec. 3.5.1, due to the small energetic difference between the HgTe Γ_{8v} level and the conduction band of InSb, the confinement situation of the HgTe/InSb(110) QW is similar to that of α-Sn/CdTe QWs and differs from that of the HgTe/CdTe(110) structures. Consequently, the electronic structure of InSb/HgTe QWs shows a behavior analogous to α-Sn/CdTe superlattices. There is only a quantitative difference due to the different net electron transfers along [001].

3.5.3.2 Edge states

In order to investigate the topological character of (110) QWs, Fig. 3.38(a) shows the subband dispersion around Γ along $-X \rightarrow \Gamma \rightarrow X$ for the highest occupied and the lowest empty states together with their wave functions and their local spin orientations at Γ for the HgTe QW structure with $d = 4.8$ nm, i.e., the closest value to the critical thickness (for its band structure see Fig. 3.32(b)). The linear band dispersion, especially for the empty subband, is underlined. The linearity is quickly modified away from Γ. From the Γ-point wave-function squares in Fig. 3.38 (b) it is obvious, that the highest occupied and lowest empty states are mainly located inside the HgTe layer. The atomic oscillations are clearly visible. Their envelopes however demonstrate the edge character. The maximum probability to find an electron is mainly localized at the HgTe-CdTe interfaces, i.e., at the edges of the QW and decays exponentially into the HgTe layer, while the probability in the barrier layers is small, in particular for the hole state. The two edges belong

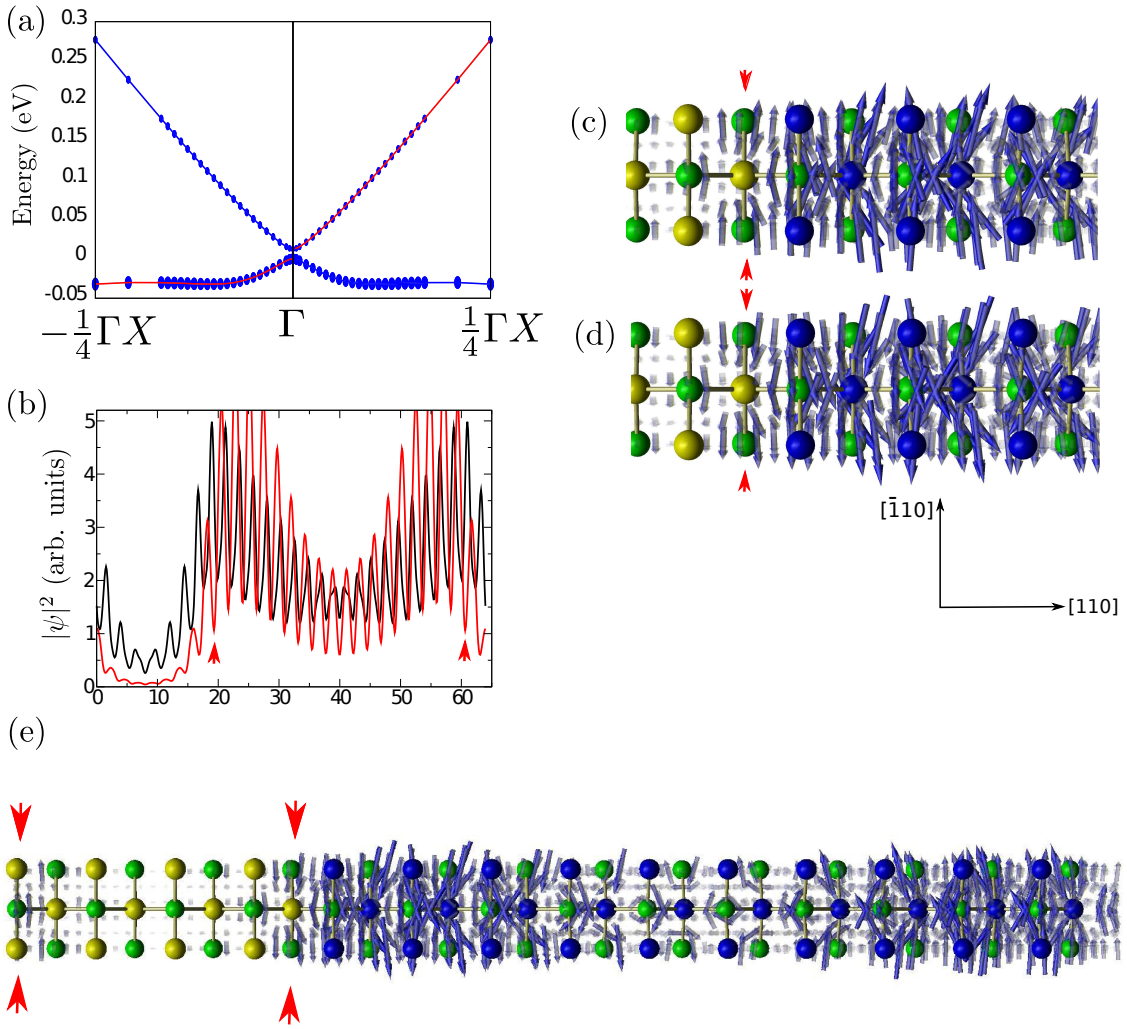

Figure 3.38: Characteristic edge state properties in the case of the $(HgTe)_{20}(InSb)_8(110)$ QW: (a) Dispersion of the highest occupied and lowest unoccupied subbands around Γ. The size of the blue dots indicates the atomic *p*-contributions. The larger a dot, the higher the projection onto atomic *p*-orbitals. The energy of the highest occupied state is used as energy zero. The colors of the bands, red or blue, indicate the direction of the local magnetization, the spin density, inside the rectangular surface BZ. (b) Wave-function square of the lowest unoccupied (black) and highest occupied states at Γ averaged over planes perpendicular to the QW orientation [110] as a function of the distance. A local magnetization with a large projection onto the [100] direction is depicted in red, while a blue color means a magnetization in opposite direction. A view along a (001) plane of the local magnetization of the lowest unoccupied state in both cases is shown in (c) and (d). The spin polarization inside the whole supercell of the lowest unoccupied state near Γ is depicted in panel (e). Red arrows indicate the position of the interfaces.

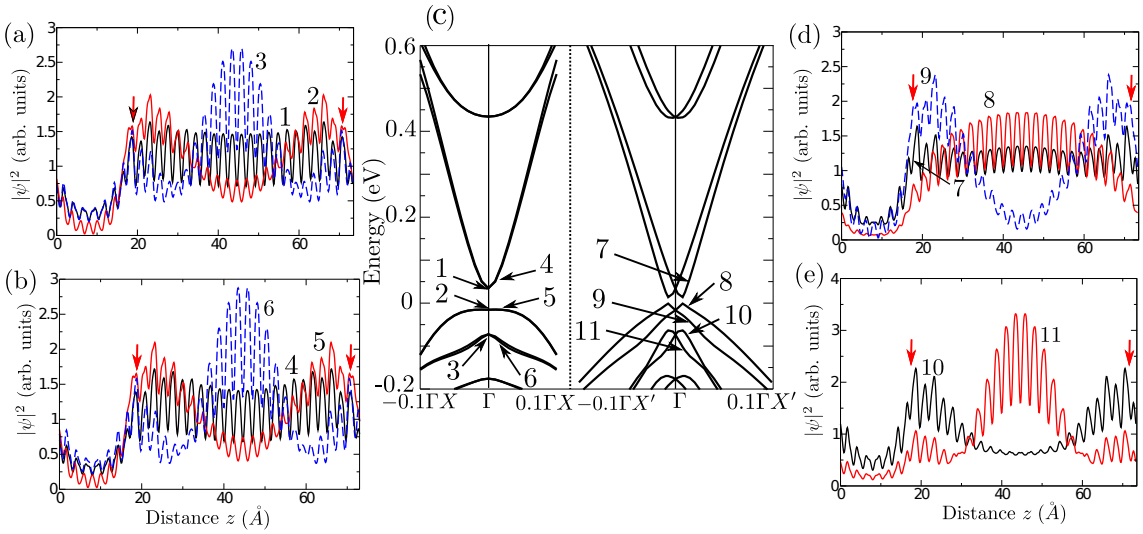

Figure 3.39: Band structure of the $(\alpha\text{-Sn})_{20}(\text{CdTe})_8(110)$ superlattice. The panels around the band structure plot show the wave functions averaged over the (110) plane of the states that are marked by numbers. The energy of the highest occupied states is used as energy zero. The red arrows indicate the positions of the interfaces.

to different spin orientations, which, however are influenced by the vector character of the spin (for demonstration see Figs. 3.38(c), (d), and (e)), because of the used non-collinear treatment, and the different contributions of anions and cations. The helical character is also clearly visible. Moreover, the local spin orientation (see Figs. 3.38 (c), (d), and (e)) shows a rotation of π of the spin polarization between the $-X \rightarrow \Gamma$ and the $\Gamma \rightarrow X$ direction, similar to the (001) case. This behavior is indicated by the colors of the bands in Fig. 3.38 (a). From Fig. 3.38 (e) it is obvious, that the lowest unoccupied state near Γ shows opposite spin orientations at the two edges. Therefore, the topological interface states occur in (001) and (110) orientated QWs indicating that these states are independent of the QW orientation, which is a clear indication that they are topologically protected, as can be expected from the strong 3D TI nature of HgTe bulk (see Sec. 3.2).

The state properties of the lowest empty and highest occupied subbands in the case of α-Sn QWs are depicted in Fig. 3.32. For one example $(\alpha\text{-Sn})_{20}(\text{CdTe})_8(110)$ we study the wave functions at Γ but also at shifted position $(0, 0.01)$ (in units of the reciprocal lattice) in the surface BZ, at which the extrema of the subbands occur and in [100] direction at $(0.01, 0)$ in which the subband splitting is negligibly small. The wave-function squares in Fig. 3.39(a) show the characteristic atomic oscillations. Most interesting are however the envelopes of these functions because they directly describe their localization behavior.

At Γ, the lowest empty subband and the highest occupied one are localized in the

QW material. They clearly indicate maxima of the probability density close to the interfaces with a relatively slow decay into the QW material. Therefore, both states show an important property of edge states, their localization near the interfaces. The second highest occupied band is localized in the center of the α-Sn material and can be identified with a lowest $n = 1$ confined state as occurs in a rectangular potential well. The localization of the envelope functions of these three subband states closest to the Fermi level does not change at $(0.01, 0)$ in the vicinity of Γ in [001] direction where the twofold degeneracy of the subbands is not lifted (see Fig. 3.39(b)).

The situation does completely change in the $[\bar{1}10]$ direction of the interface BZ, where the large subband splittings due to the local electric field in the interface plane via the Rashba effect occur as depicted in Figs. 3.39 (d) and (e). The envelope functions (Figs. 3.39 (d) and (e)) show, that the lowest unoccupied band still exhibits a slightly elevated probability density at the interface while the decay inside the α-Sn layer is very small. Most interesting is the behavior of the four highest occupied bands. In $\Gamma X'$ direction, each pair splits into an upper state that is localized at the interfaces and decays inside the α-Sn layer, and a lower one that is similar to a n=1 confined state due to Rashba splitting as explained in the previous section.

The QSH phase, that occurs in HgTe QWs, is not present in the case of α-Sn QWs, because the subband states, that are localized at the interface, do not possess the characteristic spin polarization perpendicular to the interface normal. In fact, as shown in Fig. 3.34, the subband states possess a spin orientation parallel to the interface normal, which leads to the Rashba splitting of states in $[\bar{1}10]$ direction as discussed above. In the opposite direction [001] without subband splitting, Kramers degeneracy of these states occurs. The interface states are therefore not anymore chiral edge states that could lead to spin currents.

4 Summary and Conclusions

In this thesis, results of *ab-initio* and tight-binding calculations for structural, energetic, electronic, and topological properties of α-tin and HgTe bulk, α-Sn nanocrystals, α-Sn(001) surfaces, and α-Sn/CdTe and HgTe/CdTe quantum well structures are presented. The spin-orbit interaction is taken into account.

A comparison of different approximations of the XC energy for the bulk systems turned out that hybrid functional calculations including a fraction of the non-local Fock exchange give very reliable electronic structure results. This holds in comparison with experimental data but also quasiparticle calculations in the framework of the GW approximation. However, the applicability of hybrid functionals is restricted to small systems due to the required computational effort because of the non-local treatment. To overcome the limitations in computational cost, approximate methods are needed. One is the meta-DFT, e.g. the modified Becke-Johnson method, which uses a parametric model function to reproduce the shape of the non-local exchange energy. The MBJLDA yields reasonable band-structure results in comparison with hybrid functional calculations combined with low computational cost, which allows for the treatment of large systems containing more than 100 atoms. However, it cannot be applied to systems containing vacuum, such as NCs and surfaces. To investigate system sizes, which are too large to be treated within an *ab-initio* description, a tight-binding model including nearest-neighbor spin-orbit interaction was additionally developed. Therefore, it was appropriate to treat quantum well structures within the MBJLDA method, while hybrid functional calculations could be performed in the case of small NCs and surfaces modeled by thin slabs. However, for systems consisting of several hundreds of atoms, local XC functionals or the ETBM were applied.

To calculate the topological invariants of 3D systems, especially strained and unstrained α-Sn and HgTe, a numerical method suggested by Yu et al. has been implemented in the VASP code. It is based on the Wannier charge center evolution and does not require any gauge fixing, which makes its application to wave functions obtained by *ab-initio* calculations possible. By means of this method, α-Sn and HgTe were shown to be three-dimensional topological insulators, while CdTe and InSb are found to be topologically trivial.

Comparing the electronic level ordering of the bulk α-Sn to those of the NCs, an

inversion in the ordering of the Γ_{8v} and Γ_{6c} states is found. Calculating the size dependence of the HOMO-LUMO gaps, we found a decreasing spatial confinement causing a decrease of the gaps with rising diameter. Consequently, a topological transition, where the level ordering changes for a certain NC size, is predicted. Fitting the diameter dependence of the energetic position of HOMO and LUMO states in DFT-LDA, we determine the NC diameter for the topological transition to be approximately 11.5 nm, which fits quite well to the result 12.7 nm obtained from the calculations in tight-binding approximation. The lowest two-particle excitation energies have been studied within different approximations for the electron-electron interaction, in order to distinguish between quasiparticle and optical gap. We found, that there is an almost cancellation of quasiparticle and excitonic effects, which is in agreement to previous calculations for NCs made for other materials. Consequently, the differences of Kohn-Sham eigenvalues for HOMO and LUMO already give a reasonable description of the optical gaps. Calculating the absorption spectra of all NCs we have shown, that the gap decreases with rising NC size leading to a redshift of the absorption spectra, which allows to tune the optical properties by the NC diameter. The resulting absorption edges cover a wide energy range from the infrared region of the electromagnetic spectrum up to the UV. This might offer possibilities for future applications in optoelectronic devices with varying characteristic wavelength. The radiative decay times are of the order of 0.1 ns, which make the α-Sn NCs with diameters larger than 2 nm to suitable nanostructures for light-emitting devices in the infrared spectral region.

The electronic properties of slightly strained α-Sn(001) films are investigated by *ab-initio* and tight-binding methods. The strain models the growth of α-Sn on a slightly lattice-mismatched material such as InSb or CdTe. For film thicknesses in the order of 4-5 nm, we found the formation of upper and lower Dirac cones formed by a pair of helical edge states as predicted by model studies in the literature. However, there are also significant discrepancies to the conventional picture of a 3D topological insulator. First of all the Dirac cones do not appear in the gap between the Γ_{8v} states opened by biaxial strain. Rather, the linear bands appear mainly between heavy-hole-like Γ_{8v} and electron-like Γ_{6c} bulk-derived bands in agreement with experimental observations. This means, that the TSSs appear inside a bulk gap, but not inside a gap between occupied and unoccupied bands but the negative $\Gamma_{8v} - \Gamma_{6c}$ bulk *sp* band gap. The influence of a strain-induced fundamental gap therefore seems to be negligible. For smaller slab thicknesses the situation is more complex. A gap between the Dirac cones may be opened due to confinement effects for small slab size. The Dirac cones observed by ARPES under surface-sensitive

conditions are explained by pieces of slab subbands with linear dispersion. The resulting Fermi velocity agrees with the measured values. Since the Dirac points are below the Fermi level, it will be difficult to observe spin currents at the surface and, therefore, a quantum spin Hall phase for as-grown samples. However, a shift of the Fermi level toward larger binding energies by gate voltages, doping or band bending may bring the Dirac point close to it. Such manipulations indicate a promising potential to demonstrate new physical effects for α-Sn films of varying thickness and varying Fermi level position.

We have applied the approximate quasiparticle MBJLDA method including spin-orbit interaction to study the size-dependent properties of α-Sn and HgTe quantum wells embedded in CdTe. Especially a possible quantum phase transition along the thickness and the carrier confinement as well as the occurrence of edge states depending on the well material and the QW orientation were investigated. Two growth directions, [001] and [110], have been studied. Furthermore, test calculations of HgTe QWs with InSb as barrier material were performed. In the case of [001] orientated interfaces, the resulting subband structures vary significantly with the QW thickness, although they are mainly derived by HgTe states, at least for energies close to and above the Fermi level. In the case of HgTe as well material, the predictions made by $\mathbf{k} \cdot \mathbf{p}$ theory and their experimental proof are qualitatively verified. A topological transition from a trivial insulator with normal band ordering for small thicknesses $d_1 < d_c$ to the quantum spin-Hall phase for $d_1 > d_c$ is confirmed. It approximately occurs for critical QW thicknesses $d_c \approx 4.6$ nm. The QSH phase is characterized by the existence of edge states with linear dispersion, that bridge the fundamental gap. They are localized in the HgTe layers near the interfaces and decay exponentially into the QW. The edge states show a clear spin polarization parallel to the interface indicating their possible contribution to spin currents near the edges. α-Sn/CdTe(001) interfaces are found to behave similarly to the HgTe case. The topological transition occurs at larger diameters $d_c = 8.5$ nm than in the HgTe case and the extension of the edge states is restricted to a much smaller interval around the Γ-point. This is likely to be caused by differences in the interface electrostatics. At the α-Sn/CdTe(001) interface, the valence Γ_{8v} level is much closer to the conduction band edge of CdTe than in the HgTe/CdTe(001) interface leading to different confinement situations.

In the case of HgTe/CdTe(110), the picture is very similar to the (001) case, which underlines the characteristic topological protection of the edge states against changes in surface or interface orientation and termination for strong topological insulators. However, in the α-Sn case the interpretation of the electronic structure

and, therefore, of the topological states is much more complicated. The main reason is the occurrence of an asymmetric electrostatic potential at the α-Sn/CdTe(110) interface in [001] direction. The accompanying electric field represents an additional symmetry break, which significantly influences the edge states. The most striking effect is, however, the **k**-induced splitting and, for many subbands, the displacement of band extrema together with a spin polarization parallel to the interface normal for **k** vectors parallel to $[\bar{1}10]$. Therefore, these phenomena can be subsumized as consequences of a Rashba effect due to an asymmetric electrostatic potential in the interface region. This was further verified by the calculation of the electronic structure of HgTe/InSb(110) QWs that show similar electrostatic interface properties as α-Sn/CdTe(110) QWs and, consequently, possess very similar electronic subband structures.

It can be summarized, that the investigation of the topological properties, especially the QSH effect and its relation to real-structure effects of semiconductors, yields extremely exciting results. However, it opens a wide field for further research. A first issue could be the investigation of the evolution of electronic states located at the surface of NCs for increasing NC size. They can be expected to evolve into topological surface states, when the density of states of the NC converges toward the bulk DOS and, hence, the NC behaves electronically similar to the topologically non-trivial bulk substrate. Here, in addition to the α-Sn NCs, a comparison to the electronic properties of HgTe clusters would be of great interest. The same holds for a possible investigation of the electronic properties HgTe surfaces. The occurrence of TSSs can be expected due to the non-trivial topology of HgTe bulk. However, in contrast to α-Sn surfaces, the ionic bond character is likely to significantly influence the results depending on surface orientation and termination. Even in the case of α-Sn surfaces, open questions remain. They concern the dependence of the TSSs on the surface orientation, since only the (001) surface has been studied in the framework of this thesis. Moreover, the occurrence of the TSS in α-Sn(001) surfaces below the Fermi energy makes the influence of doping an interesting subject. Experimental studies suggest, that doping could lower the Fermi level in such a way, that the TSSs become depleted, possibly providing the necessary conditions for the QSH effect. In the case of QW structures, the influence of the barrier material and the barrier thickness on the topological transition between the trivial insulating phase and the QSH phase are a promising subject for further investigation.

Bibliography

[1] I. Tsidilkowski. *Gapless Semiconductors - a New Class of Materials*. Berlin: Akademie-Verlag, 1988.

[2] J. R. Chelikowsky and M. L. Cohen. "Nonlocal pseudopotential calculations for the electronic structure of eleven diamond and zinc-blende semiconductors". In: *Phys. Rev. B* 14 (2 1976), pp. 556–582. DOI: 10.1103/PhysRevB.14.556. URL: http://link.aps.org/doi/10.1103/PhysRevB.14.556.

[3] L. Fu and C. L. Kane. "Topological insulators with inversion symmetry". In: *Phys. Rev. B* 76 (4 2007), p. 045302. DOI: 10.1103/PhysRevB.76.045302. URL: http://link.aps.org/doi/10.1103/PhysRevB.76.045302.

[4] C. L. Kane and E. J. Mele. "Z_2 Topological Order and the Quantum Spin Hall Effect". In: *Phys. Rev. Lett.* 95 (14 2005), p. 146802. DOI: 10.1103/PhysRevLett.95.146802. URL: http://link.aps.org/doi/10.1103/PhysRevLett.95.146802.

[5] B. Andrei Bernevig, T. L. Hughes, and S.-C. Zhang. "Quantum Spin Hall Effect and Topological Phase Transition in HgTe Quantum Wells". In: *Science* 314 (2006), pp. 1757–1761. DOI: 10.1126/science.1133734.

[6] L. Fu, C. L. Kane, and E. J. Mele. "Topological Insulators in Three Dimensions". In: *Phys. Rev. Lett.* 98 (10 2007), p. 106803. DOI: 10.1103/PhysRevLett.98.106803. URL: http://link.aps.org/doi/10.1103/PhysRevLett.98.106803.

[7] M. König et al. "Quantum Spin Hall Insulator State in HgTe Quantum Wells". In: *Science* 318 (2007), p. 766. DOI: 10.1126/science.1148047.

[8] C. Liu et al. "Quantum Spin Hall Effect in Inverted Type-II Semiconductors". In: *Phys. Rev. Lett.* 100 (23 2008), p. 236601. DOI: 10.1103/PhysRevLett.100.236601. URL: http://link.aps.org/doi/10.1103/PhysRevLett.100.236601.

[9] J. Moore. "Topological insulators: The next generation". In: *Nat Phys* 5.6 (June 2009), pp. 378–380. ISSN: 1745-2473. URL: http://dx.doi.org/10.1038/nphys1294.

[10] M. Z. Hasan and C. L. Kane. "Colloquium: Topological insulators". In: *Rev. Mod. Phys.* 82 (4 2010), pp. 3045–3067. DOI: 10.1103/RevModPhys.82.3045. URL: http://link.aps.org/doi/10.1103/RevModPhys.82.3045.

[11] S. Murakami, N. Nagaosa, and S.-C. Zhang. "Spin-Hall Insulator". In: *Phys. Rev. Lett.* 93 (15 2004), p. 156804. DOI: 10.1103/PhysRevLett.93.156804. URL: http://link.aps.org/doi/10.1103/PhysRevLett.93.156804.

[12] A. Alivisatos. "Semiconductor clusters, nanocrystals, and quantum dots". In: *Science* 271.5251 (1996), pp. 933–937. DOI: 10.1126/science.271.5251.933.

[13] T. Martin. "Shells of atoms". In: *Physics Reports* 273.4 (1996), pp. 199 –241. DOI: 10.1016/0370-1573(95)00083-6. URL: http://www.sciencedirect.com/science/article/pii/0370157395000836.

[14] R. V. S. Jensen, T. Garm Pedersen, and K. Pedersen. "Optical properties and size/shape dependence of α-Sn nanocrystals by tight binding". In: *physica status solidi (c)* 8.3 (2011), pp. 1002–1005. ISSN: 1610-1642. DOI: 10.1002/pssc.201000397. URL: http://dx.doi.org/10.1002/pssc.201000397.

[15] A. Rogach et al. "Colloidally Prepared HgTe Nanocrystals with Strong Room-Temperature Infrared Luminescence". In: *Advanced Materials* 11.7 (1999), pp. 552–555. ISSN: 1521-4095. DOI: 10.1002/(SICI)1521-4095(199905)11:7<552::AID-ADMA552>3.0.CO;2-Q. URL: http://dx.doi.org/10.1002/(SICI)1521-4095(199905)11:7<552::AID-ADMA552>3.0.CO;2-Q.

[16] M. V. Kovalenko et al. "Colloidal HgTe Nanocrystals with Widely Tunable Narrow Band Gap Energies: From Telecommunications to Molecular Vibrations". In: *Journal of the American Chemical Society* 128.11 (2006). PMID: 16536514, pp. 3516–3517. DOI: 10.1021/ja058440j. eprint: http://pubs.acs.org/doi/pdf/10.1021/ja058440j. URL: http://pubs.acs.org/doi/abs/10.1021/ja058440j.

[17] C. Wang et al. "Enhanced infrared emission from colloidal HgTe nanocrystal quantum dots on silicon-on-insulator photonic crystals". In: *Applied Physics Letters* 95.5, 053107 (2009), p. 053107. DOI: 10.1063/1.3194151. URL: http://link.aip.org/link/?APL/95/053107/1.

[18] S. Keuleyan et al. "Mid-infrared HgTe colloidal quantum dot photodetectors". In: *Nat Photon* 5 (2011), pp. 489–493. DOI: 10.1038/nphoton.2011.142. URL: http://dx.doi.org/10.1038/nphoton.2011.142.

[19] M. F. Fyhn et al. "α-Sn and β-Sn precipitates in annealed epitaxial $Si_{0.95}Sn_{0.05}$". In: *Phys. Rev. B* 60 (8 1999), pp. 5770–5777. DOI: 10.1103/PhysRevB.60.5770. URL: http://link.aps.org/doi/10.1103/PhysRevB.60.5770.

[20] I. Arslan et al. "Embedded Nanostructures Revealed in Three Dimensions". In: *Science* 309 (2005), p. 2195. DOI: 10.1126/science.1116745.

[21] R. Ragan and H. Atwater. "Diamond cubic Sn-rich nanocrystals: synthesis, microstructure and optical properties". English. In: *Applied Physics A* 80 (6 2005), pp. 1335–1338. ISSN: 0947-8396. DOI: 10.1007/s00339-004-3163-3. URL: http://dx.doi.org/10.1007/s00339-004-3163-3.

[22] Y. Lei et al. "Void-mediated formation of Sn quantum dots in a Si matrix". In: *Applied Physics Letters* 82.24 (2003), pp. 4262–4264. DOI: 10.1063/1.1584073. URL: http://link.aip.org/link/?APL/82/4262/1.

[23] A. Barfuss et al. "Elemental Topological Insulator with Tunable Fermi Level: Strained α-Sn on InSb(001)". In: *Phys. Rev. Lett.* 111 (15 2013), p. 157205. DOI: 10.1103/PhysRevLett.111.157205. URL: http://link.aps.org/doi/10.1103/PhysRevLett.111.157205.

[24] Y. Ohtsubo et al. "Dirac Cone with Helical Spin Polarization in Ultrathin α-Sn(001) Films". In: *Phys. Rev. Lett.* 111 (21 2013), p. 216401. DOI: 10.1103/PhysRevLett.111.216401. URL: http://link.aps.org/doi/10.1103/PhysRevLett.111.216401.

[25] X.-L. Qi and S.-C. Zhang. "Topological insulators and superconductors". In: *Rev. Mod. Phys.* 83 (4 2011), pp. 1057–1110. DOI: 10.1103/RevModPhys.83.1057. URL: http://link.aps.org/doi/10.1103/RevModPhys.83.1057.

[26] A. Roth et al. "Nonlocal Transport in the Quantum Spin Hall State". In: *Science* 325.5938 (2009), pp. 294–297. DOI: 10.1126/science.1174736. eprint: http://www.sciencemag.org/content/325/5938/294.full.pdf. URL: http://www.sciencemag.org/content/325/5938/294.abstract.

[27] F. Tran and P. Blaha. "Accurate Band Gaps of Semiconductors and Insulators with a Semilocal Exchange-Correlation Potential". In: *Phys. Rev. Lett.* 102 (22 2009), p. 226401. DOI: 10.1103/PhysRevLett.102.226401. URL: http://link.aps.org/doi/10.1103/PhysRevLett.102.226401.

[28] J. Heyd, G. E. Scuseria, and M. Ernzerhof. "Hybrid functionals based on a screened Coulomb potential". In: *J. Chem. Phys.* 118 (2003), p. 8207. DOI: 10.1063/1.1564060.

[29] O. Gunnarsson and B. I. Lundqvist. "Exchange and correlation in atoms, molecules, and solids by the spin-density-functional formalism". In: *Phys. Rev. B* 13.10 (1976), p. 4274. DOI: 10.1103/PhysRevB.13.4274. URL: http://link.aps.org/doi/10.1103/PhysRevB.13.4274.

[30] S. Küfner et al. "Structural and electronic properties of α-tin nanocrystals from first principles". In: *Phys. Rev. B* 87 (23 2013), p. 235307. DOI: 10.1103/PhysRevB.87.235307. URL: http://link.aps.org/doi/10.1103/PhysRevB.87.235307.

[31] S. Küfner et al. "Optical absorption and emission of α-Sn nanocrystals from first principles". In: *Nanotechnology* 24.40 (2013), p. 405702. URL: http://stacks.iop.org/0957-4484/24/i=40/a=405702.

[32] S. Küfner and F. Bechstedt. "Topological transition and edge states in HgTe quantum wells from first principles". In: *Phys. Rev. B* 89 (19 2014), p. 195312. DOI: 10.1103/PhysRevB.89.195312. URL: http://link.aps.org/doi/10.1103/PhysRevB.89.195312.

[33] S. Küfner, M. Fitzner, and F. Bechstedt. "Topological α-Sn surface states versus film thickness and strain". In: *Phys. Rev. B* 90 (12 2014), p. 125312. DOI: 10.1103/PhysRevB.90.125312. URL: http://link.aps.org/doi/10.1103/PhysRevB.90.125312.

[34] S. Küfner and F. Bechstedt. "Topological states in α-Sn and HgTe quantum wells: A comparison of *ab initio* results". In: *Phys. Rev. B* 91 (3 2015), p. 035311. DOI: 10.1103/PhysRevB.91.035311. URL: http://link.aps.org/doi/10.1103/PhysRevB.91.035311.

[35] M. Born and R. Oppenheimer. "Zur Quantentheorie der Molekeln". In: *Annalen der Physik* 389.20 (1927), pp. 457–484. ISSN: 1521-3889. DOI: 10.1002/andp.19273892002. URL: http://dx.doi.org/10.1002/andp.19273892002.

[36] W. Nolting. *Grundkurs Theoretische Physik: Vielteilchentheorie.* Vol. 2. Jena: Springer-Verlag, 2005.

[37] F. Bechstedt. "Austausch und Korrelation in Festkörpern". Vorlesungsscript. Friedrich Schiller Universität Jena, 2010.

[38] P. Hohenberg and W. Kohn. "Inhomogeneous Electron Gas". In: *Phys. Rev.* 136.3B (Nov. 1964), B864–B871. DOI: 10.1103/PhysRev.136.B864.

[39] U. von Barth and L Hedin. "A local exchange-correlation potential for the spin polarized case." In: *Journal of Physics C: Solid State Physics* 5.13 (1972), p. 1629. URL: http://stacks.iop.org/0022-3719/5/i=13/a=012.

[40] W. Kohn and L. J. Sham. "Self-Consistent Equations Including Exchange and Correlation Effects". In: *Phys. Rev.* 140.4A (Nov. 1965), A1133–A1138. DOI: 10.1103/PhysRev.140.A1133.

[41] V. Fock. "Näherungsmethode zur Lösung des quantenmechanischen Mehrkörperproblems". German. In: *Zeitschrift für Physik* 61.1-2 (1930), pp. 126–148. ISSN: 0044-3328. DOI: 10.1007/BF01340294. URL: http://dx.doi.org/10.1007/BF01340294.

[42] J. Slater. *The self-consistent field for molecules and solids*. Quantum theory of molecules and solids Bd. 4. McGraw-Hill, 1974. ISBN: 9780070580381. URL: http://books.google.de/books?id=RXYfAQAAMAAJ.

[43] D. Hobbs, G. Kresse, and J. Hafner. "Fully unconstrained noncollinear magnetism within the projector augmented-wave method". In: *Phys. Rev. B* 62.17 (Nov. 2000), pp. 11556–11570. DOI: 10.1103/PhysRevB.62.11556.

[44] J. P. Perdew and A. Zunger. "Self-interaction correction to density-functional approximations for many-electron systems". In: *Phys. Rev. B* 23.10 (1981), pp. 5048–5079. DOI: 10.1103/PhysRevB.23.5048.

[45] R. Dreizler and G. E.K.U. *Density functional theory*. Springer-Verlag, 1990.

[46] D. M. Ceperley and B. J. Alder. "Ground State of the Electron Gas by a Stochastic Method". In: *Phys. Rev. Lett.* 45.7 (Aug. 1980), pp. 566–569. DOI: 10.1103/PhysRevLett.45.566.

[47] M. Gell-Mann and K. A. Brueckner. "Correlation Energy of an Electron Gas at High Density". In: *Phys. Rev.* 106 (2 1957), pp. 364–368. DOI: 10.1103/PhysRev.106.364. URL: http://link.aps.org/doi/10.1103/PhysRev.106.364.

[48] R. M. Martin. *Electronic Structure: Basic Theory and Practical Methods*. Cambridge University Press, 2004.

[49] W. G. Aulbur, L. Jönsson, and J. W. Wilkins. "Quasiparticle Calculations in Solids". In: *Solid State Physics*. Ed. by H. Ehrenreich and F. Saepen. Vol. 54. Solid State Physics. Academic Press, 1999, pp. 1 –218. DOI: 10.1016/S0081-1947(08)60248-9. URL: http://www.sciencedirect.com/science/article/pii/S0081194708602489.

[50] J. P. Perdew and W. Yue. "Accurate and simple density functional for the electronic exchange energy: Generalized gradient approximation". In: *Phys. Rev. B* 33 (12 1986), pp. 8800–8802. DOI: 10.1103/PhysRevB.33.8800. URL: http://link.aps.org/doi/10.1103/PhysRevB.33.8800.

[51] J. P. Perdew et al. "Atoms, molecules, solids, and surfaces: Applications of the generalized gradient approximation for exchange and correlation". In: *Phys. Rev. B* 46 (11 1992), pp. 6671–6687. DOI: 10.1103/PhysRevB.46.6671. URL: http://link.aps.org/doi/10.1103/PhysRevB.46.6671.

[52] J. P. Perdew, K. Burke, and M. Ernzerhof. "Generalized Gradient Approximation Made Simple". In: *Phys. Rev. Lett.* 77.18 (Oct. 1996), pp. 3865–3868. DOI: 10.1103/PhysRevLett.77.3865.

[53] C. Filippi, D. J. Singh, and C. J. Umrigar. "All-electron local-density and generalized-gradient calculations of the structural properties of semiconductors". In: *Phys. Rev. B* 50 (20 1994), pp. 14947–14951. DOI: 10.1103/PhysRevB.50.14947. URL: http://link.aps.org/doi/10.1103/PhysRevB.50.14947.

[54] A. D. Becke. "A new mixing of Hartree-Fock and local density-functional theories". In: *Journal of Chemical Physics* 98.2 (1993), pp. 1372–1377. DOI: doi:10.1063/1.464304..

[55] J. P. Perdew, M. Ernzerhof, and K. Burke. "Rationale for mixing exact exchange with density functional approximations". In: *J. Chem. Phys.* 105.22 (1996), pp. 9982–9985. ISSN: 00219606. DOI: DOI:10.1063/1.472933. URL: http://dx.doi.org/doi/10.1063/1.472933.

[56] M. Ernzerhof, J. P. Perdew, and K. Burke. "Coupling-constant dependence of atomization energies". In: *International Journal of Quantum Chemistry* 64.3 (1997), pp. 285–295. ISSN: 1097-461X. DOI: 10.1002/(SICI)1097-461X(1997)64:3<285::AID-QUA2>3.0.CO;2-S. URL: http://dx.doi.org/10.1002/(SICI)1097-461X(1997)64:3<285::AID-QUA2>3.0.CO;2-S.

[57] F. Fuchs et al. "Quasiparticle band structure based on a generalized Kohn-Sham scheme". In: *Phys. Rev. B* 76 (11 2007), p. 115109. DOI: 10.1103/PhysRevB.76.115109. URL: http://link.aps.org/doi/10.1103/PhysRevB.76.115109.

[58] J. Heyd and G. E. Scuseria. "Assessment and validation of a screened Coulomb hybrid density functional". In: *The Journal of Chemical Physics* 120.16 (2004), pp. 7274–7280. DOI: http://dx.doi.org/10.1063/1.1668634. URL: http:

//scitation.aip.org/content/aip/journal/jcp/120/16/10.1063/1.1668634.

[59] R. T. Sharp and G. K. Horton. "A Variational Approach to the Unipotential Many-Electron Problem". In: *Phys. Rev.* 90 (2 1953), pp. 317–317. DOI: 10.1103/PhysRev.90.317. URL: http://link.aps.org/doi/10.1103/PhysRev.90.317.

[60] J. D. Talman and W. F. Shadwick. "Optimized effective atomic central potential". In: *Phys. Rev. A* 14 (1 1976), pp. 36–40. DOI: 10.1103/PhysRevA.14.36. URL: http://link.aps.org/doi/10.1103/PhysRevA.14.36.

[61] A. D. Becke and E. R. Johnson. "A simple effective potential for exchange". In: *The Journal of Chemical Physics* 124.22, 221101 (2006), pp. –. DOI: http://dx.doi.org/10.1063/1.2213970. URL: http://scitation.aip.org/content/aip/journal/jcp/124/22/10.1063/1.2213970.

[62] V. N. Staroverov, G. E. Scuseria, and E. R. Davidson. "Optimized effective potentials yielding Hartree-Fock energies and densities". In: *The Journal of Chemical Physics* 124.14, 141103 (2006), pp. –. DOI: http://dx.doi.org/10.1063/1.2194546. URL: http://scitation.aip.org/content/aip/journal/jcp/124/14/10.1063/1.2194546.

[63] A. D. Becke and M. R. Roussel. "Exchange holes in inhomogeneous systems: A coordinate-space model". In: *Phys. Rev. A* 39 (8 1989), pp. 3761–3767. DOI: 10.1103/PhysRevA.39.3761. URL: http://link.aps.org/doi/10.1103/PhysRevA.39.3761.

[64] Y.-S. Kim et al. "Towards efficient band structure and effective mass calculations for III-V direct band-gap semiconductors". In: *Phys. Rev. B* 82 (20 2010), p. 205212. DOI: 10.1103/PhysRevB.82.205212. URL: http://link.aps.org/doi/10.1103/PhysRevB.82.205212.

[65] C. Cohen-Tannoudji, B. Diu, and F. Laloë. *Quantenmechanik*. Vol. 2. Berlin New York: Walter de Gruyter, 2008.

[66] D. D. Koelling and B. N. Harmon. "A technique for relativistic spin-polarised calculations". In: *Journal of Physics C: Solid State Physics* 10.16 (1977), p. 3107. URL: http://stacks.iop.org/0022-3719/10/i=16/a=019.

[67] G. Kresse and J. Furthmüller. "Efficient iterative schemes for *ab initio* total-energy calculations using a plane-wave basis set". In: *Phys. Rev. B* 54 (16 1996), pp. 11169–11186. DOI: 10.1103/PhysRevB.54.11169.

[68] G. Kresse and J. Furthmüller. "Efficiency of ab-initio total energy calculations for metals and semiconductors using a plane-wave basis set". In: *Comp. Mat. Sci.* 6 (1996), p. 15. DOI: 10.1016/0927-0256(96)00008-0.

[69] P. Pulay. "Convergence acceleration of iterative sequences. the case of scf iteration". In: *Chemical Physics Letters* 73.2 (1980), pp. 393 –398. ISSN: 0009-2614. DOI: DOI:10.1016/0009-2614(80)80396-4. URL: http://www.sciencedirect.com/science/article/pii/0009261480803964.

[70] D. D. Johnson. "Modified Broyden's method for accelerating convergence in self-consistent calculations". In: *Phys. Rev. B* 38 (18 1988), pp. 12807–12813. DOI: 10.1103/PhysRevB.38.12807. URL: http://link.aps.org/doi/10.1103/PhysRevB.38.12807.

[71] H. Hellmann. *Einfuehrung in die Quantenchemie*. Leipzig: Deuticke, 1937.

[72] R. P. Feynman. "Forces in Molecules". In: *Phys. Rev.* 56 (4 1939), pp. 340–343. DOI: 10.1103/PhysRev.56.340. URL: http://link.aps.org/doi/10.1103/PhysRev.56.340.

[73] F. D. Murnaghan. "The Compressibility of Media under Extreme Pressures". In: *P. Nat. Acad. Sci. USA* 30.9 (1944), pp. 244–247. URL: http://www.pnas.org/content/30/9/244.short.

[74] J. Hafner. "Ab-initio simulations of materials using VASP: Density-functional Theory and beyond". In: *Journal of Computational Chemistry* 29 (2008), p. 13.

[75] H. J. Monkhorst and J. D. Pack. "Special points for Brillouin-zone integrations". In: *Phys. Rev. B* 13 (12 1976), pp. 5188–5192. DOI: 10.1103/PhysRevB.13.5188.

[76] P. E. Blöchl. "Projector augmented-wave method". In: *Phys. Rev. B* 50.24 (Dec. 1994), pp. 17953–17979. DOI: 10.1103/PhysRevB.50.17953.

[77] F. Bechstedt. *Principles of Surface Physics*. Springer-Verlag, Berlin, 2003.

[78] B. Adolph et al. "Nonlocality and many-body effects in the optical properties of semiconductors". In: *Phys. Rev. B* 53 (15 1996), pp. 9797–9808. DOI: 10.1103/PhysRevB.53.9797. URL: http://link.aps.org/doi/10.1103/PhysRevB.53.9797.

[79] M. Gajdoš et al. "Linear optical properties in the projector-augmented wave methodology". In: *Phys. Rev. B* 73 (4 2006), p. 045112. DOI: 10.1103/PhysRevB.73.045112. URL: http://link.aps.org/doi/10.1103/PhysRevB.73.045112.

[80] L. E. Ramos, J. Furthmüller, and F. Bechstedt. "Quantum confinement in Si- and Ge-capped nanocrystallites". In: *Phys. Rev. B* 72 (4 2005), p. 045351. DOI: 10.1103/PhysRevB.72.045351. URL: http://link.aps.org/doi/10.1103/PhysRevB.72.045351.

[81] C. Delerue, G. Allan, and M. Lannoo. "Theoretical aspects of the luminescence of porous silicon". In: *Phys. Rev. B* 48 (15 1993), pp. 11024–11036. DOI: 10.1103/PhysRevB.48.11024. URL: http://link.aps.org/doi/10.1103/PhysRevB.48.11024.

[82] G. Allan, C. Delerue, and Y. M. Niquet. "Luminescence polarization of silicon nanocrystals". In: *Phys. Rev. B* 63 (20 2001), p. 205301. DOI: 10.1103/PhysRevB.63.205301. URL: http://link.aps.org/doi/10.1103/PhysRevB.63.205301.

[83] R. Leitsmann and F. Bechstedt. "Characteristic Energies and Shifts in Optical Spectra of Colloidal IV-VI Semiconductor Nanocrystals". In: *ACS Nano* 3.11 (2009). PMID: 19873980, pp. 3505–3512. DOI: 10.1021/nn900987j. eprint: http://pubs.acs.org/doi/pdf/10.1021/nn900987j. URL: http://pubs.acs.org/doi/abs/10.1021/nn900987j.

[84] K. Seino et al. "Influence of SiO2 matrix on electronic and optical properties of Si nanocrystals". In: *Nanotechnology* 20 (2009), p. 135702. DOI: 10.1088/0957-4484/20/13/135702. URL: http://iopscience.iop.org/0957-4484/20/13/135702.

[85] S. Öğüt, J. R. Chelikowsky, and S. G. Louie. "Quantum Confinement and Optical Gaps in Si Nanocrystals". In: *Phys. Rev. Lett.* 79 (9 1997), pp. 1770–1773. DOI: 10.1103/PhysRevLett.79.1770. URL: http://link.aps.org/doi/10.1103/PhysRevLett.79.1770.

[86] R. W. Godby and I. D. White. "Density-Relaxation Part of the Self-Energy". In: *Phys. Rev. Lett.* 80 (14 1998), pp. 3161–3161. DOI: 10.1103/PhysRevLett.80.3161. URL: http://link.aps.org/doi/10.1103/PhysRevLett.80.3161.

[87] H.-C. Weissker, J. Furthmüller, and F. Bechstedt. "Optical properties of Ge and Si nanocrystallites from *ab initio* calculations. II. Hydrogenated nanocrystallites". In: *Phys. Rev. B* 65 (15 2002), p. 155328. DOI: 10.1103/PhysRevB.65.155328. URL: http://link.aps.org/doi/10.1103/PhysRevB.65.155328.

[88] E. Lifshitz et al. "Air-Stable PbSe/PbS and PbSe/PbSe$_x$S$_{1-x}$ Core-Shell Nanocrystal Quantum Dots and their Applications". In: *The Journal of Physical Chemistry B* 110.50 (2006). PMID: 17165982, pp. 25356–25365. DOI: 10.1021/jp0644356. eprint: http://dx.doi.org/10.1021/jp0644356. URL: http://dx.doi.org/10.1021/jp0644356.

[89] A. Franceschetti. "Structural and electronic properties of PbSe nanocrystals from first principles". In: *Phys. Rev. B* 78 (7 2008), p. 075418. DOI: 10.1103/PhysRevB.78.075418. URL: http://link.aps.org/doi/10.1103/PhysRevB.78.075418.

[90] R. Farrow et al. "The growth of metastable, heteroepitaxial films of α-Sn by metal beam epitaxy". In: *Journal of Crystal Growth* 54.3 (1981), p. 507. ISSN: 0022-0248. DOI: 10.1016/0022-0248(81)90506-6. URL: http://www.sciencedirect.com/science/article/pii/0022024881905066.

[91] A. Thewlis J. Davey. "Thermal Expansion of Grey Tin". In: *Nature* 174 (1954), p. 1011. DOI: 10.1038/1741011a0. URL: http://dx.doi.org/10.1038/1741011a0.

[92] A. R. West. *Basic Solid State Chemistry*. Wiley, 1988.

[93] M. E. Straumanis and C. D. Kim. "Lattice Parameters, Thermal Expansion Coefficients, Phase Width, and Perfection of the Structure of GaSb and InSb". In: *Journal of Applied Physics* 36.12 (1965), pp. 3822–3825. DOI: http://dx.doi.org/10.1063/1.1713955. URL: http://scitation.aip.org/content/aip/journal/jap/36/12/10.1063/1.1713955.

[94] W. Martienssen and H. Warlimont. *Springer handbook of condensed matter and materials data*. Bd. 1. Springer, 2005. URL: http://books.google.de/books?id=TnHJX79b3RwC.

[95] P. Yu and M. Cardona. *Fundamentals of Semiconductors*. Springer, Berlin, 1996.

[96] L. E. Ramos, J. Furthmüller, and F. Bechstedt. "Quantum confinement in Si- and Ge-capped nanocrystallites". In: *Phys. Rev. B* 72 (4 2005), p. 045351. DOI: 10.1103/PhysRevB.72.045351. URL: http://link.aps.org/doi/10.1103/PhysRevB.72.045351.

[97] J.-W. Luo et al. "Comparative study for colloidal quantum dot conduction band state calculations". In: *Applied Physics Letters* 88.14, 143108 (2006), pp. –. DOI: http://dx.doi.org/10.1063/1.219257. URL: http://

scitation.aip.org/content/aip/journal/apl/88/14/10.1063/1.2192575.

[98] Sargent-Welch. *Table of Periodic Properties of the Elements*. Sargent-Welch Scientific Co., Skokie (IL), 1980.

[99] J. N. Schulman and Y.-C. Chang. "HgTe-CdTe superlattice subband dispersion". In: *Phys. Rev. B* 33 (4 1986), pp. 2594–2601. DOI: 10.1103/PhysRevB.33.2594. URL: http://link.aps.org/doi/10.1103/PhysRevB.33.2594.

[100] O. Madelung. *Semiconductors: group IV elements and III-V compounds*. Springer-Verlag, 1991. URL: http://books.google.de/books?id=kRxRAAAAMAAJ.

[101] J. Mavroides and D. Kolesar. "Elastic constants of HgTe". In: *Solid State Communications* 2.12 (1964), pp. 363 –364. ISSN: 0038-1098. DOI: http://dx.doi.org/10.1016/0038-1098(64)90182-6. URL: http://www.sciencedirect.com/science/article/pii/0038109864901826.

[102] J. Reno and L. Stephenson. "The stability of α-Sn grown on CdTe by molecular beam epitaxy". In: *J. Electronic Materials* 19.6 (1990), pp. 549–553. ISSN: 0361-5235. URL: http://dx.doi.org/10.1007/BF02651277.

[103] J. A. Gómez et al. "Theoretical and experimental study of α-Sn deposited on CdTe(001)". In: *Phys. Rev. B* 67 (11 2003), p. 115340. DOI: 10.1103/PhysRevB.67.115340. URL: http://link.aps.org/doi/10.1103/PhysRevB.67.115340.

[104] P. Löwdin. "On the Non-Orthogonality Problem Connected with the Use of Atomic Wave Functions in the Theory of Molecules and Crystals". In: *The Journal of Chemical Physics* 18.3 (1950), pp. 365–375. DOI: http://dx.doi.org/10.1063/1.1747632. URL: http://scitation.aip.org/content/aip/journal/jcp/18/3/10.1063/1.1747632.

[105] P. Vogl, H. P. Hjalmarson, and J. D. Dow. "A Semi-empirical tight-binding theory of the electronic structure of semiconductors". In: *Journal of Physics and Chemistry of Solids* 44.5 (1983), pp. 365 –378. DOI: 10.1016/0022-3697(83)90064-10. URL: http://www.sciencedirect.com/science/article/pii/0022369783900641.

[106] J. C. Slater and G. F. Koster. "Simplified LCAO Method for the Periodic Potential Problem". In: *Phys. Rev.* 94 (6 1954), pp. 1498–1524. DOI: 10.1103/PhysRev.94.1498. URL: http://link.aps.org/doi/10.1103/PhysRev.94.1498.

[107] Y. Li and P. J. Lin-Chung. "New semiempirical construction of the Slater-Koster parameters for group-IV semiconductors". In: *Phys. Rev. B* 27 (6 1983), pp. 3465–3470. DOI: 10.1103/PhysRevB.27.3465. URL: http://link.aps.org/doi/10.1103/PhysRevB.27.3465.

[108] T. B. Boykin. "More complete treatment of spin-orbit effects in tight-binding models". In: *Phys. Rev. B* 57 (3 1998), pp. 1620–1625. DOI: 10.1103/PhysRevB.57.1620. URL: http://link.aps.org/doi/10.1103/PhysRevB.57.1620.

[109] Y. A. Bychkov and E. I. Rashba. "Oscillatory effects and the magnetic susceptibility of carriers in inversion layers". In: *Journal of Physics C: Solid State Physics* 17.33 (1984), p. 6039. URL: http://stacks.iop.org/0022-3719/17/i=33/a=015.

[110] G. Dresselhaus. "Spin-Orbit Coupling Effects in Zinc Blende Structures". In: *Phys. Rev.* 100 (2 1955), pp. 580–586. DOI: 10.1103/PhysRev.100.580. URL: http://link.aps.org/doi/10.1103/PhysRev.100.580.

[111] W. Harrison. *Electronic Structure and the Properties of Solids*. Dover, New York, 1989.

[112] J. Vidal et al. "Large insulating gap in topological insulators induced by negative spin-orbit splitting". In: *Phys. Rev. B* 86 (7 2012), p. 075316. DOI: 10.1103/PhysRevB.86.075316. URL: http://link.aps.org/doi/10.1103/PhysRevB.86.075316.

[113] H. Landolt and R. Börnstein. *Zahlenwerte und Funktionen aus Physik, Chemie, Astronomie, Geophysik und Technik*. Vol. 6. Berlin: Springer-Verlag, 1982.

[114] S. Groves and W. Paul. "Band Structure of Gray Tin". In: *Phys. Rev. Lett.* 11 (5 1963), pp. 194–196. DOI: 10.1103/PhysRevLett.11.194. URL: http://link.aps.org/doi/10.1103/PhysRevLett.11.194.

[115] N. Orlowski et al. "Direct evidence for the inverted band structure of HgTe". In: *Phys. Rev. B* 61 (8 2000), R5058–R5061. DOI: 10.1103/PhysRevB.61.R5058. URL: http://link.aps.org/doi/10.1103/PhysRevB.61.R5058.

[116] G. L. Hansen, J. L. Schmit, and T. N. Casselman. "Energy gap versus alloy composition and temperature in Hg1âĹŠxCdxTe". In: *Journal of Applied Physics* 53.10 (1982), pp. 7099–7101. DOI: http://dx.doi.org/10.1063/1.330018. URL: http://scitation.aip.org/content/aip/journal/jap/53/10/10.1063/1.330018.

[117] M. Cardona, K. L. Shaklee, and F. H. Pollak. "Electroreflectance at a Semiconductor-Electrolyte Interface". In: *Phys. Rev.* 154 (3 1967), pp. 696–720. DOI: 10.1103/PhysRev.154.696. URL: http://link.aps.org/doi/10.1103/PhysRev.154.696.

[118] R. Poerschke and O. Madelung. *Data in Science and Technology, Semiconductors Group IV Elements and III-V Compounds*. Berlin: Springer-Verlag, 1991.

[119] R. Sakuma et al. "GW calculations including spin-orbit coupling: Application to Hg chalcogenides". In: *Phys. Rev. B* 84 (8 2011), p. 085144. DOI: 10.1103/PhysRevB.84.085144. URL: http://link.aps.org/doi/10.1103/PhysRevB.84.085144.

[120] A. Svane et al. "Quasiparticle band structures of β-HgS, HgSe, and HgTe". In: *Phys. Rev. B* 84 (20 2011), p. 205205. DOI: 10.1103/PhysRevB.84.205205. URL: http://link.aps.org/doi/10.1103/PhysRevB.84.205205.

[121] S. Groves et al. "Interband magnetoreflection of α-Sn". In: *Journal of Physics and Chemistry of Solids* 31.9 (1970), pp. 2031 –2049. ISSN: 0022-3697. DOI: http://dx.doi.org/10.1016/0022-3697(70)90006-5. URL: http://www.sciencedirect.com/science/article/pii/0022369770900065.

[122] A. Fleszar and W. Hanke. "Electronic structure of II^B-VI semiconductors in the GW approximation". In: *Phys. Rev. B* 71 (4 2005), p. 045207. DOI: 10.1103/PhysRevB.71.045207. URL: http://link.aps.org/doi/10.1103/PhysRevB.71.045207.

[123] K. Hummer. In: *unpublished* ().

[124] D. Eich et al. "Band Discontinuity and Band Gap of MBE Grown HgTe/CdTe(001) Heterointerfaces Studied by k-Resolved Photoemission and Inverse Photoemission". In: *physica status solidi (a)* 173.1 (1999), pp. 261–267. ISSN: 1521-396X. DOI: 10.1002/(SICI)1521-396X(199905)173:1<261::AID-PSSA261>3.0.CO;2-#. URL: http://dx.doi.org/10.1002/(SICI)1521-396X(199905)173:1<261::AID-PSSA261>3.0.CO;2-#.

[125] J. Camassel et al. "Temperature dependance of the fundamental absorption edge in CdTe". In: *Solid State Communications* 13.1 (1973), pp. 63 – 68. ISSN: 0038-1098. DOI: http://dx.doi.org/10.1016/0038-1098(73)90068-9. URL: http://www.sciencedirect.com/science/article/pii/0038109873900689.

[126] C. L. Littler and D. G. Seiler. "Temperature dependence of the energy gap of InSb using nonlinear optical techniques". In: *Applied Physics Letters* 46.10 (1985), pp. 986–988. DOI: http://dx.doi.org/10.1063/1.95789. URL: http://scitation.aip.org/content/aip/journal/apl/46/10/10.1063/1.95789.

[127] M. W. Goodwin, D. G. Seiler, and M. H. Weiler. "Two-photon magnetoabsorption spectroscopy in n-InSb with cw CO_2 lasers". In: *Phys. Rev. B* 25 (10 1982), pp. 6300–6309. DOI: 10.1103/PhysRevB.25.6300. URL: http://link.aps.org/doi/10.1103/PhysRevB.25.6300.

[128] S. Logothetidis, L. Via, and M. Cardona. "Temperature dependence of the dielectric function and the interband critical points of InSb". In: *Phys. Rev. B* 31 (2 1985), pp. 947–957. DOI: 10.1103/PhysRevB.31.947. URL: http://link.aps.org/doi/10.1103/PhysRevB.31.947.

[129] L. Müchler et al. "Topological Insulators from a Chemist's Perspective". In: *Angew. Chem. Int. Ed.* 51 (2012), p. 7221. DOI: 10.1002/anie.201202480.

[130] R. Enderlein and N. J. M. Horing. *Fundamentals of Semiconductor Physics and Devices*. World Scientific Publishing, 1997.

[131] L. Vina, H. Höchst, and M. Cardona. "Dielectric function of α -Sn and its temperature dependence". In: *Phys. Rev. B* 31 (2 1985), pp. 958–967. DOI: 10.1103/PhysRevB.31.958. URL: http://link.aps.org/doi/10.1103/PhysRevB.31.958.

[132] W. G. Schmidt et al. "Efficient $\mathcal{O}(N^2)$ method to solve the Bethe-Salpeter equation". In: *Phys. Rev. B* 67 (8 2003), p. 085307. DOI: 10.1103/PhysRevB.67.085307. URL: http://link.aps.org/doi/10.1103/PhysRevB.67.085307.

[133] A. Riefer et al. "Interplay of excitonic effects and van Hove singularities in optical spectra: CaO and AlN polymorphs". In: *Phys. Rev. B* 84 (7 2011), p. 075218. DOI: 10.1103/PhysRevB.84.075218. URL: http://link.aps.org/doi/10.1103/PhysRevB.84.075218.

[134] A. Schleife et al. "Optical and energy-loss spectra of MgO, ZnO, and CdO from ab initio many-body calculations". In: *Phys. Rev. B* 80.3 (2009), p. 035112. DOI: 10.1103/PhysRevB.80.035112.

[135] L. G. Ferreira, M. Marques, and L. K. Teles. "Approximation to density functional theory for the calculation of band gaps of semiconductors". In: *Phys. Rev. B* 78 (12 2008), p. 125116. DOI: 10.1103/PhysRevB.78.125116. URL: http://link.aps.org/doi/10.1103/PhysRevB.78.125116.

[136] F. Bechstedt and A. Belabbes. "Structure, energetics, and electronic states of III-V compound polytypes". In: *Journal of Physics: Condensed Matter* 25.27 (2013), p. 273201. URL: http://stacks.iop.org/0953-8984/25/i=27/a=273201.

[137] L. Fu and C. L. Kane. "Time reversal polarization and a Z_2 adiabatic spin pump". In: *Phys. Rev. B* 74 (19 2006), p. 195312. DOI: 10.1103/PhysRevB.74.195312. URL: http://link.aps.org/doi/10.1103/PhysRevB.74.195312.

[138] Y. Ando. "Topological Insulator Materials". In: *Journal of the Physical Society of Japan* 82.10 (2013), p. 102001. DOI: 10.1143/JPSJ.82.102001. URL: http://jpsj.ipap.jp/link?JPSJ/82/102001/.

[139] R. Yu et al. "Equivalent expression of $\mathbb{Z}_2$ topological invariant for band insulators using the non-Abelian Berry connection". In: *Phys. Rev. B* 84 (7 2011), p. 075119. DOI: 10.1103/PhysRevB.84.075119. URL: http://link.aps.org/doi/10.1103/PhysRevB.84.075119.

[140] A. A. Soluyanov and D. Vanderbilt. "Computing topological invariants without inversion symmetry". In: *Phys. Rev. B* 83 (23 2011), p. 235401. DOI: 10.1103/PhysRevB.83.235401. URL: http://link.aps.org/doi/10.1103/PhysRevB.83.235401.

[141] E. Prodan. "Manifestly gauge-independent formulations of the $\mathbb{Z}_2$ invariants". In: *Phys. Rev. B* 83 (23 2011), p. 235115. DOI: 10.1103/PhysRevB.83.235115. URL: http://link.aps.org/doi/10.1103/PhysRevB.83.235115.

[142] L. Winterfeld et al. "Strain-induced topological insulator phase transition in HgSe". In: *Phys. Rev. B* 87 (7 2013), p. 075143. DOI: 10.1103/PhysRevB.87.075143. URL: http://link.aps.org/doi/10.1103/PhysRevB.87.075143.

[143] L. E. Ramos et al. "Optical properties of Si and Ge nanocrystals: Parameter-free calculations". In: *physica status solidi (b)* 242.15 (2005), pp. 3053–3063. DOI: 10.1002/pssb.200562229. URL: http://dx.doi.org/10.1002/pssb.200562229.

[144] L. Landau and E. Lifshitz. *Statistical Physics*. Vol. 5. Pergamon, Oxford, 1959.

[145] A. Baldan. "Review Progress in Ostwald ripening theories and their applications to nickel-base superalloys Part I: Ostwald ripening theories". English. In: *Journal of Materials Science* 37.11 (2002), pp. 2171–2202. ISSN: 0022-2461. DOI: 10.1023/A:1015388912729. URL: http://dx.doi.org/10.1023/A%3A1015388912729.

[146] J.-W. Luo et al. "Comparative study for colloidal quantum dot conduction band state calculations". In: *Applied Physics Letters* 88.14, 143108 (2006), p. 143108. DOI: 10.1063/1.2192575. URL: http://link.aip.org/link/?APL/88/143108/1.

[147] F. Trani et al. "Tight-binding calculation of the optical absorption cross section of spherical and ellipsoidal silicon nanocrystals". In: *Phys. Rev. B* 72 (7 2005), p. 075423. DOI: 10.1103/PhysRevB.72.075423. URL: http://link.aps.org/doi/10.1103/PhysRevB.72.075423.

[148] H. Fu, L.-W. Wang, and A. Zunger. "Applicability of the $\mathbf{k} \cdot \mathbf{p}$ method to the electronic structure of quantum dots". In: *Phys. Rev. B* 57 (16 1998), pp. 9971–9987. DOI: 10.1103/PhysRevB.57.9971. URL: http://link.aps.org/doi/10.1103/PhysRevB.57.9971.

[149] L. E. Ramos, J. Furthmüller, and F. Bechstedt. "Effect of backbond oxidation on silicon nanocrystallites". In: *Phys. Rev. B* 70 (3 2004), p. 033311. DOI: 10.1103/PhysRevB.70.033311. URL: http://link.aps.org/doi/10.1103/PhysRevB.70.033311.

[150] F. Bechstedt, F. Fuchs, and G. Kresse. "Ab-initio theory of semiconductor band structures: New developments and progress". In: *Phys. Status Solidi B* 246.8 (2009), pp. 1877–1892. DOI: 10.1002/pssb.200945074.

[151] C. Delerue, M. Lannoo, and G. Allan. "Excitonic and Quasiparticle Gaps in Si Nanocrystals". In: *Phys. Rev. Lett.* 84 (11 2000), pp. 2457–2460. DOI: 10.1103/PhysRevLett.84.2457. URL: http://link.aps.org/doi/10.1103/PhysRevLett.84.2457.

[152] L. B. Ma et al. "Evolution of photoluminescence properties of $Si_{1-x}Ge_x$ nanocrystals synthesized by laser-induced pyrolysis". In: *Applied Physics Letters* 95.1, 013115 (2009), p. 013115. DOI: 10.1063/1.3176948. URL: http://link.aip.org/link/?APL/95/013115/1.

[153] H.-C. Weissker, J. Furthmüller, and F. Bechstedt. "Structural relaxation in Si and Ge nanocrystallites: Influence on the electronic and optical properties". In: *Phys. Rev. B* 67 (24 2003), p. 245304. DOI: 10.1103/PhysRevB.67.245304. URL: http://link.aps.org/doi/10.1103/PhysRevB.67.245304.

[154] H.-C. Weissker et al. "Luminescence and absorption in germanium and silicon nanocrystals: The influence of compression, surface reconstruction, optical excitation, and spin-orbit splitting". In: *Phys. Rev. B* 83 (12 2011), p. 125413. DOI: 10.1103/PhysRevB.83.125413. URL: http://link.aps.org/doi/10.1103/PhysRevB.83.125413.

[155] H.-C. Weissker, J. Furthmüller, and F. Bechstedt. "Excitation Energies and Radiative Lifetimes of $Ge_{1-x}Si_x$ Nanocrystals: Alloying Versus Confinement Effects". In: *Phys. Rev. Lett.* 90 (8 2003), p. 085501. DOI: 10.1103/PhysRevLett.90.085501. URL: http://link.aps.org/doi/10.1103/PhysRevLett.90.085501.

[156] O. Guillois et al. "Photoluminescence decay dynamics of noninteracting silicon nanocrystals". In: *Journal of Applied Physics* 95.7 (2004), pp. 3677–3682. DOI: 10.1063/1.1652245. URL: http://link.aip.org/link/?JAP/95/3677/1.

[157] H. Lüth. *Solid Surfaces, Interfaces and Thin Films*. Springer, Berlin, 2001.

[158] J. Tersoff. "Theory of semiconductor heterojunctions: The role of quantum dipoles". In: *Phys. Rev. B* 30 (8 1984), pp. 4874–4877. DOI: 10.1103/PhysRevB.30.4874. URL: http://link.aps.org/doi/10.1103/PhysRevB.30.4874.

[159] A. Schleife et al. "Branch-point energies and band discontinuities of III-nitrides and III-/II-oxides from quasiparticle band-structure calculations". In: *Applied Physics Letters* 94.1, 012104 (2009), pp. –. DOI: http://dx.doi.org/10.1063/1.3059569. URL: http://scitation.aip.org/content/aip/journal/apl/94/1/10.1063/1.3059569.

[160] B. Höffling et al. "Band discontinuities at Si-TCO interfaces from quasiparticle calculations: Comparison of two alignment approaches". In: *Phys. Rev. B* 85 (2012), p. 035305. DOI: 10.1103/PhysRevB.85.035305.

[161] A. Muoz, J. Sánchez-Dehesa, and F. Flores. "Reply to "Comment on 'Heterojunction valence-band-discontinuity dependence on face orientation' """. In: *Phys. Rev. B* 37 (9 1988), pp. 4803–4804. DOI: 10.1103/PhysRevB.37.4803. URL: http://link.aps.org/doi/10.1103/PhysRevB.37.4803.

[162] C. G. Van de Walle and R. M. Martin. "Comment on "Heterojunction valence-band-discontinuity dependence on face orientation"". In: *Phys. Rev. B* 37 (9 1988), pp. 4801–4802. DOI: 10.1103/PhysRevB.37.4801. URL: http://link.aps.org/doi/10.1103/PhysRevB.37.4801.

[163] H. Ibach and H. Lüth. *Festkörperphysik: Einführung in die Grundlagen*. Springer, Berlin, 1995.

[164] B. Höffling et al. "Band lineup between silicon and transparent conducting oxides". In: *Appl. Phys. Lett.* 97.3, 032116 (2010), p. 032116. DOI: 10.1063/1.3464562.

[165] Y.-C. Chang et al. "Effects of quasi-interface states in HgTe-CdTe superlattices". In: *Phys. Rev. B* 31 (4 1985), pp. 2557–2560. DOI: 10.1103/PhysRevB.31.2557. URL: http://link.aps.org/doi/10.1103/PhysRevB.31.2557.

[166] J. Anversa et al. "First-principles study of HgTe/CdTe heterostructures under perturbations preserving time-reversal symmetry". In: *Phys. Rev. B* 90 (19 2014), p. 195311. DOI: 10.1103/PhysRevB.90.195311. URL: http://link.aps.org/doi/10.1103/PhysRevB.90.195311.

[167] X. Dai et al. "Helical edge and surface states in HgTe quantum wells and bulk insulators". In: *Phys. Rev. B* 77 (12 2008), p. 125319. DOI: 10.1103/PhysRevB.77.125319. URL: http://link.aps.org/doi/10.1103/PhysRevB.77.125319.

[168] W. Harrison. *Elementary electronic structure*. Singapore: World Scientific, 1999.

Danksagung

An dieser Stelle möchte ich bei allen Personen bedanken, die mich im Rahmen dieser Arbeit unterstützt haben.
Besonderen Dank möchte ich Prof. Dr. Friedhelm Bechstedt für die Betreuung meiner Arbeit aussprechen. Er zeigte stets reges Interesse am Fortschreiten der Arbeit, stand mir jederzeit helfend und beratend zur Seite und regte darüber hinaus fortwährend zum selbstständigen Weiterdenken an. Auch sorgte er dafür, dass meine finanzielle Situation während der gesamten Arbeit gesichert war. Seine Unterstützung trug maßgeblich zur Fertigstellung dieser Arbeit bei.
Meinen Kollegen Lars Matthes, Andreas Schrön, und Benjamin Höffling danke ich für die angenehme Arbeitsatmosphäre und viele Diskussionen zu technischen und physikalischen Aspekten. Lars Matthes danke ich darüber hinaus für die wertvolle Zusammenarbeit bei der Bearbeitung physikalischer Fragestellungen. Martin Fitzner, dessen Diplomarbeit ich betreut habe, danke ich für seine Arbeit, die auch zum besseren Verständnis der in dieser Arbeit diskutierten Probleme beigetragen hat.
Meinem besten Freund Philipp Wagner gilt mein Dank für die vielen Diskussionen und Gespräche und seine Hilfsbereitschaft.
Vor allem möchte ich mich bei meinen Eltern für ihre unermüdliche Unterstützung, nicht nur im Rahmen dieser Arbeit, bedanken. Ohne Eure Hilfe und Euer Vertrauen in mich wäre all das nicht möglich gewesen.

THESEN

1. Die korrekte Beschreibung der Elektronenstruktur der Volumenkristalle von α-Zinn und HgTe bezüglich der Bandordnung der Γ_{8v}-, Γ_{7v}-, und Γ_{6c} Zustände sowie der Null-Gap-Halbleitercharakteristik, aber auch von Nanostrukturen, im Rahmen der Dichtefunktionaltheorie (DFT) erfordert die explizite oder näherungsweise Berücksichtigung von Quasiteilcheneffekten und Spin-Bahn-Wechselwirkung.

2. Die Modellierung von Austausch und Korrelation (XC) im Rahmen des HSE06 Hybridfunktionals, sowie die Anwendung des approximativen MBJLDA XC Funktionals, führen zu einer hinreichend genauen Beschreibung der kritischen Bandstrukturparameter und Bandordnung von kristallinem α-Sn und HgTe.

3. Um nanokristalline Systeme zu modellieren, die aufgrund ihrer Größe und des resultierenden Rechenaufwandes nicht im Rahmen von DFT behandelt werden können, eignet sich die empirische Methode der starken Bindung mit Spin-Bahn Wechselwirkung.

4. Die Berechnung der topologischen $\mathbb{Z}_2$-Invarianten von Volumenkristallen kann unabhängig von einer Eichtransformation unter Verwendung von *ab-initio* berechneten Wellenfunktionen durch die Berechung der Evolution der Wannier-Ladungszentren, die als Phasen der Eigenwerte des auf den besetzten Unterraum der Blochwellenfunktionen projizierten Ortsoperators bestimmt werden können, parallel zu den reziproken Gittervektoren erfolgen.

5. HgTe und α-Sn sind starke topologische Isolatoren, während CdTe und InSb triviale Isolatoren sind.

6. α-Sn-Nanokristalle mit einem Durchmesser unterhalb von 12 nm besitzen eine invertierte Bandordnung verglichen mit dem Volumenkristall. Bei einem kritischen Durchmesser von ca. 12 nm tritt ein topologischer Übergang auf, an welchem sich die Bandordnung der Γ_{8v} und Γ_{6c} Zustände umkehrt. Ihre optische Absorptions- und Emissionswellenlänge kann über die Größe der NCs beeinflusst werden.

7. An der α-Sn(001) Oberfläche bilden sich topologische Oberflächenzustände unterhalb der Fermienergie aus. Diese weisen eine lineare $\mathbf{k}$-Dispersion in Form von Dirac-Kegeln auf und sind spinpolarisiert.

8. HgTe/CdTe(001), HgTe/CdTe(110) und α-Sn/CdTe(001) Multiquantumwellstrukturen zeigen bei einer kritischen Dicke von 4.6 nm einen topologischen Phasenübergang von einem trivialen Isolator in die Quanten-Spin Hall (QSH) Phase, die sich durch das Auftreten von metallischen, linearen und spinpolarisierten Kantenzuständen, die an der Grenzschicht zwischen beiden Materialien lokalisiert sind, auszeichnet.

9. In α-Sn/CdTe(110) und HgTe/InSb(110)-Multiquantumwellstrukturen führt die unterschiedliche Ionizität der Bindungen in den Quantengraben- und Barrierematerialien zur Ausbildung eines intrinsischen Dipols in der Grenzschicht, wodurch die Entstehung einer topologisch nichttrivialen QSH Phase verhindert wird.

Ehrenwörtliche Erklärung

Ich erkläre hiermit ehrenwörtlich, dass ich die vorliegende Arbeit selbständig, ohne unzulässige Hilfe Dritter und ohne Benutzung anderer als der angegebenen Hilfsmittel und Literatur angefertigt habe. Die aus anderen Quellen direkt oder indirekt übernommenen Daten und Konzepte sind unter Angabe der Quelle gekennzeichnet. Bei der Auswahl und Auswertung folgenden Materials haben mir die nachstehend aufgeführten Personen in der jeweils beschriebenen Weise unentgeltlich geholfen:

1. Dipl.-Phys Lars Matthes, durch die gemeinsame Bearbeitung der in Kapitel 3.2 dargestellten Fragestellungen,

2. M.Sc. Martin Fitzner, dessen Masterarbeit im Rahmen der vorliegenden Dissertation betreut wurde, durch die gemeinsame Bearbeitung der in den Abschnitten 2.6 und 3.4.2 diskutierten Fragestellungen,

3. Prof. Dr. sc. nat. Friedhelm Bechstedt als betreuender Hochschullehrer.

Weitere Personen waren an der inhaltlich-materiellen Erstellung der vorliegenden Arbeit nicht beteiligt. Insbesondere habe ich hierfür nicht die entgeltliche Hilfe von Vermittlungs- bzw. Beratungsdiensten (Promotionsberater oder andere Personen) in Anspruch genommen. Niemand hat von mir unmittelbar oder mittelbar geldwerte Leistungen für Arbeiten erhalten, die im Zusammenhang mit dem Inhalt der vorgelegten Dissertation stehen. Die Arbeit wurde bisher weder im In- noch im Ausland in gleicher oder ähnlicher Form einer anderen Prüfungsbehörde vorgelegt. Die geltende Promotionsordnung der Physikalisch-Astrono mischen Fakultät ist mir bekannt. Ich versichere ehrenwörtlich, dass ich nach bestem Wissen die reine Wahrheit gesagt und nichts verschwiegen habe.

Jena, den 10. März 2015

Lebenslauf

Zur Person

Name	Sebastian Küfner
Geburtsdatum	13.05.1987
Geburtsort	Gera

Ausbildung

Juli 1998 - Mai 2005	Georg-Christoph-Lichtenberg Gymnasium Gera
2005	Abitur am Georg-Christoph-Lichtenberg Gymnasium Gera
Januar 2006 - September 2006	Zivildienst im SRH Waldklinikum Gera
September 2006 - Oktober 2011	Studium der Physik an der Friedrich-Schiller-Universität Jena
Oktober 2011	Hochschulabschluss als Diplom-Physiker an der Friedrich-Schiller-Universität Jena
Seit November 2011	Wissenschaftlicher Mitarbeiter am Institut für Festkörpertheorie und -optik der FSU Jena

Jena, den 10. März 2015